DEVELOPMENT OF PHOTOANODES FOR PERFORMANCE ENHANCED DYE SENSITIZED SOLAR CELLS

A THESIS SUBMITTED TO

THE GRADUATE SCHOOL OF ENGINEERING AND SCIENCE

OF BILKENT UNIVERSITY

IN PARTIAL FULFILLMENT OF THE REQUIREMENTS

FOR THE DEGREE OF

MASTER OF SCIENCE

IN

MATERIALS SCIENCE AND NANOTECHNOLOGY

By

Türkan Gamze Ulusoy

August, 2015

DEVELOPMENT OF PHOTOANODES FOR PERFORMANCE ENHANCED DYE SENSITIZED SOLAR CELLS

By Turkan Gamze Ulusoy

August, 2015

We certify that we have read this thesis and that in our opinion it is fully adequate, in scope and in quality, as a thesis for the degree of Master of Science.

_____

Assist. Prof. Dr. Ali Kemal Okyay (Advisor)

_____

Prof. Dr. Ahmet Macit Özenbaş

_____

Assist. Prof. Dr. Ferdi Karadaş

Approved for the Graduate School of Engineering and Science:

_____

Prof. Dr. Levent Onural

Director of the Graduate School

ABSTRACT

DEVELOPMENT OF PHOTOANODES FOR PERFORMANCE ENHANCED DYE SENSITIZED SOLAR CELLS

Türkan Gamze Ulusoy

M.S in Materials Science and Nanotechnology

Advisor: Assist. Prof. Dr. Ali Kemal Okyay

August, 2015

With a raising demand for clean and renewable energy sources in recent decades, **dye sensitized solar cell (DSSC),** as an efficient and low-cost solar cell technology, have attracted considerable attention and several efforts have been directed for the optimization of all components of DSSCs including photoanode, sensitizer dye, hole transport layer and counter electrode. The objective of this thesis is to provide a better understanding on the function of photoanode in overall performance of DSSC device by highlighting problems and limitations and offering proper solutions to tackle these deficiencies. Based on this understanding, this thesis reports, fabrication, characterization and analysis of designed three different cells to boost device photovoltaic performance which includes: 1) angstrom thick ZnO-sheathed TiO_2 nanowires as photoanodes, 2) multifunctional omnidirectional antireflective coating, 3) peptide nanofiber network templated ALD-grown TiO_2 nanostructures as photoanodes in DSSC.

Since photoanode-dye interface engineering is of utmost importance, the first of our proposals in this thesis relies on a systematic approach to understand the impact of atomic layer deposited (ALD) angstrom-thick ZnO sheath on hydrothermally grown TiO_2 nanowires (NWs) core utilized as photoanodes in DSSC. The results show that this ultrathin layer will contribute at device

efficiency enhancement almost three times via reducing recombination rate of injected electrons, enhancement in collection efficiency of electrons via reducing density of surface trap states without hampering injection efficiency and increased dye uptake on TiO_2 nanowires' surface which in turn leads to increased light absorption.

On the other work, we also utilized multifunctional organically modified silica (ORMOSIL) as antireflection coating layer on DSSC to improve conversion efficiency of the device via reduction in the light reflection. ORMOSIL coated DSSC surfaces show a low-reflective omnidirectional response in a wide range of wavelengths (400-800 nm). At normal incidence (θ=0°), the short circuit current density (J_{SC}) is improved to an amount of 23% as a result of ORMOSIL coating. In addition, J_{SC} meets even higher amounts of enhancement where 84% increase is recorded at θ=30°. Moreover, this coating exhibits superhydrophobicity representing a contact angle of 155º.

Finally, we proposed and implemented, self-assembled peptide amphiphiles nanofiber 3D networks in order to obtain TiO_2 nanotube structures as a template in DSSC. These self-assembled peptide amphiphiles are resistant to high temperature and more durable than other kinds of peptide amphiphiles. The advantage of this 3D fiber composed template is its high surface area and interconnected solid support providing an effective template for formation of TiO_2 network using ALD. On the other hand, since ALD offers uniform and conformal coating of high aspect ratio features, it ensures an ideal thin film coating method on high surface area nano-template materials such as the peptide nanofiber templates proposed in this study.

***Keywords*:** Photovoltaics, dye sensitized solar cells (DSSCs), interface engineering, atomic layer deposition (ALD), metal-oxides, zinc oxide, titanium dioxide, antireflection coating, peptide template, nanofiber.

ÖZET

YÜKSEK VERİMLİ BOYA UYARIMLI GÜNEŞ PİLLERİ İÇİN FOTOANOT GELİŞTİRİLMESİ

Türkan Gamze Ulusoy

Malzeme Bilimi ve Nanoteknoloji, Yüksek Lisans

Tez Danışmanı: Yrd. Doç. Dr. Ali Kemal Okyay

Ağustos, 2015

Yenilenebilir ve temiz enerji kaynaklarına son yıllarda verilen önem, **boya uyarımlı güneş pillerine (DSSCs)** yoğun ilgiyi beraberinde getirmiş ve bu aygıtların yapısında bulunan fotoanot, aktifleştirici boya, boşluk (hole) aktarım katmanı ve karşıt elektrot gibi bileşenlerin yüksek performans için optimize edilmesine sebep olmuştur. Bu çalışmada, fotoanot bileşeninin DSSC performansına nasıl etki ettiği, aygıt çalışmasında ortaya çıkan sorunlar ve kısıtlamalar ele alınarak incelenmiş ve bu sorunlar için geliştirilen çareler sunulmuştur. Yapılan çalışmalar sonucunda ise DSSClerin fotovoltaik performansını arttırmak için üç farklı yöntem kullanılmıştır. Bu tezde fotoanot olarak 1) angstrom kalınlığında ZnO-kaplı TiO_2 nanoteller, 2) çok-işlevli, her açıdan geri yansıtmasız kaplamalar ve 3) peptit nanofiber alttaşı kullanılarak ALD ile büyütülen TiO_2 nanotüpler olmak üzere DSSC sistemleri için geliştirilen performans-arttırıcı fotoanot yapıların sentezi, karakterizasyonu ve analizi detaylandırılmıştır.

Fotoanot ve boya katmanları arasında bulunan arayüzeyin optimizasyonu, fotoanot performansı için hayati önem taşımaktadır, dolayısıyla bu tezdeki ilk sunulan çalışmada hidrotermal yöntemi ile büyütülmüş TiO_2 nanotellerin üzerine angstrom kalınlığında ZnO tabakası atomik katman kaplama (ALD) tekniği ile kaplanmış ve fotoanot olarak DSSClerde kullanılmasının etkisi incelenmiştir. Angstrom kalınlığındaki ZnO katmanı, TiO_2 nanoteller için bir

arayüzey görevi görmektedir. Elde edilen sonuçlar, bu süper-ince katmanın cihazın verimini, (a) sistemdeki elektronların boşluklarla yeniden birleşmesini engelleyerek, (b) elektron enjeksiyonuna engel olmadan nanotellerin yüzeydeki kusur yoğunluğunu azaltıp elektronları toplama verimini arttırarak ve (c) TiO_2 nanotellerin yüzeylerinde boyanın emilimini güçlendirerek absorplanan ışık miktarını arttırarak verimin neredeyse üç kat arttıracağını göstermiştir.

Diğer bir çalışmada ise; organik olarak modifiye edilmiş silika (ORMOSIL) DSSClerde çok işlevli bir yansıma engelleyici katman olarak kullanılmış, ışık yansıması engellenerek cihazın enerji üretim verimi arttırılmıştır. ORMOSIL kaplı DSSC yüzeyleri, her açıdan ve geniş bir dalgaboyu aralığından (400-800 nm) gelen ışığın yansımasına engel olmaktadır. Bu kaplama sonucunda, kısa devre akım yoğunluğu 0 dereceden gelen (normal) ışık için %23 artmış ve 30 derecelik bir açıda %84'e kadar çıkmıştır. Ayrıca, ORMOSIL kaplaması 155 derecelik bir temas açısına sahiptir ve dolayısıyla süperhidrofobik özellik göstermektedir.

Son olarak, kendiliğinden birleşme (self-assembly) yardımı ile üç boyutlu yapılar oluşturan peptit amfifil nanofiberlerinin kalıp olarak kullanımı ile TiO_2 nanotüplerin sentezlenmesi gösterilmiştir. Kullanılan peptit nanofiberler, geleneksel peptit yapılarına göre yüksek sıcaklıklarda daha dayanıklıdır. Düşük çaplara sahip olan bu fiberler tarafından oluşturulan üçboyutlu yapılar, yüksek yüzey alanlarına sahip olup, birbirine bağlı TiO_2 nanotüp yapılarının oluşturulması için etkili bir ALD kalıbı olarak işlev görmektedir. ALD, nanofiber yapılarının üniform ve yüzeyi tutarlı bir şekilde takip edecek şekilde kaplanmasını sağladığından bahsi geçen en/boy oranı yüksek peptit yapılarını kaplamak için ideal bir yöntemdir ve bu yüzden kullanılmıştır.

Anahtar kelimeler: Fotovoltaik, boya uyarımlı güneş pilleri (DSSCs), yüzey mühendisliği, atomik katman kaplama (ALD), metal oksitler, çinko oksit, titanyum dioksit geri yansitmasiz kaplama, peptit alttaşı, nanofiber.

Be less curious about people and more curious about ideas.

Marie Curie

ACKNOWLEDGEMENT

First and foremost I wish to thank my supervisor, Assist. Prof. Dr. Ali Kemal Okyay, for giving me the opportunity to occupy all the facilities and his invaluable academically and emotionally contributions throughout my entire graduate studies. He normally has a very busy schedule, but he would always find time to discuss my research progress. On the verge of finishing my master degree, I am so grateful for working with such an advisor within this field.

I would also like to say special thanks to Assist Prof. Ferdi Karadas and Prof. Ahmet Macit Özenbaş for attending my thesis committee.

It is a great pleasure to acknowledge all the professors, instructors, engineers, and graduate students at UNAM Materials Science and Nanotechnology Department. Also, I would like to thank to UNAM administration office and Ayşegul Torun, for their attention and favor during my graduation. I must also thank Nimet Kaya who helped me overcome many crisis situations at dormitory.

I gratefully acknowledge financial support by TÜBITAK (The Scientific and Technological Research Council of Turkey) under the project name BIDEP 2210-C M.Sc. fellowship.

Also, I express my heartfelt thanks to my undergraduate research advisors, Prof. Dr. Zeki Aktaş and Assoc. Prof. Dr. Emine Yağmur, from Chemical Engineering Department of Ankara University for their illuminating and friendly guidance, constructive criticism on various issues in my personally and academic life since the day I began my research as an undergraduate.

My sincere thanks also go to Assist Prof. Kağan Topallı for his insightful comments and encouragement in all the time of my study.

I am deeply thankful to my group members for providing an honest and friendly environment. Thank you to those who are my laboratory colleagues and fellows Kerem Çağatay İçli, Kinyas Polat, Tuna Demirbas, Ruslan

Garifullin, Bihter Dağlar, Sahin Beşerik, Hamit Eren, Zeliha Soran-Erdem, Talha Erdem, Yusuf Keleştemur, Fatma Kayacı, Yelda Ertaş, Aslı Çelebioğlu, Arif Khalily and Shahab Akhavan for always being kind, helpful and friendly. I want to acknowledge and appreciate their moral support, patience and kindness during my research. I owe my deepest gratitude to my dearest friends Nuray Gündüz, Pelin İşgor, Şeyma Canık, Burak Güzeltürk and Yildiz Gozde Sağlam for their help and transparency. I will never forget the awesome time we have had together and I feel very lucky to get to know such great people.

I feel the need to single out Amir Ghobadi, for his professional support valued, from whom I have learned many things and he never fed up to help me from the beginning to the end. I would not have been able to accomplish this task without his scientific knowledge, enthusiasm, experience and invaluable support.

And finally, without a doubt most importantly, I would like to thank my parents Şerife and Hakan, my siblings İpek and Emre, my aunt Şaziye and my uncle Mustafa for their sacrifices, understanding, patience and countless support all the time. I feel exceedingly lucky to have had these people in my life.

CONTENTS

ABSTRACT……..……..…….....III

ÖZET……..……..…….....V

ACKNOWLEDGEMENT……..……..…….VIII

LIST OF FIGURES…….…..XIII

LIST OF TABLES…..……..…….....XVIII

CHAPTER 1 INTRODUCTION ..... …1

1.1 MOTIVATION OF THE THESIS 3

1.2 ORGANIZATION OF THE THESIS.....3

CHAPTER 2 SCIENTIFIC BACKGROUND.....5

2.1 INTRODUCTION TO DYE SENSITIZED SOLAR CELLS (DSSCS) 5

2.1.1 DSSC INSPIRED BY PHOTOSYNTHESIS……5

2.1.2 ADVANTAGES OF DSSC…….7

2.2 BASIC STRUCTURE OF DSSC…….9

2.2.1 TRANSPARENT CONDUCTIVE OXIDE SUBSTRATE……...9

2.2.2 SEMICONDUCTOR PHOTOANODE……...10

2.2.3 DYE SENSITIZER……11

2.2.4 ELECTROLYTE……13

2.2.5 COUNTER ELECTRODE……...13

2.3 ELECTRON TRANSFER DYNAMICS OF DSSCS……...14

CHAPTER 3 CHARACTERIZATION METHODS…….19

3.1 MATERIAL CHARACTERIZATION 19

3.2 PHOTOVOLTAIC PERFORMANCE CHARACTERIZATION..... 19

3.2.1 CURRENT-VOLTAGE (I-V) MEASUREMENT..... 20

3.2.2 INCIDENT PHOTON TO-CURRENT CONVERSION EFFICIENCY (IPCE)..... 21

3.3 TIME-RESOLVED TRANSIENT CHARACTERIZATION 22

3.3.1 TRANSIENT OPEN CIRCUIT PHOTOVOLTAGE DECAY MEASUREMENT..... 23

3.3.2 TIME RESOLVED PHOTOLUMINESCENCE DECAY SPECTROSCOPY 23

3.4 OPTICAL CHARACTERIZATION 24

3.4.1 PHOTOLUMINESCENCE MEASUREMENTS..... 24

3.4.2 UV-VIS-NIR ABSORPTION..... 25

CHAPTER 4 SURFACE ENGINEERED ANGSTROM THICK ZNO SHEATHED TiO_2 NANOWIRES AS PHOTOANODE IN DSSC ... 26

4.1 INTRODUCTION 26

4.2 MATERIALS AND REAGENTS 28

4.3 SYNTHESIS OF TiO_2 NANOWIRES 28

4.4 ALD DEPOSITION 29

4.5 DEVICE ASSEMBLY 29

4.6 RESULTS AND DISCUSSIONS 29

CHAPTER 5 OMNIDIRECTIONAL ANTIREFLECTIVE COATINGS FOR PERFORMANCE ENHANCED DSSC 48

5.1 INTRODUCTION 48

5.2 MATERIALS AND REAGENTS 50

5.3 PREPARATION OF NANOPOROUS ORMOSIL COATINGS 50

5.4 PREPARATION OF NONPOROUS ORMOSIL COATINGS 51

5.5 PREPARATION OF THREE-LAYER COATING 51

5.6 DSSC ASSEMBLING 52

5.7 RESULTS AND DISCUSSIONS 52

CHAPTER 6 PEPTIDE NANOFIBER NETWORK TEMPLATED ALD-GROWN TiO_2 NANOSTRUCTURES FOR DSSC 59

6.1 INTRODUCTION 59

6.2 MATERIALS AND REAGENTS 60

6.3 SYNTHESIS OF PEPTIDE FOR 3D TiO_2 NANONETWORKS 60

6.4 PHOTOANODE FABRICATION 61

6.5 DSSC ASSEMBLING 62

6.6 RESULTS AND DISCUSSION 62

CHAPTER 7 CONCLUSIONS 69

7.1 KEY CHALLENGES AND RECOMMENDATIONS 70

7.2 CONTRIBUTIONS 71

CHAPTER 8 BIBLIOGRAPHY 73

LIST OF FIGURES

Figure 2.1: Light conversion analogy between photosynthesis and dye sensitized solar cell (DSSC). a) Sunlight is absorbed by chlorophyll. H_2O and CO_2 enter the stomata. Chemical energy is formed by water under light and consequently carbohydrates and oxygen are the outcome of rearrangement between chemical energy and carbon dioxide (yield=0.2%). b) Sunlight is absorbed by dye molecules which work as photosensitizer to make electrical energy. The photo-excited electrons are injected to the conduction band of the TiO_2 and collected by the external circuit. On the other side, holes complete the circuit by diffusion through the electrolyte mediator (yield>10%). 6

Figure 2.2: Conventional DSSC structure 9

Figure 2.3: a) Energy band diagram of conventional p-n junction under short circuit conditions; b) Charge separation under illumination.....15

Figure 2.4: Processes involved in sunlight conversion to the electricity inside a typical DSSC device 15

Figure 3.1: Current Density–Voltage (*J–V*) curve of a conventional DSSC under illumination.....21

Figure 4.1: Illustrative representations of (a) a 3D schematic of the TiO_2–ZnO core–sheath composite structure and (b) the related electronic dynamics of electron transfer in the DSSC. (c) TEM and HRTEM images of ZnO (10 ALD cycles)-coated TiO_2 NWs; the SAED pattern and HRTEM images in the inset prove the growth of a single crystalline rutile phase. (d) HRTEM image estimating the thickness of a ZnO sheath layer to be 1.3 nm for 10 ALD cycles. (e) SEM images (cross sectional) of densely-packed TiO_2 NW arrays. 30

Figure 4.2: XRD patterns of TiO_2–ZnO core–sheath composite structures for different ALD cycles of ZnO sheath layer. Diffraction peaks are in accordance

with a standard diffraction pattern of rutile structure of TiO2 with the prominent peak for (110) direction. 31

Figure 4.3: XPS spectra of a) Ti2p and b) Zn2p for TiO2-ZnO core-shell 32

Figure 4.4: Core-level XPS spectra of O1s from different ALD cycles coated TiO_2 deconvoluted to three different peaks indicating the presence of three types of oxygen, lattice oxygen (L_O), oxygen vacancy (V_O) and chemisorbed oxygen (C_O) 33

Figure 4.5: the ratio of the areas associated with V_O and C_O peaks to total area of O1s in which the concentration of V_O defect states stays almost constant after one cycle deposition of ZnO while C_O follows an upward trend.....33

Figure 4.6: Depiction of the mechanisms associated with water adsorption and dissociation.....34

Figure 4.7: PV parameters dependence on the ZnO deposition cycles on TiO_2 NWs in DSSC. (a) J -V curves and (b) The IPCE for the DSSCs consisting of the bare TiO_2 and ZnO coated TiO_2 core-shell composite photoanodes. The inset shows magnified image of the IPCE for wavelengths in the range of 400-600 nm. 37

Figure 4.8: Excited state electron radiative decay of N719 dye sensitizer for 0, 2 and 10 cycles ZnO coated TiO_2 NWs for an excitation of 370 nm. 38

Figure 4.9: The PL spectra for different ZnO cycles coated TiO_2 NWs samples for an excitation wavelength of 320 nm. All samples show a near band-edge emission (NBE) at 408 nm arising from e-h recombination across the conduction band (CB) and valance band (VB) of TiO_2 and a shallow surface defect traps emission (STE) centered at 424 nm. The inset shows the ratio of STE / NBE.....39

Figure 4.10: Electron recombination rates for different DSSC devices including bare TiO_2 NWs and TiO_2 NWs coated with different numbers of

ALD ZnO cycles obtained from transient photovoltage decay measurements. 41

Figure 4.11: The amounts of dye adsorbed on the surface of TiO2 NWs coated with different numbers of ALD ZnO cycles, showing a sharp increase for the sample coated with two cycles. For additional cycles,the adsorbed amount follows a gradual increase.....43

Figure 4.12: UV–Vis absorption spectrum of N719 sensitizer dye and max absorption is observed at 378 nm and 514 nm.....43

Figure 4.13: Concentration versus absorbance graph of N719 at 514 nm. The calibration curve of dye obtained from 5 different dye concentration (75, 62.5, 50, 25, 10, and 5 μM in 1 mL) and each sample immersed in 1mL of 1:1 ethanol–0.1 M NaOH solution for desorption of the dye. 44

Figure 4.14: CLs of a) Zn 2p3/2 and b)Ti 2p3/2 recorded on TiO_2 –ZnO heterojunction. All peaks have been fitted to Voigt line shapes using a Shirley background, and the VB values are determined by linear extrapolation of the leading edge to the baseline. 45

Figure 4.15: CLs and VB Spectra of Zn 2p3/2 and Ti 2p3/2 recorded on pure ZnO and TiO_2 samples (VBM values are determined by extrapolating of leading edge to the base line.).....45

Figure 4.16: 7 $(\alpha h\nu)^{1/2}$ versus hν plot for the bare rutile TiO_2 structure.....46

Figure 4.17: Energy band diagram of a DSSC showing band alignment in the TiO_2–ZnO interface. Some photoexcited electrons will be captured by the ZnO well, while the rest will be injected to the CB of TiO_2. The ZnO passivation layer will reduce recombination rates by reducing surface trap states at the interface and inducing surface band bending at the TiO_2 surface. 47

Figure 5.1: (a) Schematic of the DSSC design consists of MLAR ORMOSIL coating (three-layer anti-reflective (AR) coating) single side coated TCO glass substrate, titania paste as photoanode, dye as photosensitizer, electrolyte as

electron transfer mediator, Pt-coated conducting glass as counter electrode. This AR coating which is a superhydrophobic porous film can provide self-cleaning property of the cell, blue spheres and brown particles on the surface represent the water droplets and dirt molecules, respectively. (b) The schematic illustration of AR coating with three-layer and its effect on light reflection reduction through gradual increasing of the refractive indices as 1.1, 1.2, 1.4, respectively to match it to the bare glass refractive index (1.5). (c) Top view SEM images of three-layer porous thin film. The inset shows the water contact angle of the surface which is 156° indicating superhydrophobic property of the porous film. (d) Higher magnification SEM image of the surface. 54

Figure 5.2: Transmission spectra of uncoated glass, ORMOSIL coated glass and glass after bladed of AR coating 55

Figure 5.3: (a) Variations of UV-Vis optical transmittance spectra for the ORMOSIL coated (blue) and uncoated (red) samples. For the whole range, 300nm-800nm, the amount of transmittance has increased and an average increase of 6.5% is recorded for visible spectrum. (b, c, d) One-to-one comparison of J_{SC}-V characteristics of the ORMOSIL coated cells under different incident angles of incoming wave (0°, 15°, 30°). The ORMOSIL coating has been removed by razor blade and acetone and used as the uncoated sample. It is shown that the amount of J_{SC} has increased by 23%, 32.1% and 84.6 % for different incident angles of 0°, 15°and 30°, respectively. 57

Figure 5.4: IPCE curves are collected in a wavelength range of 250nm-600nm for the both ORMOSIL coated and uncoated cells. The amplitude of maximums located at 370nm and 520nm are improved by about 19% and 11%, respectively. The three-layer coating significantly improves IPCE efficiency for the solar cell. 58

Figure 6.1: Representative image to nanostructured TiO_2 network.....62

Figure 6.2: SEM images of 3D TiO_2 nanonetworks a-c) before and d-f) after calcination (bar scale: 1 µm).....64

Figure 6.3: TEM images of 3D TiO_2 nanonetworks a-c) before and d-f) after calcination. (bar scale: 50 nm).....64

Figure 6.4: Raman of 3D TiO_2 nanonetworks for different ALD cycles 65

Figure 6.5: αhϑ2 versus hϑ plot for TiO_2 templated structures with different ALD cycles and corresponding band gaps of 3.39, 3.33, 3.24, respectively...66

Figure 6.6: DSSC devices with 100,150 and 200 cycles templated TiO_2 a) *J-V* curves b) IPCE curves 67

LIST OF TABLES

Table 2.1: Analogy of subsystems between photosynthesis and DSSC 7

Table 4.1: Atomic concentrations extracted from XPS survey scans 32

Table 4.2: J–V parameters for the experimental devices with different ZnO ALD cycles under AM 1.5 G filtered spectral illumination at an incident intensity of 100 mW/cm^2. 36

Table 4.3: Results obtained from XPS valence band spectra 47

Table 5.1: Photovoltaic parameters for the ORMOSIL coated photoanode in DSSC with different incident angles under AM 1.5 G filtered spectral illumination at an incident intensity of 100 mW/cm^2. 56

Table 6.1: *J–V* parameters for the experimental devices of 3D TiO_2 Networks AM 1.5 G filtered spectral illumination at 100 mWcm^{-2}.....68

Chapter 1 Introduction

Since the industrial revolution, starting from several decades ago, energy concern is the most vital issue for today's modern society. On the other side, population explosion continues and consequently demands for energy supplies are skyrocketing. This unavoidable gap between the limited energy resources and ever-increasing demand will be more pronounced moving toward halfway through this century. The upcoming energy crisis does not only have an effect on economic and political status of the society but also it will be closely attributed to health and environmental issues. How and to what extent each country will be influenced is debatable. It can be said that the energy use is directly proportional to living standards determined by a worldwide factor called the human development index (HDI). HDI is an analogical measure of progress—a composite index of life expectancy, years of schooling and income [1]. What we can understand from HDI is that as more electricity is used, higher HDI increases and better standard of living is obtained.

Since the investment of fossil fuels, the human's main source of energy was provided by this resource. According to U.S Energy Information Administration (EIA) [2], the contribution of different energy resources consist of oil (37%), natural gas (28%), coal (18%), nuclear (8%), and renewable energy (9%) such as biomass (4.4%), hydro (2.8%), wind (1.5%), geothermal (0.2%) and solar (about 0.4%). It is expected that traditional sources will continue its major contribution to world's energy mix till the end of 2020 with an ongoing decline out to 2050. Therefore, now more than ever before, several ongoing interests have motivated the societies around the globe to harvest alternative and renewable energy sources such as solar cell, fuel cell, wind power, geothermal energy, biomass, hydroelectric and so on. Renewables are expected to grow rapidly and supply just fewer than 13 percent of the energy needs by 2040 with EIA forecasts. Since there is a tremendous capacity in solar energy due to the expected energy generation capacity of 23000TWy/year, solar energy regarded as one of the most reliable, abundant, clean energy sources among different renewable energy sources,

and it allows energy generation in remote areas. That's why we need to use solar in an efficient way to produce electricity. Photovoltaic (PV) systems convert the energy of the light coming from the sun (photons) into electricity and they are commonly known as "solar cells". This process is coined as the photovoltaic effect. This effect was discovered first by Becquerel in the late 1830s. In 1905, A. Einstein won the Nobel Prize with the explanation of photoelectric effect. There was a big breakthrough in 1954 because the first crystalline silicon solar cell was invented in Bell Telephone Laboratories (4%). After 4 years, it was used on an electrical power for a space satellite called Vanguard I and launched in 1958.

Following the world energy crisis in the mid-1970s, companies realized that crystalline Si solar cells would be so expensive in the future, so great efforts and millions of dollars were spent to build cheaper and more efficient solar cells for residential and commercial uses. In 1976, David Carlson and Christopher Wronski fabricated the first amorphous Si photovoltaic cell consisting of the major portion of the present world PV market including power rural health clinics, refrigeration, water pumping, telecommunications, off-grid households and modern flat panel displays. Amorphous form of silicon (a-Si) is considerably cheaper material than its crystalline form used in traditional solar cells.

In the 1980's, the solar PV became a popular power source for consumer electronic devices, including calculators, watches, radios, lanterns and other small battery-charging applications [3]. There was a steady progress towards higher efficiency solar cells and the first thin film solar cell exceeded 10% efficiency using copper sulfide/cadmium sulfide at the University of Delaware.

Starting with 90's, there were large scale production of GaAs, other III-Vs, $CuInSe_2$ and CdTe based multi-junction solar cells with more than 15% efficiency. Despite the revolutions in utilizing new semiconductors for achieving high efficiency solar cells, a new path was discovered for photovoltaic community through the use of organic semiconductors. At first, it

was found that soluble fullerene derivatives (as acceptors or n-type semiconductors) connected to soluble p-type semiconductors (donors) can make a layered structure which will efficiently convert the light into the electricity. This generation of solar cells can easily be made through a simple coating technique. After emergence of this type of solar cells, nanostructured inorganic-organic hybrid solar cells (Dye sensitized solar cell and organic solar cells) were proposed as a promising approach to further lower production costs and provide efficient solar energy conversion. Since the invention of DSSC in 1991 by Micheal Grätzel and Brian O'Regan, a lot of attentions have been paid on these "state of art" PV devices. This thesis is on this type of solar cells.

1.1 Motivation of the thesis

Global energy crisis is a lingering problem that world is facing because the gap between energy supply and demand is significantly increasing day by day. In order to circumvent this problem, solar energy option amongst renewable energies can be considered as the most abundant and promising alternative energy sources.

Our motivation in this study is to make a bridge between our knowledge and current-to-future solar cell technologies. For this aim, in this thesis, we have developed photoanodes for performance enhanced dye sensitized solar cells which are the most successful approach of artificial photosynthesis. We will propose three main ideas to improve PV performance of typical DSSC designs and the contribution of each of these ideas in the device overall performance would be scrutinized.

1.2 Organization of the thesis

This thesis consists of eight chapters. The following chapters are outlined below:

Chapter 1 points out energy crisis and gives general information about photovoltaic cells, its historical background and current-future status.

Chapter 2 provides basic information about device structure, key components, operation principle and impact of different factors on device photovoltaic functionality. Here we review the recent trends in development of DSSC technology.

Chapter 3 gives the detailed information about the characterization methods including materials, photovoltaic performance, time-resolved transient and optical characterizations.

Chapter 4 presents our study on surface engineered angstrom thick ZnO-sheathed TiO_2 nanowires as photoanode in DSSCs and gives details of experimental methods, presents the results of fabricated device and discusses the reason behind this enhancement in the device efficiency.

Chapter 5 discusses multifunctional antireflection coatings for omnidirectional reduction in the surface reflection and provides information about the materials, experimental techniques and device preparation steps.

Chapter 6, peptide nanofiber network templated ALD-grown TiO_2 nanostructures are investigated as the photoanode for DSSC. The details of the proof-of-concept devices are also presented.

Chapter 7 concludes the whole thesis providing a summary of the completed projects and explains key challenges with recommendations to solve them.

Chapter 2 Scientific Background

2.1 Introduction to Dye Sensitized Solar Cells (DSSCs)

Dye Sensitized Solar Cells (DSSCs), also called Gratzel cell, as a third generation solar cell technology, includes new and innovative structures compared to thin film and conventional silicon solar cell technologies. DSSC was introduced for the first time over 20 years ago by Gratzel and co-workers who demonstrated the emulation of the light absorption and electron flow of photosynthesis by different elements to produce electricity [4].

Up to now, DSSC has reached efficiencies up to 15 % on small laboratory scale cells and sub modules of 8 % efficiencies have been reported by companies which lead this technology closer to market and commercial applications.

2.1.1 DSSC Inspired by Photosynthesis

Photosynthesis is of paramount importance for plants, single-cell organisms and also for animate beings that require oxygen. An understanding of photosynthesis is so valuable because it uses low energy starting materials triggered by harvested sunlight energy and during chemical reactions water and carbon dioxide is converted into chemical energy stored in simple sugars (glucose). Thus, the first idea of making DSSC was inspired by principles and materials of the photosynthesis process [5] which consist of complex sequence events, but simply it has two stage processes. The first stage is light-dependent reactions since solar energy is required and the second one is the dark (light-independent) reactions due to lack of need to solar energy.

***Light dependent reactions*:**

In these reactions, sunlight triggers the movement of electrons (electrical current) to cause the chemical change on the -thylakoid membranes- innermost

membrane of the chloroplast. During the light-dependent reactions, chloroplasts absorb solar energy and two energy storing molecules (Adenozin trifosfat ATP as chemical energy and reducing agent, oxidized dihydro-nicotinamide-adenine-dinucleotide phosphate, NADPH as reducing agent) are produced. At the same time, water molecules are split which causes oxygen release (as a by-product) and this is an essential part of photosynthesis process.

***Dark (light-independent) reactions*:**

During this process, energy stored in ATP and NADPH is consumed for simple sugars (such as glucose) formation from carbon dioxide taking placed in the –stroma- cytoplasm" of the chloroplast. The produced sugars such as glucose are stored as chemical energy for later energy source of usage at cellular respiration or its conversion to organic molecules (proteins, carbohydrates, fats/lipids, or cellulose and so on) by the cells. The below chemical equation simply summarizes the overall photosynthetic reaction

$6CO_2 + 6H_2O + sunlight \rightarrow C_6H_{12}O_6 + 6O_2$ where, carbon dioxide and water are ultimately converted to carbohydrates and oxygen.

To have better understandings on the analogous between photosynthesis and DSSC, we can clarify the imitation in the following way:

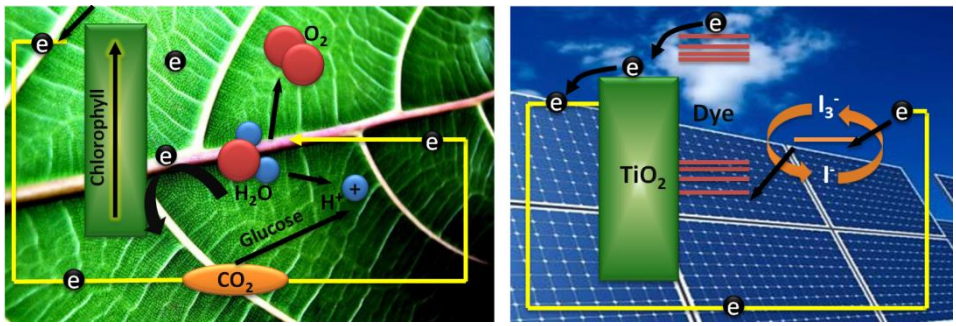

Figure 2.1: Light conversion analogy between photosynthesis and dye sensitized solar cell (DSSC). a) Sunlight is absorbed by chlorophyll. H_2O and CO_2 enter the stomata. Chemical energy is formed by water under light and consequently carbohydrates and oxygen are the outcome of rearrangement between chemical energy and carbon dioxide (yield=0.2%). b) Sunlight is absorbed by dye molecules which work as photosensitizer to make electrical energy. The photo-excited electrons

are injected to the conduction band of the TiO_2 and collected by the external circuit. On the other side, holes complete the circuit by diffusion through the electrolyte mediator (yield>10%).

DSSC is a photoelectrochemical system which behaves like a molecular machine based on a photosensitive pigment and it consists of organic and inorganic materials (see Table 2.1). In the Gratzel cell light absorbing pigments such as chlorophyll are replaced by the organic dye monolayer. The water is replaced by electrolyte and split oxygen as an electron donor and oxidation product, respectively [2],[3]. Furthermore, the wide band gap nanostructured semiconductor layer (porous titanyum dioksit/titania nano-structure) is analogous to the chloroplast in leaves, in that it mimics the naturally occurring light absorbing protein called NADPH as a scaffold for the self- assembly of dye molecules per volume and finally carbon dioxide acts as the electron acceptor.

In natural photosynthesis, the existing NADPH inside the thylakoid membrane acts as chlorophylls and carotenes arranger in a specific and fixed orientation with respect to each other. By this way, vectorial energy transfer to the photosynthetic reaction centers can be optimized. That's why it can be said that TiO_2 has a dual role in DSSC since it acts as an electron acceptor and charge carrier transport layer [8].

Table 2.1: Analogy of subsystems between photosynthesis and DSSC

Subsystem	Photosynthesis	DSSC
Electron acceptor	CO_2	TiO_2
Electron Donor	H_2O/O_2	Electrolyte
Photon Absorber	Chlorophyll	Dye

2.1.2 Advantages of DSSC

The solar cell technology can be grouped in three generations: crystalline solar cells (~350 µm film thick) as the first one [9], thin film solar cells (~1 µm film thick) including $CuInGaSe_2$, CdTe, a-Si:H etc. as the second and organic based solar cells [10], dye-sensitized solar cells (DSSCs) [11],

quantum dot solar cells [12], and recently emerged perovskite solar cells as the third generation solar cells [13].

Although silicon based solar cells have high efficiencies, but they are so expensive mainly due to the energy intensive purification and crystallization processes. In contrast, thin film solar cells cost much less and use less material but they have lower efficiencies. To come to grips with the complexity of cost and efficiency, third generation solar cells are emerged with low cost production techniques, together with relatively high efficiencies. Owing to extensive recent efforts spent on this generation, currently the prices of third generation solar cells continue to drop while their efficiencies are approaching to the limits of the silicon based photovoltaic technology. The major advantages of DSSC listed below over other first and second generation solar cells enable it to be used for various functions and cell configurations in DSSC:

- The materials used in DSSC are non-toxic, environmental friendly.
- Low-cost processing equipment which make DSSC vastly cheaper than that of silicon solar cells. Therefore, more surface area can be covered for an equivalent cost.
- Low sensitivity to nonstandard conditions of solar incidence angle, temperature and irradiation (shadow and ambient temperature change). Even, when the temperature heats up from 20 to 60 ºC, it operates in an efficient and stable way. However, conventional Si cells exhibit a significant decline over the same temperature and reach an amount of approximately 20% of their nominal efficiency.
- DSSC is a bifacial cell which provides capturing light from all angles and both sides.
- It shows multi-color range possibilities achieved by changing the dye, either organic or inorganic.
- The performance of DSSC is stable for a long period of time [4].
- It can be flexible which this in turn provides innovative device structures.

2.2 Basic Structure of DSSC

The typical architecture of DSSC is constructed from negative electrode (so called working electrode or photoanode) which is sensitized with organometallic dye molecules as light absorbing layer and platinized glass cathode as a counter electrode, placed in front of photoanode with a parallel configuration (Figure 2.2). The space (~40 μm) between two isolated electrodes is commonly filled by the liquid iodide/tri-iodide redox couple due to its good stability and reversibility acting as the hole conducting media.

The mesoporous n-type wide band gap inorganic semiconductor layer plays a key role as photoanode in the device. In the conventional DSSC, titanium dioxide (TiO_2) layer (~10μm) has interconnected architecture with anatase phase and diameter of ~10-20 nm deposited on optically transparent conductive oxide electrode (TCO, generally florine-doped tin oxide glass). Dye sensitized solar cell with high efficiency is achieved through the molecular engineering of porphyrin sensitizers. In following part, we will explain each component in detail.

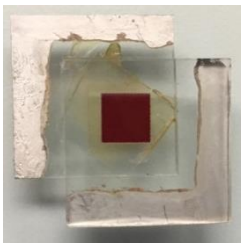

Figure 2.2: Conventional DSSC structure

2.2.1 Transparent Conductive Oxide Substrate

Transparent conductive oxide (TCO) substrates have been heavily used in various types of solar cells and other optoelectronic applications owing to their unique properties. This family of conducting substrates can provide low sheet resistance together with having high transparency which makes them an excellent option for designing high efficiency solar cells such as DSSC. Particularly, low sheet resistance will increase the collection efficiency of the

DSSC and due to its transparency most of the light will reach to the sensitized photoanode. Apart from these remarkable optical properties, TCOs can sustain under harsh chemical environment and keep their durability through high temperature processes such as sintering.

In general, there are different types of metal oxide transparent conducting substrates. The most typically used compounds are; fluorine doped tin oxide (FTO), indium doped tin oxide (ITO), aluminum doped zinc oxide (AZO) and gallium doped zinc oxide (GZO) [14]. Among all of these compounds, FTO and ITO are the most popular options for device applications. Industry standard ITO can provide a sheet resistance as low as $5\Omega sq^{-1}$ and a transparency of 90% over the visible spectrum. However, indium is not earth abundant and due to its limitations such as mechanical fragility, non-compatibility on strong acid environment and having high sheet resistance at high temperatures, FTO is highly preferred for DSSC application [15]. Currently, most of the DSSCs are constructed using FTO glass substrates with 8-15 Ω/sq resistance and 80% transmittance at 550 nm. FTO coating on glass substrates is performed generally by physical vapor deposition systems and other deposition systems like spray pyrolysis.

2.2.2 Semiconductor Photoanode

Wide band gap metal oxide semiconductors are generally preferred for the photoelectrode layer in DSSCs. The band gap of these semiconductors is typically larger than 3eV to provide high transparency of the photoanode over the whole UV-Vis-NIR spectrum. Several morphologies can be utilized to make this semiconducting layer including, colloidal nanoparticles (NPs) [16], nanowires [16],[17] (NWs), nanotubes [19] (NTs) and other highly branched three dimensional structures [20]–[22]. The most widely used design architecture consists of TiO_2 colloidal NPs paste. This morphology can ensure an effective surface area for dye adsorption desired for high performance DSSCs. However, the discontinuities among NPs will impose an unavoidable increase in the recombination between the photogenerated carriers and electrolyte species which consequently reduced the collection capability of the

cell. However, NWs and NTs will introduce a continuous 1D structure in which the probability of electron recombination will considerably reduce compared to that of NP based DSSCs, but they would offer much less surface area. In addition to these various types of designs, the choice of the metal oxide semiconductor layer is another factor which can be used to optimize the device efficiency [23],[24]. Chemical stability, high electron mobility and high adhesion to TCO are the most important requirements for this layer. SnO_2 [25], ZnO [26],[27], Nb_2O_5 [28],[29], ZrO_2 [30],[31] and TiO_2 are the potential metal oxides which are examined in DSSC structures. Although, TiO_2 is the mainly utilized semiconductor for DSSC due to its high stability, high photocatalytic activity, ZnO with mobility much higher than that of TiO_2 is one of the favored options to replace TiO_2 based cells. However, it was demonstrated that ZnO was never replaced with TiO_2 for high efficiency DSSC application due to its low photo electrochemical activity [26], [27].

Up to now, the highest efficiency of the DSSC was attained by using TiO_2. Taking all of these factors into consideration, it is clear that different factors related to semiconductor photoanode are one of the key factors on the cell efficiency. Type of the semiconductor layer, design architecture and substantial treatments can be conducted to improve device efficiency.

2.2.3 Dye Sensitizer

Sensitizer is the major component of the DSSC which acts as absorbing active layer of the cell. Primarily, it absorbs incoming photons over wide range of solar spectrum from UV to near IR region. This photon will generate the electron and hole pairs via excitation of an electron from HOMO (highest occupied molecular orbital) to LUMO (lowest unoccupied molecular orbital) of the dye. Afterwards, this electron will be injected to the conduction band of the photoanode and it will be collected through this layer and hole will be conducted by the electrolyte toward the counter electrode layer.

Dye has a function to absorb light and create electron and hole pairs. Therefore, the absorption capability of the dye through the solar spectrum is

one of the main factors for attaining high efficiencies. In recent years, different types of dyes were prepared with the main goal of 1) increasing the extinction coefficient of the dye and 2) extension of the dye absorption tail toward visible and NIR region 3) good adsorption (chemisorption) to semiconductor layer depending on the molecular structure 4) high injection yield of excited electrons into semiconductor layer with a faster response compared to its relaxation to ground state (valence band), 5) having stable oxidized form allowing it to be regenerated by an electrolyte and 6) stable long life time (108 cycle turnover, nearly 20 years). In total, there are three classes of photosensitizers: metal complex sensitizers [32], metal-free organic sensitizers [33], and natural sensitizers [34]. However, transition metals based photosensitizers have been demonstrated to be the most suitable option so far. Especially, polypyridyl complex of ruthenium with one or more carboxylic acid groups becomes the main product and they are used to develop other dyes. Generally, the carboxyl groups on the dye will assist an effective adsorption of the dye to the mesoporous photoanode. Moreover, a considerable increase in the efficiency of DSSC can be achieved with utilization of metal to ligand charge transfer (MLCT) which is the case for N3 dye. MLCT modifies the electron position from Ru to the p* orbital and consequently increases the electron injection capability of the dye to the conduction band of TiO_2. It should be noted that in MLCT, HOMO level of dye molecules are positioned near to metal particles and oppositely LUMO level of the dye molecules are positioned near ligands. Furthermore, N719 dye was obtained through engineering of the N3 bond structure. N719 shifts the conduction band of TiO_2 positively and increases the open circuit voltage of the cell. Although these dyes are able to provide nominal efficiencies for the DSSC but both of them can absorb the light efficiently below the 600nm. Therefore, a new dye was invented; N749 or black dye which was able to extend the light absorption to longer wavelengths and consequently more current density is produced. On the other end of the scale, Z907 was another dye studied to solve the stability problem of the above dyes at temperature of nearly 80 ºC. Z907 dye does not show any degradation for 1000 hours at 80

ºC. As it can be clearly seen, all of the studies performed in this area are aiming to tackle with a specific deficiency of the dye such as light absorption and thermal stability.

2.2.4 Electrolyte

Another component of the DSSC is the electrolyte. Electrolyte is a liquid based charge transport layer; its main function is to regenerate the dye after injection of an electron to the photoanode. Also, this layer is hole transport layer to transfer positive charges to the counter electrode layer. The long-term stability of DSSCs is defined by electrolyte [35]. Thus, to obtain a proper working electrode following requirements should be met: (1) fast electron diffusion with the help of low viscosity, small redox species and high electrical conductivity (2) high efficient interfaces of electrolyte/semiconductor and electrolyte/counter electrode (3) low imposing degradation of dye or desorption of the dye from the photoanode surface (4) low absorbing light in the visible region.

At the end of this section, it should be noted that there were a lot of studies on the development of new electrolytes to get long-term stability. Electrolytes for DSSCs can be categorized into three types: liquid electrolytes [36], solid state electrolytes [37], and quasi solid state electrolytes [38]. The most frequently used one is liquid electrolytes (organic and ionic electrolytes) with a redox couple.

2.2.5 Counter Electrode

The counter electrode (cathode) is used for the reduction of the oxidized species of electrolyte. For proper operation, the counter electrode should have good catalytic activity. The redox species reduction in cathode is faster than anode. To date, the most preferred catalyst is platinum which maintains the reduction reaction fast as well as high transparency, but its performance mainly depends on deposition techniques on TCO substrate such as thermal decomposition of hexachloroplatinic salt in isopropanol, electro deposition,

sputtering, vapor deposition, and screen printing. Here, the main point which should be considered related to Pt catalyst is its performance reduction in time and catalytic activity is deteriorated due to its removal off of the substrate (etching) in the presence of electrolyte. In addition, it is an expensive metal and its preparation requires high temperature fabrication methods (400ºC), thus graphene [39], activated carbon [40], conductive polymers [41] have been investigated as alternative materials for cathode; however, their electrical efficiencies were not as high as Pt catalyst.

2.3 Electron Transfer Dynamics of DSSCs

It should be noted that photovoltaic processes in DSSC such as charge separation is different from conventional p-n junction based solar cells. In p-n junction the separation is assisted by built-in electric field across the interface. However, this process is originated from kinetic competition of the excited electrons at the organic/inorganic interface in DSSC.

Solar energy is converted to electrical energy by means of several kinetic-based processes involved inside the solar cell. As shown in **Figure 2.3**, in the case of conventional p-n junction solar cells, the kinetic is different from the DSSC. When an n-type material comes to the contact with a p-type material, the depletion region will be created at the interface of the p-n junction. As the consequence of this depletion region, a built-in potential will be made in which this potential separates electron and hole pairs. Afterward, electrons will transport via n-type semiconductor and holes will diffuse inside the p-type layer. Considering all of these explanations, all processes including light absorption, charge separation and charge collection are occurred at semiconductors in which these semiconductors can be same or different. However, due to the small dimensions of the photoanode particles in the DSSC, the possibility of depletion region formation is negligible and it works based on kinetic competition of the carriers at organic/inorganic interface. DSSC is a photo electrochemical device in which all of the injection,

collection and absorption processes occur at different materials. As the result of these dynamic processes photocurrent and photovoltage are produced.

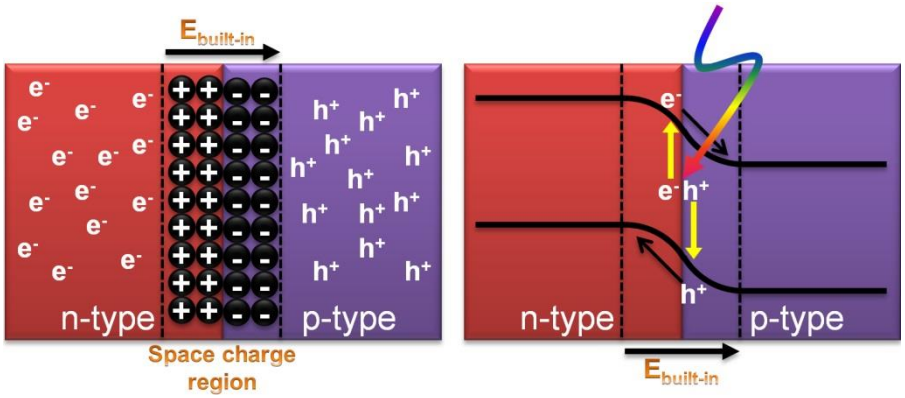

Figure 2.3: a) Energy band diagram of conventional p-n junction under short circuit conditions; b) Charge separation under illumination

This photovoltage is equal to differences between the Fermi level of the semiconducting photoanode and the electrolyte redox potential. A number of processes (photoexcitation, electron injection, electron collection, dye regeneration, recombination) that occur inside the cell during its operation can be illustrated in Figure 2.4 and following related reactions are summarized.

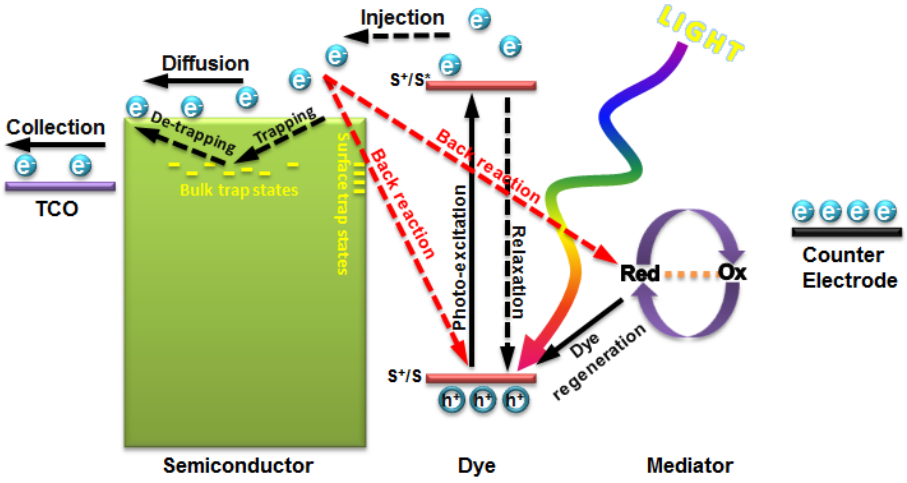

Figure 2.4: Processes involved in sunlight conversion to the electricity inside a typical DSSC device

1. $Photoexcitation: S + h\vartheta \rightarrow S^* \sim fs$

2. $Electron\ Injection: S^* \rightarrow S^+ + TiO_2{}^- \sim 100ps$

3. $Dye\ Regeneration$:

$2S^+ + 3I^- \rightarrow 2S + I_3^- \sim 1\mu s$

$I_3^- + 2e^-(cathode) \rightarrow 3I^-(cathode) \sim ms - s$

4. $Recombination\ (back\ reaction)$:

$back\ reaction\ to\ electrolyte: I_3^- + 2e^-(TiO_2) \rightarrow 3I^-(anode) \sim ms - s$

Back reaction to dye: $S^+ + e^-(TiO_2) \rightarrow S \sim \mu s - ms$

Cell: $e^-(Counter\ electrode) + h\vartheta \rightarrow 3I^-$

1. Photoexcitation

When a photon with energy higher than the band gap of the dye comes to the ground state (S) of the dye molecules adsorbed on the photoanode, it generates the electron and hole pairs. During this process, the electron will be excited to the excited state (S*) and hole will stay at the ground state (S). Some portion of these excited carriers will come back to their unexcited state through a relaxation process which is typically a ~ few femtosecond process [42] [43].

2. Electron Injection

After photoexcitation of the dye and before relaxation across the dye band gap, some of the electrons on the excited state will be injected to the conduction band of the semiconductor photoanode layer. Obviously, to have this process possible, the conduction band of semiconductor layer should be at lower energies than the excited state of the dye. The injected dye electrons will be positioned to the conduction band minimum of the photoanode layer via a process called thermalization. Another driving force comes from the entropy differences between the dye and photoanode. Electrons are tending to move in the direction of photoanode due to large number of delocalized states compared to dye molecules. Final mechanism is created by the anchor carboxyl group of dye molecules. To supply the adsorption of dye to

photoanode, a photon is donated from anchor group to photoanode. Therefore, the photoanode surface is more positive and dye surface more negative which help to separate charges and reduce recombination [44]. While both photoexcitation and electron injection take place at few femtosecond (fs) and sub-picosecond (sub-ps) scales, respectively, electron relaxation from excited state to ground state occurs at a nanosecond (ns) range [43]. Therefore, it is relatively much slower than injection time and ensures a high injection yield. On the other side, dye will lose one electron and it becomes an oxidized product. So the dye (S*) becomes (S^+).

3. Electron Collection

The injected electrons will come to the conduction band of the semiconductor and will be collected by FTO layer. During the collection process, these electrons diffuse inside the TiO_2 conduction band and experience several trapping/de-trapping processes before reaching to the collector. The existence of surface or bulk trap states and the contact between the electrolyte and TiO_2 layer can reduce device efficiency considerably by a process called recombination. It is possible for the electrons to recombine with the holes in the dye valance band or electrolyte species (it has been found that the second one is dominant). On the other hand, the existence of the surface and bulk defect states can reduce the collection capability of the device via trapping the electrons. The capability of the electron is mainly depended on the morphology, crystallinity and the mobility of the semiconductor.

4. Dye regeneration

As explained above, when a dye molecule gives an electron to the semiconductor, it turns to an oxidized product. Therefore, there would be a mechanism to regenerate the dye. This occurs with the help of the electrolyte. An electron will pass from the counter electrode (Pt) to the electrolyte to provide the reduction reaction. In other words, the electron is transferred to the electrolyte where it reduces the oxidant species, Ox. Subsequently, the

reducing agent formed, Red, oxidizes the excited dye, S^+, and returns it to the inactive/ground state, S.

As an instance, for the most typically used I^{3-}/I^- (triiodide / iodide) redox couple, I^{3-} reduced to iodide ion I^- and subsequently, electron transfers back to the dye molecule. Afterwards, iodide ion reforms to triiodide and dye molecule will return to inactive state (S). Here, I^{3-} and I^- is called as an oxidizing molecule and reducing molecule, respectively. This regeneration process takes place in a μs time scale [42],[43].

5. Recombination

The main detrimental process responsible for device performance is charge recombination. Recombination of the injected electrons is one of most restricting factors which reduce device efficiency considerably. The recombination of the carriers is an unwanted process in which electrons are captured with other species before getting collected at the TCO. This process is mainly between two routes; the reaction between 1) the injected electrons and dye holes and 2) the injected electrons and redox species. Although both mechanisms are responsible for device efficiency reduction but the portion of second process is supposed to be dominant. This recombination, -also called back reaction of the electrons, is a millisecond (ms) scale phenomenon. Therefore, compared to injection response time (which is at the order of 100 ps) its response is quite slow and a big portion of the electrons can be collected by TCO. However, this process has still undeniable detrimental effect on device performance and its impact should be mitigated. In recent years, several studies have been performed to retard electron back reaction and reduce the recombination rate of the carriers. Together with all of these mechanisms, a part of this recombination can occur through trap states in which this localized energy states trap the electrons and pass it to redox species. Considering all of these facts, a low recombination rate can be achieved with proper design structure in that electron back reaction is delayed and surface trap states are passivated.

Chapter 3 Characterization Methods

The experiments and characterizations are conducted in the UNAM Cleanroom Facilities (UCF) (class 100 and 1000), Okyay Group Laboratories and other characterization laboratories in UNAM at Bilkent University.

3.1 Material Characterization

Non-destructive analysis technique of X-ray diffraction (XRD) has been utilized to investigate the crystalline phase and morphology of the photoanodes. This has been carried out by X-ray diffractometer (XRD, model Panalytical X'pert Multi-Purpose) and patterns have been collected in the range of $2\theta = 20 - 80°$ using Bragg–Brentano geometry (Cu K$\boldsymbol{\alpha}$). Scanning electron microscope (SEM, FEI – Quanta 200 FEG, operated at 10 kV) and transmission electron microscope (TEM, Tecnai G2-F30, FEI, operated at 200 kV) have been employed to characterize the morphology and dimensions of the structure. TEM samples are prepared on a holey carbon coated copper grid. Selected area electron diffraction (SAED) analysis is also utilized to identify the growth direction and crystallinity of the nanowires. Investigations on constituent elements at the surface of the samples have been done using X-ray photoelectron spectroscopy (XPS, Thermoscientic K-Alpha, Al K-Alpha radiation, hυ=1486.6 eV). Moreover explorations on 1) the band alignments at the core shell interface, 2) elemental analysis and presence of surface defects, have been assisted by XPS performed at survey mode by operating flood gun to prevent charging surfaces. In addition to this, a contact angle meter (OCA 30, Dataphysics) is used to obtain static contact angles of coated samples by using 4µl dispersed water droplet onto the surface.

3.2 Photovoltaic Performance Characterization

The photovoltaic cells have been characterized with home-made current-voltage (I-V) measurement setup and incident photon-to-current conversion efficiency (IPCE) setup.

3.2.1 Current-Voltage (I-V) Measurement

Current-voltage *(I-V)* or current density-voltage *(J-V)* characteristic is a standard analysis technique to measure the photovoltaic performance of the solar cell. This measurement was carried out using a Keithley 2400 source-meter which is integrated with a AM 1.5 G Newport 67005 solar simulator under a 100 mW/cm^2 solar light irradiation.

"*AM*" is the abbreviation for air mass, so *AM* 1.5 implies that the light has to travel 1.5 times farther than direct incidence would before reaching ground level. The power of the incident light, P_{in}, can be adjusted by the distance between the light source and the device, and it is calibrated at a fix amount.

Upon applying light with a well-defined spectrum and intensity (A.M 1.5G solar simulation) to a solar cell and measuring its *I-V* response, several solar parameters can be deduced as demonstrated in the **Figure 3.1** and equations. The important parameters are open circuit voltage (V_{OC}), short circuit current density (J_{SC}) and fill factor (*FF*) and efficiency ($\boldsymbol{\eta}$) which can be used to compare with different devices. The maximum power, $P_{max,,}$ of the solar cell is obtained from multiplication of I_{MP} and V_{MP}. The open circuit voltage (V_{OC}) is the potential difference for the case that the net current flow is zero (when I = 0, resistance $\rightarrow \infty$). The short circuit current (I_{SC}) is the max current flow at the cell under zero voltage bias (when V = 0, resistance $\rightarrow$ 0). Often short current density *(Jsc)* is preferred which defines the ratio of photogenerated current to electrode active area. Fill factor (FF) is the ratio of the maximum power (P_{max}) of the device to the theoretical maximum power (product of V_{OC} and I_{SC}) which defines the measure of squareness of the *I-V* curve. Higher resistance and more recombination in a solar cell reduce the FF. The power conversion efficiency, η, of a solar cell is defined as the ratio of P_{max} to P_{in} per area. It is the ratio of output energy to the input energy.

$$P_{max} = V_{max} * I_{max}$$

$$\eta = \frac{P_{max}}{P_{in}}, \qquad FF = \frac{P_{max}}{I_{SC} * V_{OC}}$$

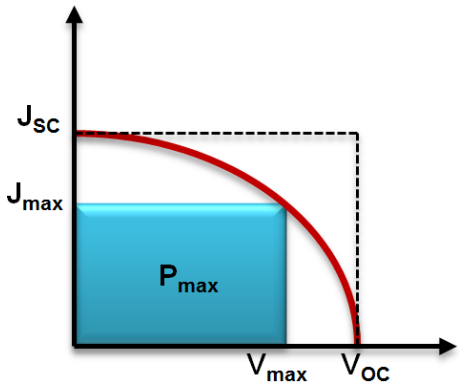

Figure 3.1: Current Density–Voltage (*J–V*) curve of a conventional DSSC under illumination

Shape of the *I-V* curves can deviate from a sharp square mainly due to the effect of parasitic resistances. Shunt (R_{SH}) and series (R_S) resistances are effective in solar cells and they reduce the fill factor and efficiency [15].

3.2.2 Incident photon to-current conversion efficiency (IPCE)

Incident photon-to-current conversion efficiency (IPCE) is a characterization technique which provides information about how efficiently the device converts photons as a percentage into electrons (current) at each wavelength.

For this aim, a Xenon lamp (150 W) is utilized as an illumination source of the light. Monochromatic light is achieved with a 1200 lines/mm grating and it is chopped by a mechanical chopper at a frequency of 10 Hz. The illuminated monochromatic light has been focused on the sample surface and the cell is biased using a Keithley 2400 source-meter. The voltage of gate terminal is separately biased with a Keithley 2400 voltage supply. A lock-in amplifier is employed to detect and measure the photogenerated current through the anode and cathode ports. In an ideal case, series connection of lock-in amplifier for photocurrent measurement is advised.

The outcoming optical beam has dimensions of 400 μm (width) and 1200 μm (length). To calibrate and measure the incident power density in every single frequency, a calibrated Si photodetector (Newport 918D-UV-OD3R) with a

1.1cm-long efficient detection range (which is much wider than the incoming spot) is used.

As explained, the monochromator that we use utilizes a 1200 lines/mm diffraction grating to selectively produce our desired single frequency light from the white incident light. But it should be mentioned that due to the reflections off the diffraction grating, polychromatic light can be made. Therefore, together with the desired wavelength (λ), the polychromatic light is also comprised including second (λ/2), third (λ/3) and larger harmonics (λ/n) of the desired wavelength [54-56]. To suppress the existence of these higher order modes, a 500 nm high-pass filter at (Newport FEL0500) is employed in all of our measurements that are beyond the 500 nm.

The monochromator was incremented through the UV and Visible spectra to generate the *IPCE* (λ) as defined below

$$IPCE(\%) = \frac{number\ of\ electron\ generated}{number\ of\ incident\ photons} \times 100$$

$$IPCE(\%) = \frac{1240 \times J_{photo}(mAcm^{-2})}{\lambda(nm) \times I_{inc}(mWcm^{-2})} \times 100$$

where λ is the wavelength, J_{SC} is short-circuit current density ($mAcm^{-2}$), and I_{inc} is the incident power intensity (Wcm^{-2}).

3.3 Time-resolved Transient Characterization

In all solar cells, the incoming light generates electron-hole pair carriers that have a probability to meet their conjugate carriers and recombine with each other. In general, recombination means a dissipation of the free energy provided by the photons to heat inside the cell. In solar cell device recombination reduces the efficiency of power conversion efficiency and it is a must to keep its contribution as low as possible. To scrutinize all of these kinetic processes, a proper time-resolved characterization can provide valuable information about this few micro/nano seconds processes.

3.3.1 Transient open circuit photovoltage decay measurement

In DSSC injected electrons from LUMO level of the dye molecules into the TiO_2 conduction band minimum can go on a back reaction and recombine with either ionic redox species or oxidized dye molecules through an interfacial charge transfer. The probability of this recombination with ionic redox species is proved to be the dominant. One of the best ways to explore this phenomenon is open circuit photovoltage decay measurement. The V_{OC} decay measurement is a relatively simple method firstly introduced at ([45]) for exploration of the recombination kinetics in DSSC. Upon cutting off the light illumination on the DSSC device at V_{OC}, the excess electrons in the conduction band of TiO_2 will be removed through the recombination with the holes, and the rate of photovoltage decay is proportional to lifetime of the electrons by below expression:

$$\tau_n = -\frac{k_B T}{e}\left(\frac{dV_{OC}}{dt}\right)^{-1}$$

Slower recombination rate means longer electron lifetime which this in turn shows an induced retardation in recombination of the carriers.

In this thesis, the open circuit voltage decay measurement has been carried out with a homemade setup. A R&S®RTM2000 digital oscilloscope has been triggered with a chopper working at 0.1 Hz and an attenuator is used to adopt different intensities on the sample. Therefore, cells were illuminated with a white light steady-state bias at different intensities. Then the voltage transient response and its exponential decays are recorded with an oscilloscope using a sampling rate of 10 ns which is triggered with a signal having frequency of the chopper, as explained before.

3.3.2 Time resolved photoluminescence decay spectroscopy

Another transient technique, used in this study, is time resolved photoluminescence decay (TRPL). This technique is useful tool to investigate lifetime decay kinetics of fluorescent materials. Using this technique which

was firstly explored by ([46]), the kinetics of electron injection from dye states to the conduction band of TiO_2 can be addressed. Since excited state decay kinetics are quite sensitive to molecular level interactions and dynamics, many different phenomena (e.g. rotation, diffusion, molecular conformations, molecular binding, energy transfer, charge transfer, etc.) can be directly observed through fluorescence decay curves.

In our laboratory, we use a time correlated single photon counting (TCSPC) system having a time resolution down to 4 ps (PicoHarp 300) integrated with a picosecond pulsed laser with an output central photon energy of 3.37eV driven by a driver module (PDL-800 series) capable of delivering laser pulses with 80 MHz repetition rate. The system utilizes a fast photo multiplier tube (PMT) (Hamamatsu H5783 series) to resolve lifetimes on the order of tens of picoseconds. In our case, we excited the samples with a light having a wavelength of 350 nm and recorded the number of recombined carriers dynamic at 600 nm to understand the injection yield of our sample.

3.4 Optical Characterization

Optical characterizations have been performed using Cary Eclipse Fluorescence Spectrophotometer for photoluminescence measurements and Cary 5000 and Microplate Reader are used for UV-Vis-NIR absorption and transmission measurements.

3.4.1 Photoluminescence measurements

Fluorescence Spectroscopy (Varian Eclipse) is a useful technique to investigate the material properties and dynamics taking place at nano scale due to high sensitivity of the photo-physical properties of the materials to even small changes in the molecular level. Using this analysis, one can estimate that the amount of surface defect states at the surface of semiconductor. The main principle of operation of these tools relies on spectrally selective excitation of the samples. Accordingly, you excite your sample with a stream of photons having energies higher than the semiconductor bandgap. As the consequence

of this excitation, electrons will take apart from holes and will be excited to the conduction band. When excitation is switched off the excited states of electrons will be relaxed through the recombination with their counterparts at valance band. If this recombination is between conduction band and valance band, it is called band-to-band emission. But sometimes, this phenomenon occurs through a trap state which can be located anywhere inside the band gap of the semiconductor. Therefore, the emission from this trap-assisted recombination will lead to an emission at energies lower than the band gap of the semiconductor.

Photoluminesence (PL) measurement is in general the emission of the light upon an optical excitation. In our case, we employ a 300 nm excitation and the emission spectrum is collected between 360 nm and 600 nm. In this study, PL measurement is applied for all samples to gain insight on the density and energetic locations of the defects of the TiO_2 nanowires surface and to investigate the passivation effect of the ultrathin ZnO layer on the TiO_2 NW surface of the core-shell heterostructure, noting that PL intensity correlates directly with the defect densities.

3.4.2 UV-Vis-NIR Absorption

UV-VIS-NIR Spectrophotometer (Cary 5000, Varian) is employed to explore the optical properties of the semiconductor. The effective optical band gap has been estimated using transmission data of UV-Vis-NIR Spectrophotometer. Also, the amount of N719 dye adsorbed on the surface of photoanode is measured by using a Microplate Reader (Spectramax M5).

Chapter 4 Surface Engineered Angstrom Thick ZnO Sheathed TiO_2 Nanowires as Photoanode in DSSC

This part is based on the publication "Surface engineered angstrom thick ZnO-sheathed TiO_2 nanowires as photoanodes for performance enhanced dye-sensitized solar cells", **T. G. Ulusoy**, A. Ghobadi and A. K. Okyay, J. Mater. Chem. A, 2014, **2**, 16867. Reproduced (or "Reproduced in part") with permission from The Royal Society of Chemistry. Copyright 2014, Journal of Materials Chemistry A.

4.1 Introduction

To date, in order to increase the light harvesting efficiency of DSSCs, new organic dyes with higher extinction coefficients and broader absorption spectra are being investigated [47]–[50]. In addition, approaches that yield large surface area are utilized to further increase PV efficiency via higher dye loading. Colloidal crystalline nanoparticle based TiO_2 films that provide high surface area, are the most widely used type of photoanodes in DSSC technology. However, the disordered state hinders efficient charge transport in the TiO_2 film due to low effective charge carrier mobility and high carrier recombination rate. To improve charge transfer efficiency, one dimensional (1D) structures such as nanotubes and nanowires (NWs) are desirable since they provide higher mobility and lower recombination rate in addition to high surface area [17],[51],[52]. Moreover, hierarchical oxide nanostructures, which can provide high surface area for dye uptake and 1D highly branched structure for better light scattering and overall light conversion efficiency, has turned to a hot research topic in recent years [20],[53] .

Recently, there is a rapidly growing interest among the DSSC community towards the optimization of the interfacial layer between dye and inorganic photoanode. Substantial improvement in DSSC performance could be attained by engineering the dye-TiO_2 interface in order to 1) reduce recombination of charge carriers by both passivation of surface state traps in the interface and

retardation of photo-injected electrons' back–transfer from TiO_2 conduction band to the oxidized red-ox species, 2) increase injection yield and collection efficiency of photogenerated carriers from dye to TiO_2, 3) increase light absorption efficiency by enhancing the amount of dye uptake. Several studies show that high band-gap metal-oxide materials such as In_2O_3, ZrO_2, Al_2O_3, Nb_2O_5, Ga_2O_3 and SiO_2 could reduce recombination in DSSC by blocking back-transfer of electrons and hence barricade the recombination of electrons with either oxidized dye molecules or with the oxidized redox couple (the latter one is thought to be particularly dominant in device performance degradation) [54]–[59], or via reducing the density of surface trap states on TiO_2 surface [55],[60]. Besides, some studies demonstrate that metal-oxides like Nb_2O_5, $SrTiO_3$, ZrO_2 and Al_2O_3 can contribute in device performance enhancement by inducing a surface dipole in metal-oxide/dye interface which leads to a negative shift of TiO_2 conduction band [44] and enhancement in injection yield of photo-induced electrons [61]. In addition to improved electrodynamics at the interface, researchers in [44],[62] explain device performance improvement to be related to dye adsorption enhancement. Materials such as ZnO, MgO, ZrO_2 and Al_2O_3 with high isoelectric point (IEP) compared to TiO_2 can provide more favorable host sites for carboxylic groups which allows higher amounts of dye uptake onto the surface of TiO_2 NWs as opposed to bare ones [63]. The increased dye loading yields increased amount of light absorption. However, a serious drawback with most of the high band gap materials is that forward electron injection (dye to TiO_2) can be significantly impeded and electron injection efficiency could be totally diminished if the interfacial layer is merely a couple of nanometer thick. To tackle this problem, recently, researchers have proved that electron transfer rate could be systematically tailored proposing ultrathin tunneling layers by using a variety of coating methods. Dip-coating is one of these methods which has been commonly utilized to coat electrodes [56],[57]. However, this technique typically shows non-uniform thicknesses as well as presence of pinholes on the surface which creates unwanted conduits for electron back transfer [66]. Contrary to this method, atomic layer deposition (ALD)

technique, a self-limiting growth process, offers uniform and conformal coating of non-line-of-sight surfaces including high aspect ratio features (like dense micrometer long NWs as in our case). Although the ALD has lower cost effectiveness compared to other deposition techniques, it ensures uniform and conformal coating of a pinhole-free angstrom-thick metal-oxide layer through the whole substrate surface which is an imperative task to improve material/device performance especially in high aspect ratio features [20],[53],[56],[58].

Taking all these factors into consideration, this work aims to investigate the effect of ZnO interfacial layer on the PV performance of DSSC devices, hydrothermally-grown TiO_2 NWs are coated with different ALD cycles of ZnO.

4.2 Materials and Reagents

Ethanol, acetone, titanium butoxide ($Ti(OCH_2CH_2CH_2CH_3)_4$) (97%) and hydrochloric acid HCl (36%) are all from Sigma–Aldrich Co and used as received. FTO coated glass (7 Ω sq-1), photosensitizer dye Ruthenizer 535-bis TBA (N719), Iodalyte HI electrolyte are all purchased from Solaronix. For ZnO deposition by ALD, diethylzinc ($(C_2H_5)_2Zn$ or DEZn, Sigma-Aldrich) and HPLC-grade water (H_2O) are used as the zinc and oxygen precursors, respectively.

4.3 Synthesis of TiO_2 Nanowires

TiO_2 NWs are prepared on FTO glass based on hydrothermal technique. First, FTO glasses are ultrasonically cleaned for 15 min sequentially by using ethanol; acetone and de-ionized (DI) water and then dried by N_2 flow. Concentrated HCl (20 ml) and DI water (20 ml) are mixed in a teflon-lined stainless steel autoclave (45 ml) for 10 min and afterward 0.8 ml titanium butoxide is added. The mixture is stirred for an additional 30 min under ambient conditions. FTO is placed into solution with the conducting side facing up with 45° angle against the autoclave wall. The hydrothermal reaction

is performed at 140 °C for 4 hours in an oven. Prior to taking out, the FTO glass is cooled to room temperature in air inside the autoclave. The NWs then rinsed extensively with DI water and dried in air.

4.4 ALD Deposition

Finally NWs are coated with ZnO by ALD reactor (Cambridge Nanotech Savannah S100). The substrate temperature was kept at 250 °C during the ALD process using DEZn at 80 °C and distilled water. The pulse and purge time for both is kept to be 0.015s and 10s, respectively. The deposition was carried out using successive different cycles (1, 2, 3, 4, 10) of ZnO as an ultrathin layer on TiO_2 NW arrays with the estimated growth rate 1.3 Å per cycle.

4.5 Device Assembly

The ZnO coated TiO2 NWs are kept at 80 °C for 15 minutes before being soaked in 0.5 mmol N719 in a t-butanol/acetonitrile (1:1, in volume ratio) solution, for 24 hours at room temperature. The samples are rinsed with acetonitrile to remove non-chemisorbed dye molecules. The drilled Pt-coated conducting glass is used as counter electrodes bonded to TiO_2 NWs by 25µm-thick thermal sealant (Dupont). The active area of each cell is filled with electrolyte driven by capillary force through the hole. The area of the electrode was controlled using a mask of 0.30 cm^2 area on the hot-melt sealed film.

4.6 Results and Discussions

In this study the main objective is to enhance DSSC device performance by interface modification of TiO_2 NWs using angstrom thick ZnO sheath. To achieve such a thin layer, ALD with different cycles of ZnO is used on TiO_2 nanowires produced by hydrothermal technique. Figure 4.1 illustrates the 3D schematic of the device consist of TiO_2-ZnO core-shell composite structure and related electron transfer dynamics. The proposed DSSC device consists of four main parts: (1) a composite photoanode formed by hydrothermally-grown

TiO_2 NWs on transparent conducting glass (FTO, F:SnO_2-doped, Tec 7 Ωsq^{-1}) coated with a conformal layer of sub-nanometer ZnO as the sheath layer; (2) cis-bis (isothiocyanato) bis (2,20-bipyridyl-4,40-dicarboxylato) ruthenium(II) (N719) as a photosensitizer; (3) an iodide/tri-iodide (I^-/I^{-3}) shuttle as the hole transfer mediator; and (4) Pt-coated conducting glass as the counter electrode.

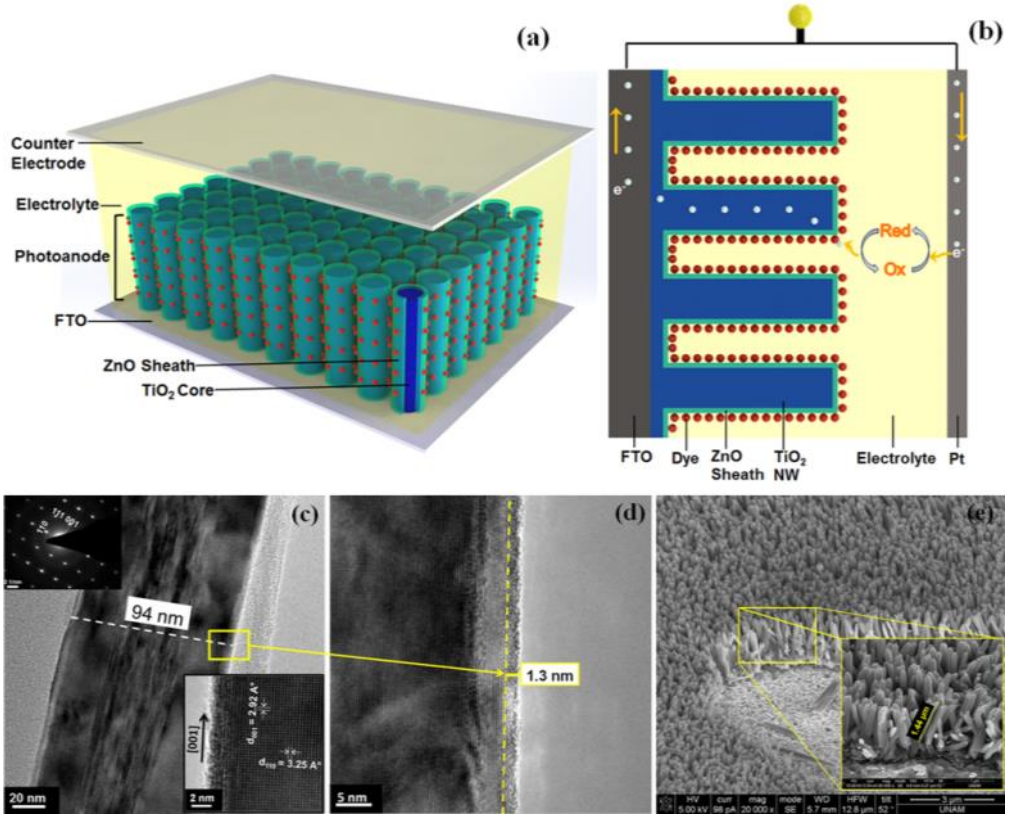

Figure 4.1: Illustrative representations of (a) a 3D schematic of the TiO_2–ZnO core–sheath composite structure and (b) the related electronic dynamics of electron transfer in the DSSC. (c) TEM and HRTEM images of ZnO (10 ALD cycles)-coated TiO_2 NWs; the SAED pattern and HRTEM images in the inset prove the growth of a single crystalline rutile phase. (d) HRTEM image estimating the thickness of a ZnO sheath layer to be 1.3 nm for 10 ALD cycles. (e) SEM images (cross sectional) of densely-packed TiO_2 NW arrays.

Figure 4.1c shows the TEM image of an individual nanowire has diameter between the range of 80-100 nm. In this figure inset, SAED pattern examined along the [110] zone axis which is perpendicular to the NW side walls reveals that hydrothermally grown TiO_2 was single crystalline with interplanar spacings of d_{110} = 3.25 Å and d_{001} = 2.9 Å which results in rutile phase grow along the [001] direction. Also, HRTEM image of composite photoanode

displayed the wurtzite ZnO (as confirmed in [67]**)** passivation layer grown on TiO_2 NWs sheath conformally (see Figure 4.1d). Since it is difficult to distinguish shell layer from core below 10 ALD ZnO cycles to our knowledge, we take this image for 10 ALD cycles and find 1.3 nm-thick which yields a growth rate of 1.3 Å per cycle. It should be noted that the growth rate of ZnO on the NW sample is lower than that of 1.55 Å [67] reported rate for planar structure stemming from slow diffusion of the gas precursor into NWs. Also, SEM image shows the length of densely packed nanowires on FTO substrate is about 1.2-1.6 µm (see Figure 4.1e). To examine crystalline structure and the orientation of the TiO_2 NWs for the TiO_2-ZnO core-shell photoanodes, XRD analysis is conducted. As shown in Figure 4.2, XRD spectra proves that the strong rutile peak for (110) direction and the TiO_2 diffraction peaks are in good agreement with the standard diffraction pattern of rutile TiO_2 structure (JCPDS, 82-0514). Since ZnO shell layer associated peak was not able to observe due to its ultrathin thickness, the all XRD spectra for different ALD ZnO cycles are quite similar to bare TiO_2 NWs.

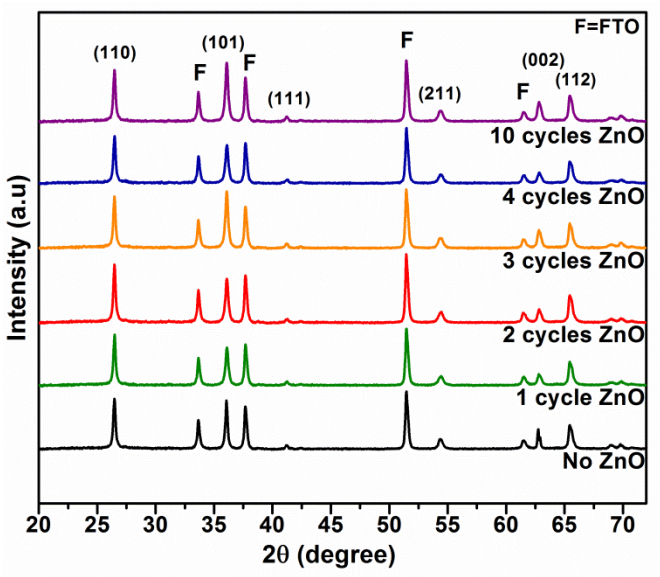

Figure 4.2: XRD patterns of TiO_2–ZnO core–sheath composite structures for different ALD cycles of ZnO sheath layer. Diffraction peaks are in accordance with a standard diffraction pattern of rutile structure of TiO2 with the prominent peak for (110) direction.

Moreover, XPS measurement is performed to verify the existence of such a thin ZnO layer and determine the elemental compositions on the core-shell surfaces. Figure 4.3 provides the XPS spectra of the Ti2p and the Zn2p, and C1s peak signal calibrated to 284.8 eV. The spin orbit splitting between the peaks of Ti2p3/2 and Ti2p1/2 are found as 5.7 eV and the peak positions are in good agreement with the reported values [68],[69]. In addition, Zn2p spectrum with 1/2 and 3/2 spin-orbit doublet components is located at 1045.24 eV and 1022.18 eV, respectively which are also in line with the literature [70]. As shown in Figure 4.3a, quite symmetric Zn2p peaks noticeably intensifies which have uniform bonding states by additional ALD cycles of ZnO, and after 4 cycles the Ti2p peak is widening because of the chemical state mixing at the composite interface shown in Figure 4.3b.

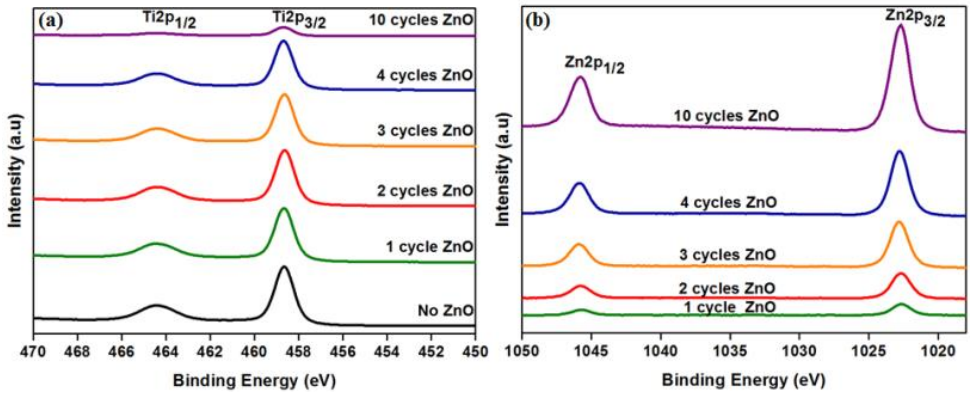

Figure 4.3: XPS spectra of a) Ti2p and b) Zn2p for TiO2-ZnO core-shell

Further evidence for the formation of ZnO layer, the surface elemental compositions are investigated and we observed that as ZnO ALD cycles increases, the ZnO proportion increases on the surface (see Table 4.1).

Table 4.1: Atomic concentrations extracted from XPS survey scans

# of ZnO ALD cycles	Ti 2p %	O 1s %	Zn 2p %	C 1s %	Zn/(Ti+Zn)%
0	30.49	62.54	-	6.96	**0**
1	26.41	55.37	2.71	15.51	**9.30**
2	26.37	58.32	5.88	9.42	**18.23**
3	24.02	54.47	9.41	12.1	**28.15**
4	23.12	55.26	13.67	7.96	**37.16**
10	11.33	40.18	41.07	7.42	**78.38**

Moreover, we deduced the existence of the surface defects from core-level O1s spectra for all samples. For this aim, O1s spectrum is deconvoluted into three peaks as shown in Figure 4.4.

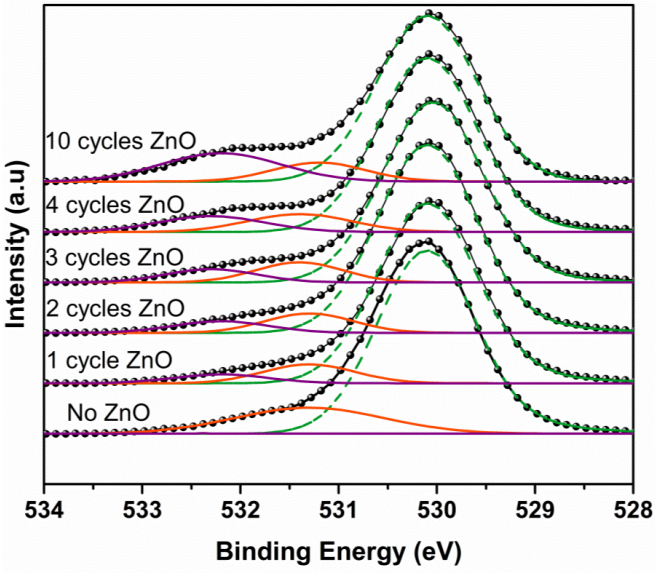

Figure 4.4: Core-level XPS spectra of O1s from different ALD cycles coated TiO_2 deconvoluted to three different peaks indicating the presence of three types of oxygen, lattice oxygen (L_O), oxygen vacancy (V_O) and chemisorbed oxygen (C_O)

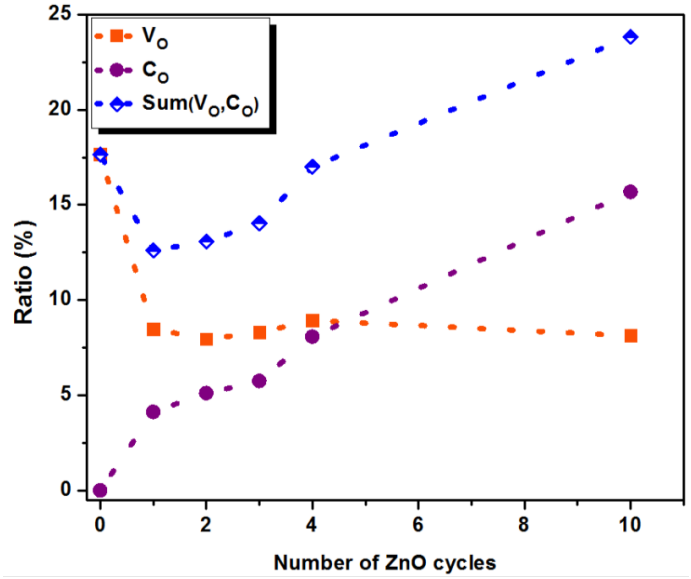

Figure 4.5: the ratio of the areas associated with V_O and C_O peaks to total area of O1s in which the concentration of V_O defect states stays almost constant after one cycle deposition of ZnO while C_O follows an upward trend

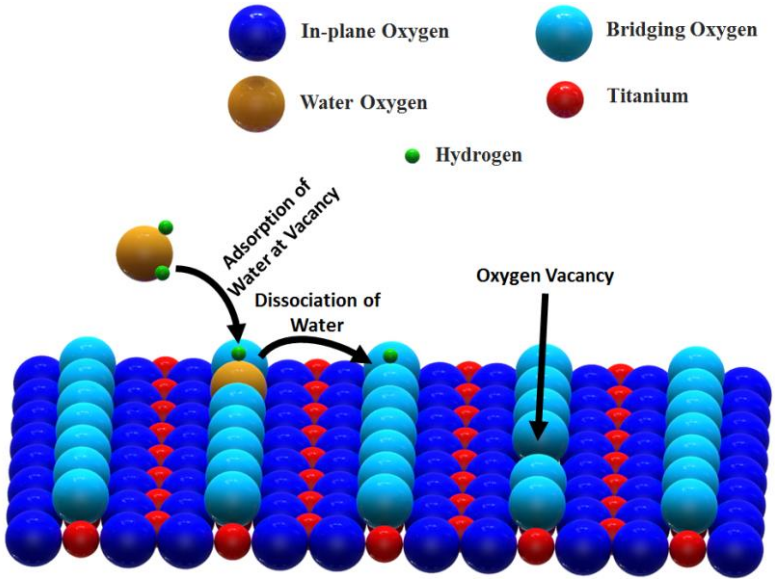

Figure 4.6: Depiction of the mechanisms associated with water adsorption and dissociation.

Here, we determined the main peak located at 530 eV can be attributed to lattice oxygen bond (L_O) to Ti^{+4} ions in TiO_2. The other peaks centered at 531.4 eV and 532.4 eV can be assigned to oxygen vacancies or defects (Vo) and chemisorbed or dissociated oxygen species (Co) on the TiO_2 surface, respectively [71],[72]. It should be implied that L_O, V_O and C_O peaks have same binding energies with angstrom thick ZnO shell layer [73],[74]. Also, hydroxyl groups which are physically adsorbed on the surface can be easily desorbed due to the ultrahigh vacuum condition of XPS system [75]. Keeping these in mind, we use three independent Gaussion function for fitting all samples because as we mentioned that there is no new Gaussian component which belongs to ZnO coated samples.

Results from Figure 4.4 illustrate that for bare TiO_2 sample oxygen-defect regions are present in the surface layer but no peak is related to C_O species (its peak value is roughly 4 orders of magnitudes smaller than V_O related peak). By deposition of 1 cycle ZnO layer on TiO_2 core, the concentration of defect states (V_o) is reduced sharply and in the meantime the small shoulder at 532.4 eV (Co) is observed. It proves that TiO_2 surface is partially coated with hydroxyl groups (i.e, -OH, H_2O) which are strongly bound to the surface defects. Shifting to thicker layers of ZnO shell, the area related to V_O shows a

nearly constant feature while the concentration of C_O radicals rises almost linearly. C_O peak is becoming more significant for 10 cycles coated sample. As already mentioned, for the surface modification of TiO_2 NWs, ALD method is employed. In the ALD process of ZnO, at first, substrate is exposed to the gaseous precursor molecule of water vapor. According to the calculation of free energy in the classical nucleation theory, most of the water-derived hydroxyl groups such as OH radicals and H_2O will be chemisorbed near the imperfections such as defects (like V_O levels) or grain boundaries and smaller concentration on Ti_{5C} sites away from the vacancies [76]–[79]. Therefore, at the position of oxygen vacancy, Ti atoms presented at the TiO_2 surface make bonds to the water induced hydroxyl groups and subsequently water-induced H ion is chemisorbed on neighbor bridging oxygen atoms [75],[76] (The schematic of these process are shown in Figure 4.6). Consequently, it is expected that the ZnO shell layer can passivate (or fill) oxygen vacancy defects by adding an oxygen-containing molecule attached on the surface of TiO_2. Furthermore, the shell layer introduces new trapping sites due to adsorbed hydroxyl groups. A better qualitative comparison among different samples can be attainable by determining the relative areas under each Gaussian component. In this sense, the ratio of the areas associated with V_O and C_O peaks to the total area of O1s spectrum is shown in Figure 4.5. The sum of these ratios is also provided in the same figure.

As it can be clearly seen, sum of two ratios has a minimum amount at 1 cycle where together with efficient passivation of V_O defect states, the concentration of C_O species is also sufficiently low. As the thickness of ZnO shell layer increases, the proportion of sum (V_O, C_O) and C_O shows a similar increasing trend.

The device photovoltaic characterization for 1, 2, 3, 4 and 10 ALD cycles of ZnO coated nanowires are evaluated using solar simulator under AM1.5G conditions. The results obtained from photovoltaic characterization including the short-circuit current density (J_{sc}), the fill factor (FF), and overall conversion efficiency ($\boldsymbol{\eta}$) are presented in Table 4.2 and *J-V* performances of devices

based on TiO_2-ZnO composite photoanodes are compared in **Figure 4.7**a. From the data shown, shifting to thicker layers of ZnO shell it is apparent that J_{sc} increases and at 2 cycles it reaches the highest of 8.826 mA/cm^2. After 2 cycles, there has been a sharp decline to 1.652 mA/cm^2 at 10 ZnO cycles. In contrast to J_{sc} trends, V_{oc} increases gradually following 2 cycles and exhibit its maximum value as 0.77 V at 10 cycles with the poorest efficiency.

Table 4.2: J–V parameters for the experimental devices with different ZnO ALD cycles under AM 1.5 G filtered spectral illumination at an incident intensity of 100 mW/cm^2.

# of ZnO ALD cycles	**Voc (V)**	**Jsc (mA/cm^2)**	**FF**	**η(%)**
0	0.71	3.643	0.43	1.12
1	0.70	5.500	0.49	1.90
2	0.70	8.826	0.49	3.03
3	0.73	6.333	0.44	2.04
4	0.75	5.367	0.36	1.43
10	0.77	1.652	0.31	0.40

Note: Reference = 0 cycle. Values given are mean values of 4 cells prepared in a similar way. Experimental errors of the mean values are within ± 10 mV for V_{oc}, ± 0.20 mA/ cm^2 for J_{sc} and ±0.5 % for FF.

In summary, the best photovoltaic device efficiency of 3.03% (J_{sc}=8.826 mA/cm^2, FF=0.49) was obtained at 2 ALD cycles of ZnO-sheated TiO_2 NWs which is almost 3 times higher than TiO_2-only DSSC with the efficiency of 1.12% (J_{sc}=3.643 mA/cm^2, FF=0.43). It should be noted that *Jsc* can be deduced from absorption of light power over the solar spectrum, thus IPCE measurement is vital for understanding the reason behind of great increment in J_{SC}. In Figure 4.7b, there is a substantial enhancement of UV light absorption for devices with ultrathin ZnO layer, whereas, their IPCE values are nearly disappeared at visible wavelengths [82]. A positive correlation can be considered between the IPCE quenching in visible range and conduction band alignment of TiO_2- ZnO core-shell design that captured photogenerated electrons at ZnO layer and in the meantime injecting through the interface.

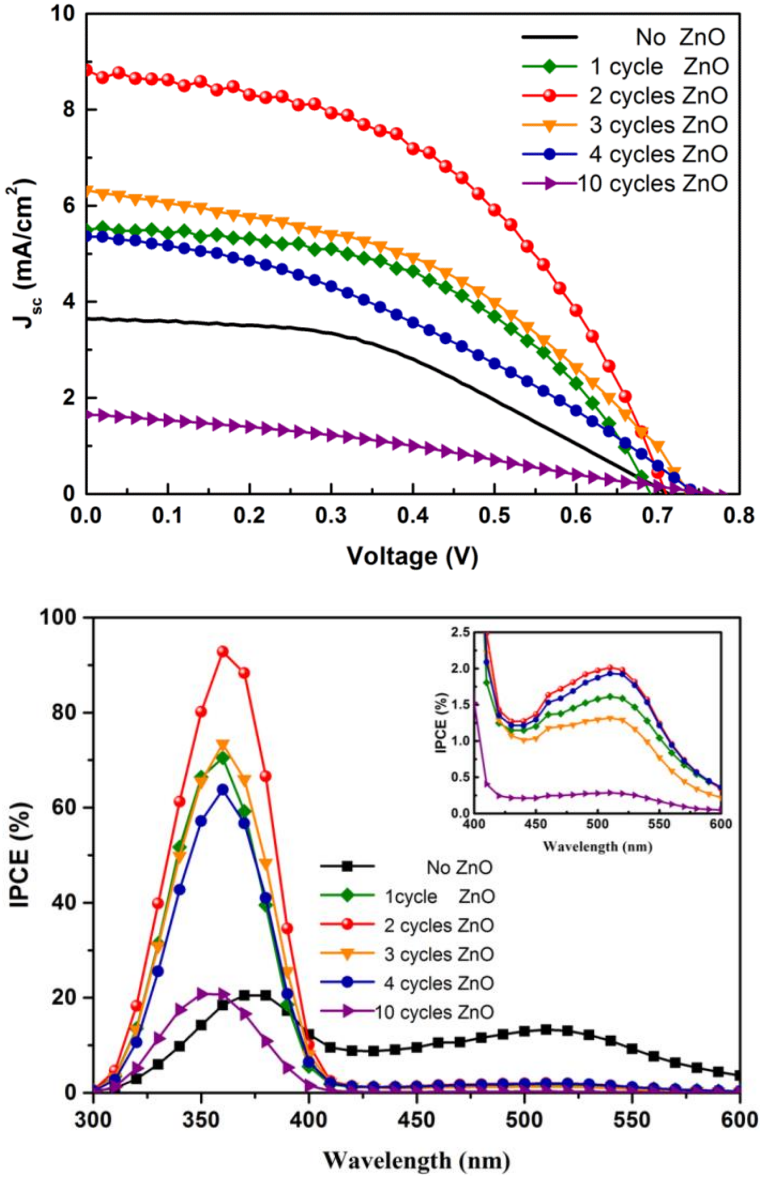

Figure 4.7: PV parameters dependence on the ZnO deposition cycles on TiO_2 NWs in DSSC. (a) J -V curves and (b) The IPCE for the DSSCs consisting of the bare TiO_2 and ZnO coated TiO_2 core-shell composite photoanodes. The inset shows magnified image of the IPCE for wavelengths in the range of 400-600 nm.

To further elaborate the mechanisms of the injection ability for photoexcited electrons into the conduction band of photoanodes in the DSSCs, time-resolved single photon counting (TRSPC) is performed as proposed by Koops et al [46]. The injection efficiencies are monitored by the excited state emission decay of the adsorbed dye for 0, 2 and 10 ALD ZnO cycles coated photoanodes (see Figure 4.8). It shows that as shifting to thicker ZnO shell layers the emission decay is delayed gradually. This means that the thicker ZnO width will capture more electrons and consequently the injection yield of

photoinduced electrons will reduce. So this loss should be somehow compensated by retardation in recombination kinetics of the injected electrons at the interface or by suppressing the activity of surface trap states at TiO_2 surface. In other words, an optimized thickness of ZnO overlayer can yield to an enhanced efficiency by providing an effective balance between injection and recombination.

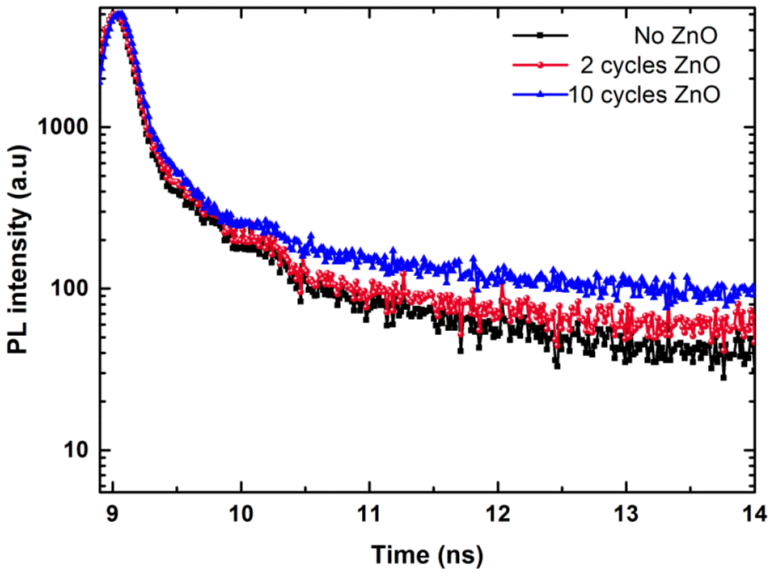

Figure 4.8: Excited state electron radiative decay of N719 dye sensitizer for 0, 2 and 10 cycles ZnO coated TiO_2 NWs for an excitation of 370 nm.

Taking all previous results into consideration, it should be noted that the mobility of the carriers in organic semiconductors is very sensitive to surface traps [83]; such defect states can reduce collection efficiency of the device through the trapping of injected electrons. On the other hand, based on XPS results, it is expected that ALD deposited ZnO layer passivates surface defects on TiO_2 NWs surface; thus, reduces the amount of recombination of electron hole-pair (e-h) for duration of charge carrier transport to the electrodes [84]. To gain better insight about passivation ability of ZnO angstrom thick layer, PL measurement is carried out for TiO_2-ZnO core-sheath working electrode with an excitation wavelength 320 nm at room temperature. The PL results support the obtained XPS data shown in Figure 4.9 and demonstrates the near band emission (NBE) centered at 408 nm and a small peak attributed to shallow surface defect trap emission (STE) at 424 nm as confirmed the peak

positions in previous studies [85]. Here, NBE is stemming from e-h recombination across the conduction band (CB) and valence band of (VB) TiO_2. As known, these surface defects can pinpoint exactly oxygen vacancies and Ti interstitials. From O1 spectrum, a small peak has been clearly observed which verifies the presence of oxygen vacancies. This means is that V_O energy levels build a shallow donor state below the CB of TiO_2 [86]. Keep this in mind, the other possible surface defects can be bonded Ti interstitials which are totally related to oxygen vacancies. This is because, in an ionic scheme, it is likely that two excess electrons per V_O can be transformed to the nearest neighboring Ti atoms and cause redistribution of excess charges [87]. However, there was no trace ascribed to Ti interstitial in Ti2p spectra detected. Thus, the major surface traps of obtained samples are associated to V_O trap states. Looking back to the information obtained from PL measurement, just passivation with an ultrathin ZnO of NWs has intensified the NBE peak.

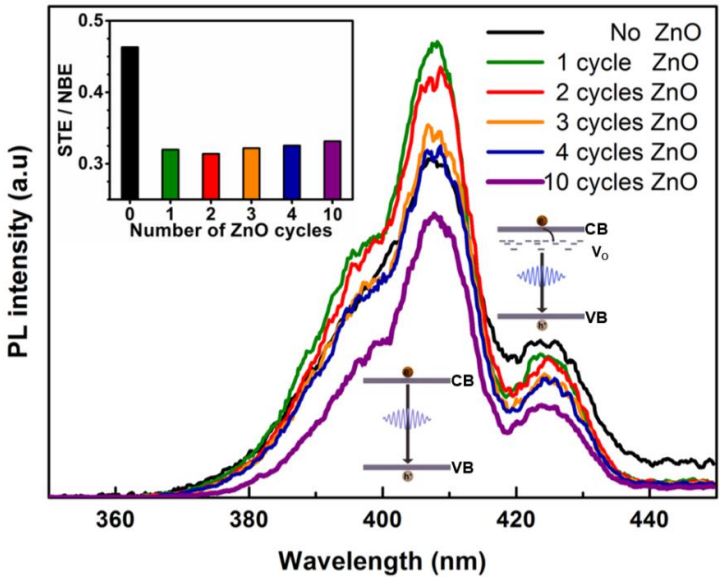

Figure 4.9: The PL spectra for different ZnO cycles coated TiO_2 NWs samples for an excitation wavelength of 320 nm. All samples show a near band-edge emission (NBE) at 408 nm arising from e-h recombination across the conduction band (CB) and valance band (VB) of TiO_2 and a shallow surface defect traps emission (STE) centered at 424 nm. The inset shows the ratio of STE / NBE.

From Figure 4.9, deposition of 1 cycle of interfacial ZnO layer has strengthened this peak along passivation of surface traps of TiO_2, but a further increase on shell thickness leads to a reduction of PL intensity. A possible explanation regarding this reduction for thicker ZnO shell layers is hidden in XPS results. Although deposition of first ALD cycles of ZnO passivates oxygen vacancy related surface defects, the amount of chemisorbed oxygen on the core-sheath surface follows an upward trend for subsequent cycles (Figure 4.5).

Based on the Madelung potential of the highly ionic crystal, these oxygen-containing molecules will act as a new trap states in the core–shell structure [73], [80]. Therefore, these chemisorbed oxygen radicals can provide an efficient charge separation that allows some of the photoexcited electrons to migrate to this localized trapping host. This separation is responsible for the reduction in NBE intensity because it reduces the probability of e–h recombination across the band gap. On the other hand, the STEs for all passivated samples exhibit a gradual quenching effect that is more pronounced for thicker shell layers. Considering that the origin of STE is generally attributed to the intrinsic V_O surface defects of TiO_2, these results strongly suggest that there is an association between the passivation of non-radiative recombination sites by ultrathin ZnO and the increment in NBE emission intensity that simultaneously quenches STE. To provide a qualitative comparison, the intensity ratio of STE/NBE is also calculated for all samples (the inset of Figure 4.9). From this data, it is apparent that the ratio decreases considerably for the sample coated with one cycle of ZnO and stays almost constant for thicker layers, which is in line with the XPS measurement results.

To gain better insight on the effect of ZnO layer on PV performance of the cell, transient photovoltage decay measurement has been performed. This is an analysis technique which can provide some information on the charge recombination rate at the TiO_2-electrolyte interface.

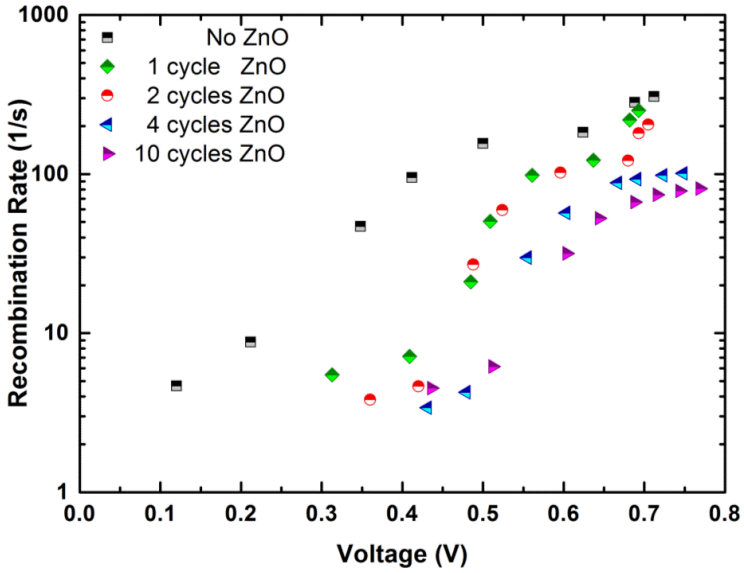

Figure 4.10: Electron recombination rates for different DSSC devices including bare TiO_2 NWs and TiO_2 NWs coated with different numbers of ALD ZnO cycles obtained from transient photovoltage decay measurements.

Figure 4.10 reveals the extracted values for recombination rates obtained from photovoltage decay measurement for various incoming light intensities. The recombination rates for all passivated samples are lower than that of the reference cell. Since the recombination rate is related to the retardation of electron back-transfer, the conduction band position of the shell layer should be several electron volts above (more negative potential) that of the TiO_2 core to effectively slow down the kinetics. However, the conduction band position of the ZnO layer is observed to be below that of the TiO_2 core. Hence, this retardation in electrons' back transfer rate should be attributed to a ZnO induced modification of the TiO_2 surface. According to previous studies, the oxygen-containing gas molecules tend to be chemisorbed on the host materials surface via capturing free electrons [72],[76],[77],[80]. As a result, these chemisorbed oxygen radicals will reduce free carriers density in the vicinity of the surface and deplete the surface electron states [81],[82]. This triggers the formation of the space charge region and the band bending near the NWs surface. Looking back to the XPS results, density of chemisorbed oxygen exhibits an increasing trend as the ZnO shell layer thickens. Thus, it is speculated that ZnO induced surface band bending (SBB) will be more pronounced for subsequent ALD cycles. It should be noted that back-reaction

of injected electrons occurs mainly via two routes: (1) the direct recombination among CB; or 2) exponentially distributed trap-mediated electrons with oxidized redox couples. Therefore, the ZnO shell layer will reduce both recombination rates (K^{CB}_{ET} and K^{trap}_{ET}) by inducing an effective SBB at the TiO_2 surface and reducing surface trap density at the interface, respectively. Keeping this in mind, the ZnO layers will reduce recombination rates just due to passivation of surface traps, and the addition of more layers will generate the SBB effect in addition to the passivation effect. Consequently, a more efficient reduction in the recombination rate of injected electrons will be provided.

In addition to suppressing recombination of photogenerated electrons across the interface, ZnO shell layer can enhance device performance by modifying NWs surface due to its high isoelectric point (IEP of ZnO is 9 compared to 5 for TiO_2 [44]). IEP defines the PH at which the oxide surface has a net zero charge [90]. ZnO layer, as an alkali material with a PH>7, will be positively charged, and hence it will become a more favorable host site for acidic carboxylic chains of N719 (PH<7). Therefore, the dye adsorption is expected to be increased by introduction of ZnO layer. To substantiate this claim, dye adsorption measurement is performed using Microplate Reader to investigate dye adsorption as a function of number of ALD cycles (see Figure 4.11). The amount of dye adsorbed on the photoanode is calculated after desorption of N719 dye from the surface using a 1:1 ethanol–0.1 M NaOH solution (Figure 4.12 and Figure 4.13)

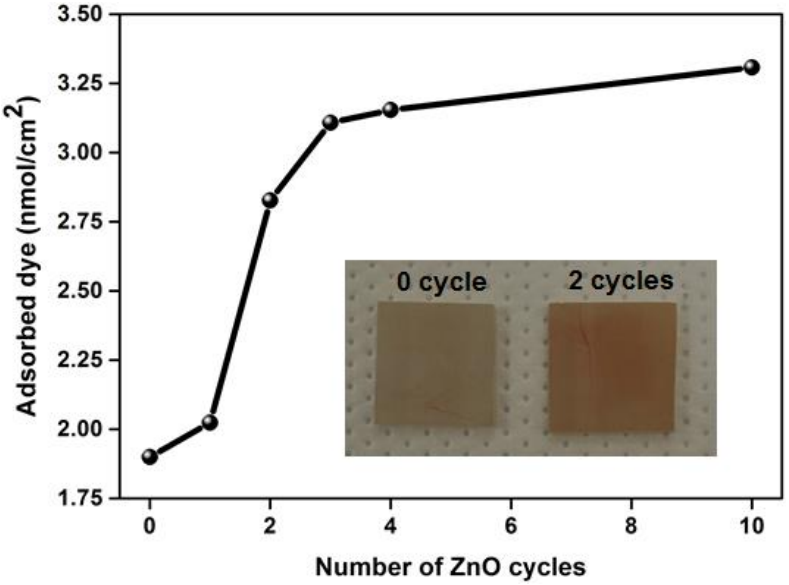

Figure 4.11: The amounts of dye adsorbed on the surface of TiO_2 NWs coated with different numbers of ALD ZnO cycles, showing a sharp increase for the sample coated with two cycles. For additional cycles, the adsorbed amount follows a gradual increase.

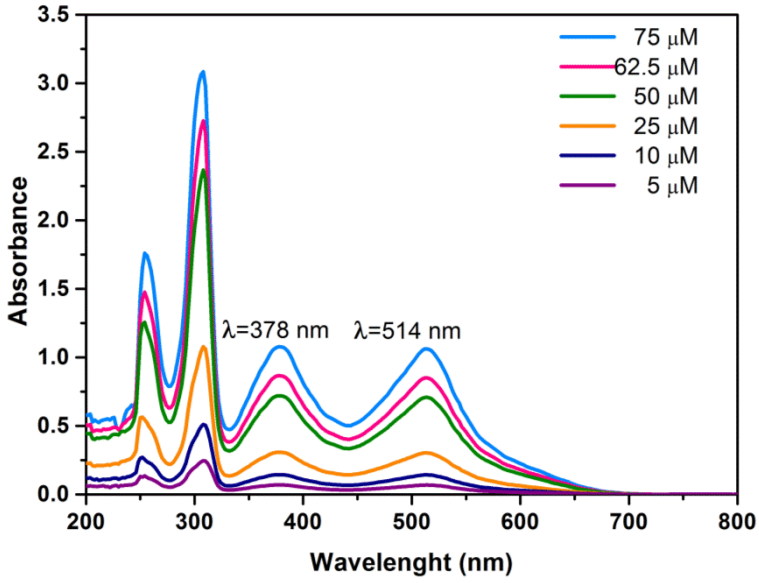

Figure 4.12: UV–Vis absorption spectrum of N719 sensitizer dye and max absorption is observed at 378 nm and 514 nm.

Although the first cycle of ZnO causes a small increase in dye uptake compared to the bare TiO_2, it is well known that the monolayer usually cannot reach 100% coverage. Figure 4.11 demonstrates that there is a significant enhancement in the amount of dye adsorbed at two cycles. After two cycles, the adsorption profile increases gradually, as expected.

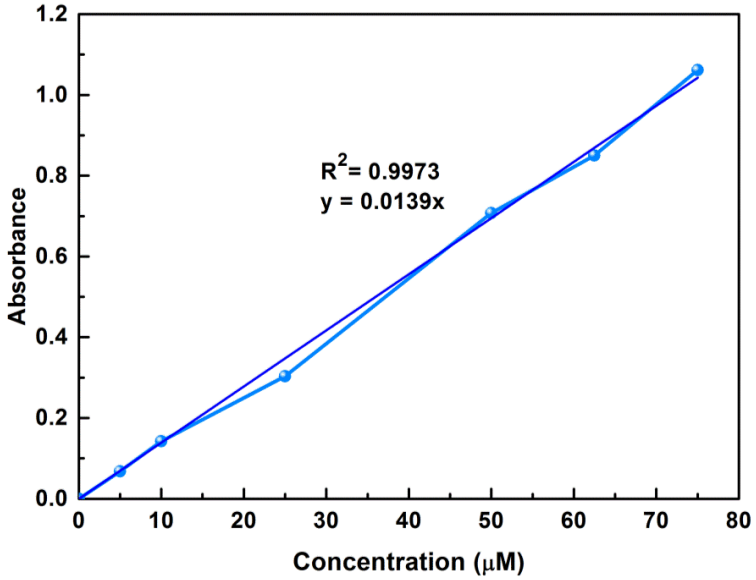

Figure 4.13: Concentration versus absorbance graph of N719 at 514 nm. The calibration curve of dye obtained from 5 different dye concentration (75, 62.5, 50, 25, 10, and 5 μM in 1 mL) and each sample immersed in 1mL of 1:1 ethanol–0.1 M NaOH solution for desorption of the dye.

As mentioned earlier, ZnO passivation layer increases power conversion efficiency up to a maximum at two cycles and it then falls back to extremely low efficiencies at 10 cycles. In order to elucidate the physical reasons responsible for this exponential drop in device performance, it is imperative to understand electron injection kinetics at the interface. In this way, understanding the band alignment at the heterostructure interface can provide better insight on the device performance. Although some papers report a band alignment where the position of conduction band of ZnO layer is at higher energy than that of TiO_2 [91]–[93], some report the opposite [94]–[96]. Considering this fact, we first adopted a high resolution XPS measurement to explore the band alignment of TiO_2-ZnO core-sheath structure. To understand electron flow process and charge transfer in the structure, valence and conduction band offsets ((ΔE_V) and (ΔE_C)) are determined respectively by well-established analysis technique of Kraut et. al [97]. In this approach, ΔE_{CL} is the energy difference between Zn2p and Ti2p core levels (CLs) in the TiO_2-ZnO (heterojunction) sample, as it is shown in Figure 4.17 and ΔE_{CL} found as 563.57 eV (also see Equation 1[98]). The energy difference of the CL to

valance band maximum (VBM) for rutile TiO_2 NWs, $(E_{CL} - E_{VBM})_{TiO_2}$ is and determined as 456.09 eV (Figure 4.15), while its value for ZnO, $(E_{CL} - E_{VBM})_{ZnO}$ is found to be 1018.96eV.

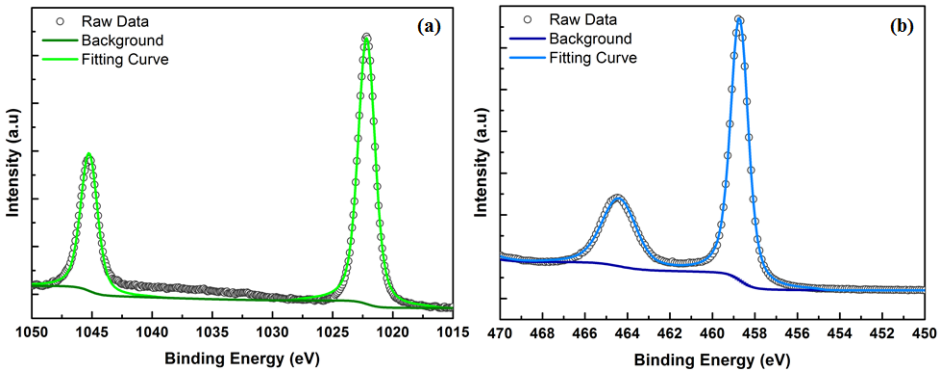

Figure 4.14: CLs of a) Zn 2p3/2 and b)Ti 2p3/2 recorded on TiO_2 –ZnO heterojunction. All peaks have been fitted to Voigt line shapes using a Shirley background, and the VB values are determined by linear extrapolation of the leading edge to the baseline.

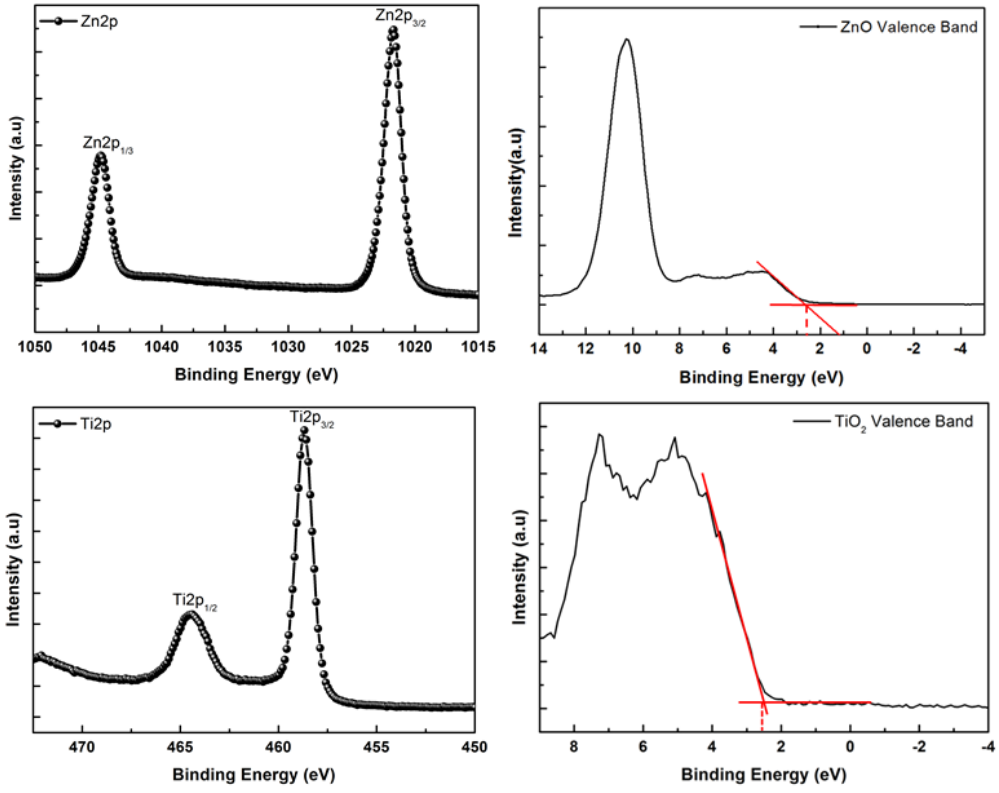

Figure 4.15: CLs and VB Spectra of Zn 2p3/2 and Ti 2p3/2 recorded on pure ZnO and TiO_2 samples (VBM values are determined by extrapolating of leading edge to the base line.)

It should be noted that the CL spectra of Zn 2p3/2 and Ti 2p3/2 show peaks located at 1021.58 eV and 458.68 eV, respectively. In this regard, the calculated values of E_{VBM} are 2.62 eV for rutile TiO_2 (which is in good agreement with [99]) and 2.59 eV for ZnO (Figure 4.15). All obtained data are summarized in Table 4.3. The optical band gap of the bare rutile TiO_2 NW arrays estimated from the graph of $(\alpha hv)^{1/2}$ versus hv is 3.02 eV [100] (Figure 4.16). The band gap of ZnO is taken as 3.37 eV at room temperature [101]. Finally, ΔE_V and ΔE_C are calculated from eqn (2) and (3) as 0.7 eV and 0.35 eV, respectively.

$$\Delta E_{CL} = \left(E_{Zn} - E_{TiO_2}\right)_{\text{TiO2/ZnO core/shell}} \quad (1)$$

$$\Delta E_V\left(\frac{\text{ZnO}}{\text{TiO}_2}\right) = (E_{CL} - E_{VBM})^{\text{bulk}}_{\text{TiO}_2} - (E_{CL} - E_{VBM})^{\text{bulk}}_{\text{ZnO}} + \Delta E_{CL} \quad (2)$$

$$\Delta E_C = \left(E_{g_{TiO2}} - E_{g_{ZnO}} + \Delta E_V\right)_{\text{TiO2/ZnO core/shell}} \quad (3)$$

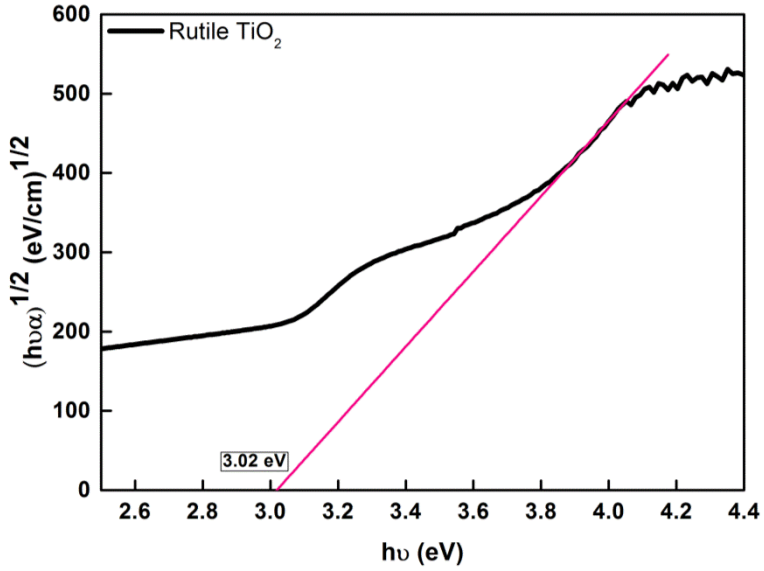

Figure 4.16: 7 $(\alpha h\nu)^{1/2}$ versus hν plot for the bare rutile TiO_2 structure

Based on these calculations, the predicted energy band diagram of the structure is shown in Figure 4.17, in which conduction band edge of rutile TiO_2 is 0.35 eV above that of ZnO. This band alignment would persuade ZnO

interfacial layer to act as a quantum well to capture photogenerated dye electrons [92].

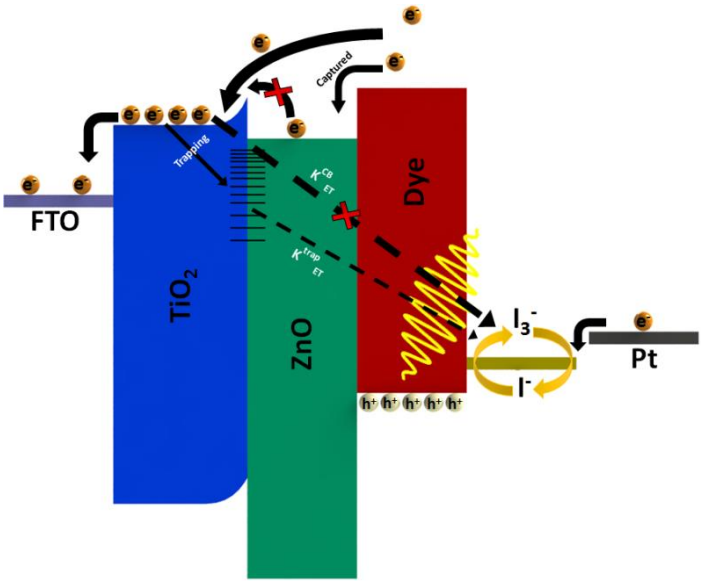

Figure 4.17: Energy band diagram of a DSSC showing band alignment in the TiO_2–ZnO interface. Some photoexcited electrons will be captured by the ZnO well, while the rest will be injected to the CB of TiO_2. The ZnO passivation layer will reduce recombination rates by reducing surface trap states at the interface and inducing surface band bending at the TiO_2 surface.

Table 4.3: Results obtained from XPS valence band spectra

Sample	Region	Binding Energy(eV)
TiO_2	Ti $2p^{3/2}$	458.68
	VBM	2.59
ZnO	Zn $2p^{3/2}$	1021.58
	VBM	2.62
TiO_2 /ZnO	Zn $2p^{3/2}$	1022.18
	Ti $2p^{3/2}$	458.61

Whether photogenerated dye electrons will be captured by the potential well or will escape from it depends on well-width and initial kinetic energy of electrons which is related to incident photon energy [102]. The probability that an electron will be captured increases as the thickness of the ZnO layer increases. Hence the amount of electrons captured in the well will be exponentially increased, and short circuit current will show a significant reduction. On the other hand, it is more likely that photogenerated electrons at lower photon energies will diffuse into the ZnO potential well towards the TiO_2 conduction band during thermalization.

Chapter 5 Omnidirectional Antireflective Coatings for Performance Enhanced DSSC

This part is based on the publication "Enhanced performance of dye-sensitized solar cells by omnidirectional antireflective coatings", **Turkan Gamze Ulusoy**, Bihter Daglar, Adem Yildirim, Amir Ghobadi, Mehmet Bayindir, and Ali K. Okyay, 2015, **5**, 053090 1-9. Reproduced (or "Reproduced in part") with permission from SPIE. Copyright 2015, Journal of Photonics for Energy. This study is collaborative work with the Prof. Mehmet Bayindir`s group in UNAM.

5.1 Introduction

In the last decade, dye sensitized solar cells (DSSCs) have undergone a renaissance as lightweight, low-cost and relatively high efficiency photovoltaic (PV) due to extensive improvements in materials, device design and fabrication technologies [103], [104]. Intense research efforts mainly focused on synthesizing new organic dye molecules with higher absorptivity and materials as more efficient carrier transport layers [105]–[109]. Single layer antireflection (SLAR) coating is a common approach to increase the light absorption in different types of solar cells [110]–[113]. The use of silica micro/nano spheres [114], bioinspired moth-eye shaped structures [115], and other designs are examples of these coatings [116], [117]. However, the SLAR coatings are optimized to decrease reflection losses in a relatively narrow spectral range and at incidence angles close to surface normal. On the other hand, solar radiation is inherently broadband and reaches the solar cell surface at a wide range of incidence angles. Therefore, broadband and omnidirectional AR coatings are required to provide significant enhancement in the device performance. Reflection from a surface can be significantly suppressed by gradually changing the refractive index between the two media [118]. Although double layer [119], [120], triple layer [121], multilayer coatings, and tapered structures [122] are proposed to achieve this gradual change, there are

only limited reports [110]–[113] that focus on the fabrication of graded index coatings on the surface of glass anode due to challenges such as high cost and suitability to large-area fabrication of such complex structures and their integration with DSSCs. The other challenge in preparing such multifunctional surfaces is to provide a trade-off between the high surface roughness requirement of superhydrophobic coatings and the low surface roughness requirement for antireflection capability [123]. Therefore, to prepare antireflective and superhydrophobic surfaces, the roughness factor should be optimized; it must be small enough to avoid diffuse reflection from the surface and high enough to provide superhydrophobicity. Recently, we reported the facile fabrication of large-area organically modified silica (ORMOSIL) coatings with well-tuned porosity (therefore refractive index) and surface morphology [124],[125]. Due to their inherent porosity and hydrophobicity, these coatings demonstrate antireflective and/or superhydrophobic properties depending on their synthesis conditions. It is also possible to create multilayer ORMOSIL structures to realize omnidirectional and broadband AR coatings [124].

In this thesis, we demonstrate the integration of multilayer antireflective (MLAR) ORMOSIL coatings on the photoanode of a DSSC device. It is shown that MLAR ORMOSIL coatings can reduce light reflection losses in a broad range of wavelengths and angles of incidence that significantly improve the efficiency of DSSCs. For the proof-of-concept demonstration, we examine the applicability of this AR coating layer using commercial titania paste as photoanode. It should be noted that the substantial improvement in the cell efficiency can be attained through modification of each layer (such as using more absorptive dyes or highly collective photoanodes) or engineering of their interfaces to reduce carrier recombination, which is out of the scope of this paper. The results obtained here are of significant interest for commercialization issues, where self-cleaning and omnidirectionality of the layer guaranties the durability of the cell under harsh conditions and maximizes the solar exposure of the modules without using tilt and/or tracking systems.

5.2 Materials and Reagents

Tetraetyl orthosilicate (TEOS), tetramethyl orthosilicate (TMOS), methyltrimethoxysilane (MTMS), oxalic acid, and ammonium hydroxide (25%) were purchased from Merck (Germany), ethanol and hydrochloric acid (37%) (HCl) were purchased from Sigma-Aldrich (U.S.A.), and methanol was purchased from Carlo-Erba (Italy). All chemicals were used as received.

5.3 Preparation of Nanoporous ORMOSIL Coatings

To prepare ORMOSIL coatings first ormosil gels are synthesized.[23] ORMOSIL coatings were synthesized using methyltrimethoxysilane (MTMS) and tetramethyl orthosilicate (TMOS) monomers with the complete hydrolysis and condensation, respectively. For first step, x mL (x is between 0.4 and 1) of MTMS and $1 - x$ mL of TMOS are added to 9.74 mL of methanol. Afterward, 0.5 mL of 0.01 M aqueous oxalic acid solution was added to the solution dropwise under gentle stirring. The reaction mixture was further stirred for 30 min and left for complete hydrolysis for 24 hours at room conditions. Condensation was started by dropwise addition of 0.42 mL of ammonium hydroxide (25%) and 0.19 mL of water mixture under gentle stirring, and the reaction mixture was further stirred for 15 min. Finally, the solution was poured into a polystyrene vial and left for gelation at 25 °C. Gels were formed typically within one day, and they were aged for two days to strengthen the porous structure. After aging, 12 mL of methanol was added to the gels, and the resulting mixture was sonicated for 45 s at 20 W using an ultrasonic liquid homogenizer in order to obtain ORMOSIL colloids. The colloids were spin coated on clean glass surfaces at 2000 rpm and dried at room temperature overnight. To increase the hydrophobicity and integrity of the coatings, they were heated to 450 °C for 1 h. The colloids and corresponding coatings were named with the number in the abbreviation indicating the TMOS volume fraction in the corresponding colloid, such that TM 7.5 indicates the coating produced using the colloid containing 7.5% TMOS and 92.5% MTMS.

5.4 Preparation of Nonporous ORMOSIL Coatings

Third and last member of MLAR is nonporous film (NPF), which was prepared by tetraethyl orthosilicate (TEOS) and MTMS monomers according to standard procedure [125], where 4.5 mL of MTMS (for NPF 1) or 3 mL of MTMS and 1.5 mL of TEOS (for NPF 2) are dissolved in 4.5 mL of ethanol and 0.4 mL of water, and 10 μL of 0.1 M HCl are added. The mixture is stirred (at 250 rpm) at 60 °C for 90 min. Then, 0.8 mL of 0.1 M HCl and 0.7 mL of water are added, and further stirred for 15 min at room temperature. Then, the solution is stayed at 50 °C for 15 min and diluted with an appropriate amount of ethanol. For example, to prepare 80 nm thick films, we added 14 mL of ethanol to the 2 mL of aged solution. Finally, 200 μL portions of diluted sol are coated on clean glass surfaces with spin coating at 2000 rpm.

5.5 Preparation of Three-Layer Coating

We prepared three layer coating by successive spin coating of ormosil solutions at 2000 rpm. First, the nonporous ormosil layer (NPF 2) was spin coated as described above and dried at room temperature overnight. To the top of this layer, 140 nm TM 60 was coated. To give the desired thickness, 4 mL of TM 60 colloid was diluted using 3 mL of methanol. This layer was dried at 225 °C for 1 h. Then, ~240 nm TM 7.5 layer is coated to the top of the TM 60 layer. To give the desired thickness 2 mL of TM 7.5 colloid was diluted using 1 mL of methanol. Finally, coating was cured at 450 °C for 1 h to guarantee strong adhesion between the layer and glass substrate. Also, it should be noted that spin coating of the AR solution was carried out using a low-profile chuck with fragment adapter (laurell 5-25 mm Adapter P/N 1002 0748 in NPP) and this mm-scale vacuum hole is adjusted to a place, far from the TiO_2 paste. So no damage is expected to the TiO_2 paste during the spin coating.

5.6 DSSC Assembling

Nanoporous TiO_2 coated test cells were purchased from Solaronix (~8-10 µm, opaque) as a working electrode. Three-layer ORMOSIL colloids were then coated one by one on glass surfaces using spin coating method and the photoanode was annealed at 450°C for 1 hour to get titania anatase crystalline structure. After isolation of the ORMOSIL coated side, TiO_2 photoanodes were soaked in 0.5 mmol Ruthenium sensitizer [cis-di(thiocyanato)-N-N′-bis(2,2′-bipyridyl- 4-carboxylic acid-4′-tetrabutylammonium carboxylate) ruthenium (II)] dye (known as N719, Solaronix) in a t-butanol/acetonitrile (1:1, in volume ratio) solution, for 24 hours at room temperature. The samples were rinsed with acetonitrile to remove non-chemisorbed dye molecules. The drilled platinum-coated conducting glass was used as counter electrodes bonded to photoanode by 25-µm-thick thermal sealant (Dupont). The active area of each cell was filled with ~10 µL electrolyte (Iodalyte HI, Solaronix) driven by capillary force through the hole. The area of the electrode was controlled using a mask of 0.36 cm^2 area on the hot-melt sealed film. The projected area for the tilted angles are also taken to be 0.347 cm^2 and 0.312 cm^2 for 15° and 30° incidence angles, respectively.

5.7 Results and Discussions

Superhydrophobic ORMOSIL aerogel thin films are reported as an effective route for large area superhydrophobic AR layers. To the best of our knowledge, no integration of these coatings with a solar cell structure is studied before. In this report, photoanode is functionalized with three-layer AR coating and the effect of this coating on PV performance has been investigated. It is shown that this layer can reduce the light loss significantly, hence enhances the efficiency of the solar cell.

Figure 5.1(a) illustrates a 3D schematic of the fabricated photoanodes of dye sensitized solar cell that is functionalized by MLAR ORMOSIL coating. The proposed device consists of 5 main parts; 1) broadband and omnidirectional

MLAR ORMOSIL coating for matching the refractive indices of air (n=1) and glass (n=1.5), 2) nanoporous titania paste on transparent conducting oxide (TCO) as photoanode, 3) cis-bis (isothiocyanato) bis (2,2′-bipyridyl-4,4′-dicarboxylato) ruthenium (II) (N719) as photosensitizer, 4) the iodide/tri-iodide (I^-/I_3^-) shuttle as electron transfer mediator and finally 5) Pt-coated conducting glass as counter electrode.

Figure 5.1(b) shows the working principle of AR coated photoanode. Previously, we determined that the optimum refractive indices of bottom layer (NPF), middle layer (TM60), and top layer (TM7.5) were as ~1.4, ~1.2, and ~1.1, respectively, and corresponding thicknesses were determined as 80 nm, 140 nm and 240 nm, respectively [124]. The gradual matching of the refractive index of air (n=1) to the glass, minimize the reflection of the light from the surfaces and accordingly increase the light absorption of the cell. SEM images of three-layer ORMOSIL coating on a TCO substrate is shown in Figure 5.1(c, d). Nanoporous structure of the MLAR also utilizes the self-cleaning property with a contact angle of ~156° (Figure 5.1(c) inset) owing to its superhydrohobicity. This finding is promising for the outdoor application of such DSSCs to prevent dirt accumulation on the devices.

In order to investigate the impact of multifunctional ORMOSIL coating and its omnidirectional property on the photovoltaic (PV) performance of the DSSCs, current-voltage curves were collected at different angles of light incidence (0°, 15°, 30°). The DSSC without AR coating is prepared by removing the coating to use identical solar cells as its own reference cell in both measurements. Due to the its hybrid nature, this ORMOSIL coating is deformable, mechanically and thermally stable and makes strong adhesion to the plastic and glass substrates [125],[126]. Also further improvement in the adhesion between glass and the coating is attained through annealing at 450 ˚C for 1h.

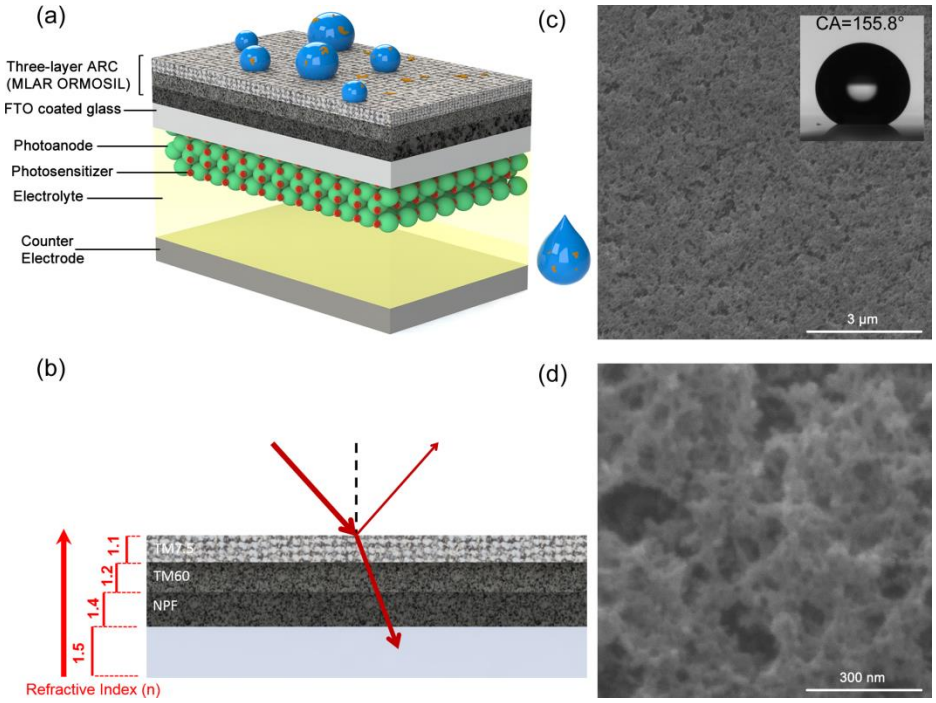

Figure 5.1: (a) Schematic of the DSSC design consists of MLAR ORMOSIL coating (three-layer anti-reflective (AR) coating) single side coated TCO glass substrate, titania paste as photoanode, dye as photosensitizer, electrolyte as electron transfer mediator, Pt-coated conducting glass as counter electrode. This AR coating which is a superhydrophobic porous film can provide self-cleaning property of the cell, blue spheres and brown particles on the surface represent the water droplets and dirt molecules, respectively. (b) The schematic illustration of AR coating with three-layer and its effect on light reflection reduction through gradual increasing of the refractive indices as 1.1, 1.2, 1.4, respectively to match it to the bare glass refractive index (1.5). (c) Top view SEM images of three-layer porous thin film. The inset shows the water contact angle of the surface which is 156° indicating superhydrophobic property of the porous film. (d) Higher magnification SEM image of the surface.

Therefore, to remove this coating from the surface, first, we gently scrap it off using razor blade for a couple of times. After partial removal of the coating, the residues are taken away from the surface using acetone and cleanroom swabs. Also, the quality of the surface is compared with a bare glass, using UV-Vis spectroscopy, demonstrating almost same transmittance for both samples (Figure 5.2). Figure 5.2(b-d) compares the solar cell current density-voltage (J_{SC}-V) characteristics in the absence and presence of AR coating. All related parameters including the short-circuit current density (J_{SC}), fill factor

(FF), and overall conversion efficiency ($\boldsymbol{\eta}$) are summarized in Table 5.1. These results prove that by applying this multifunctional coating on DSSCs, an obvious increment in short-circuit current density (J_{SC}) and efficiency ($\boldsymbol{\eta}$) is attained for all different angles of incidence.

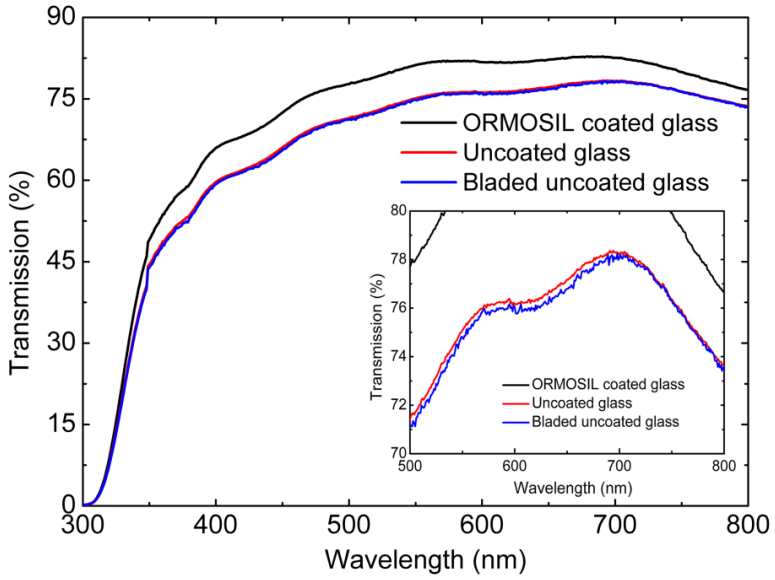

Figure 5.2: Transmission spectra of uncoated glass, ORMOSIL coated glass and glass after bladed of AR coating

For normally incident incoming light (θ=0°), device achieves a J_{SC} improvement of ~23% which results in an efficiency rise of ~25.9%. This ratio shows an upward trend and more salient for larger angles of incidence which is triggered by absorption of more photons due to lower surface reflection and reaches 32.1% ($\Delta\boldsymbol{\eta}$=31.1%) and 84.6% ($\Delta\boldsymbol{\eta}$=94%) for 15° and 30°, respectively.

Enhanced J_{SC} values as well as IPCE efficiency of the MLAR ORMOSIL coated DSSCs are closely related to the improvement of its transmittance and light absorption characteristics of the photoanodes with MLAR ORMOSIL coatings. Improvement in J_{SC} can be explained using the nonlinear relation between the number of generated carriers due to the photon absorption and J_{SC} in DSSCs [127]. The transmission spectra of both AR coated and uncoated FTO coated glass samples have been illustrated in Figure 5.3(a). As can be seen, ORMOSIL film has increased the amount of transmitted light

from air to glass interface. When this coating is applied to our device an average increase of 6.5% in generated electrons made an enhancement in J_{SC} as much as 23%. In previous reports [127], it was shown that the relation between number of generated carriers (Q) and J_{SC} has a nonlinear form in which J_{SC} is proportional to Q^{α}, where α (> 1) is a coefficient depended on the material and device properties of the DSSC. Therefore, the slight increase in the amount of transmittance could lead to a considerable change in the J_{SC}.

Moreover, in our previous study, it has been shown that AR layer reduces the light reflected off of the surface, which is lower than 2% on average (in the desired frequency range of 400-700 nm) over all incoming incident angles. Reflection loss increases considerably moving to more oblique angles, which mean that the suppression of light reflection is more dominant for higher angles of incidence. Keeping this in mind, it is expected that the J_{SC} enhancement of the DSSC is more significant for oblique angles, while open-circuit voltage, V_{OC}, does not change with the use of three-layer coating. Considering the fact that V_{OC} is mainly related to the retardation of the electron's back reaction at the semiconductor/electrolyte interface and our modification is not related this interface. It is expected that V_{OC} is almost constant (between 0.57 and 0.59) for all measurements.

Table 5.1: Photovoltaic parameters for the ORMOSIL coated photoanode in DSSC with different incident angles under AM 1.5 G filtered spectral illumination at an incident intensity of 100 mW/cm^2.

Device	Angle θ	V_{OC} (V)	J_{SC} (mA/cm^2)	FF	η (%)
ORMOSIL coated	0	0.59	4.66	0.67	1.85
uncoated	0	0.59	3.79	0.66	1.47
ORMOSIL coated	15	0.59	4.13	0.67	1.62
uncoated	15	0.59	3.16	0.66	1.23
ORMOSIL coated	30	0.57	2.77	0.70	1.12
uncoated	30	0.57	1.50	0.67	0.57

Note: Reference cell (uncoated cell) = DSSC removed the coating using a razor blade for each cell. Values given are mean values of three cells prepared in a similar way. Experimental errors of the mean values are within $\pm$2 mV for V_{oc}, $\pm$0.20 mA/ cm^2 for J_{sc} and $\pm$0.5 % for FF.

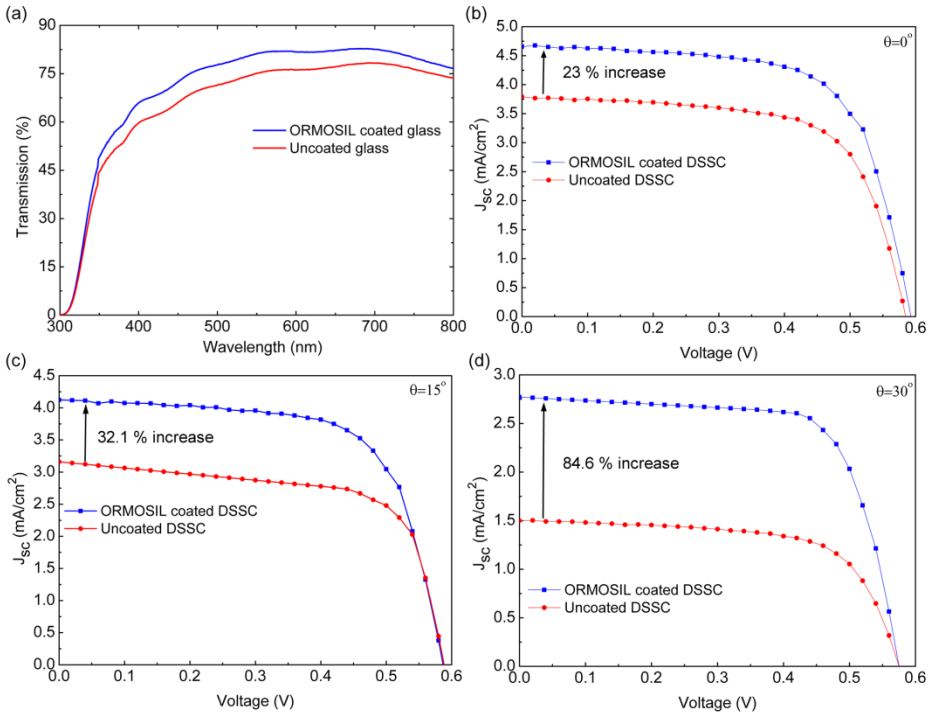

Figure 5.3: (a) Variations of UV-Vis optical transmittance spectra for the ORMOSIL coated (blue) and uncoated (red) samples. For the whole range, 300nm-800nm, the amount of transmittance has increased and an average increase of 6.5% is recorded for visible spectrum. (b, c, d) One-to-one comparison of J_{SC}-V characteristics of the ORMOSIL coated cells under different incident angles of incoming wave (0°, 15°, 30°). The ORMOSIL coating has been removed by razor blade and acetone and used as the uncoated sample. It is shown that the amount of J_{SC} has increased by 23%, 32.1% and 84.6 % for different incident angles of 0°, 15°and 30°, respectively.

In addition to earlier explanations, the substantial increase in J_{SC} can be understood by the spectral incident photon-to-current conversion efficiency (IPCE) measurement shown in Figure 5.4. As expected, the ORMOSIL functionalized DSSC has sufficiently higher IPCE values compared to the reference device which is in accordance with our earlier results.

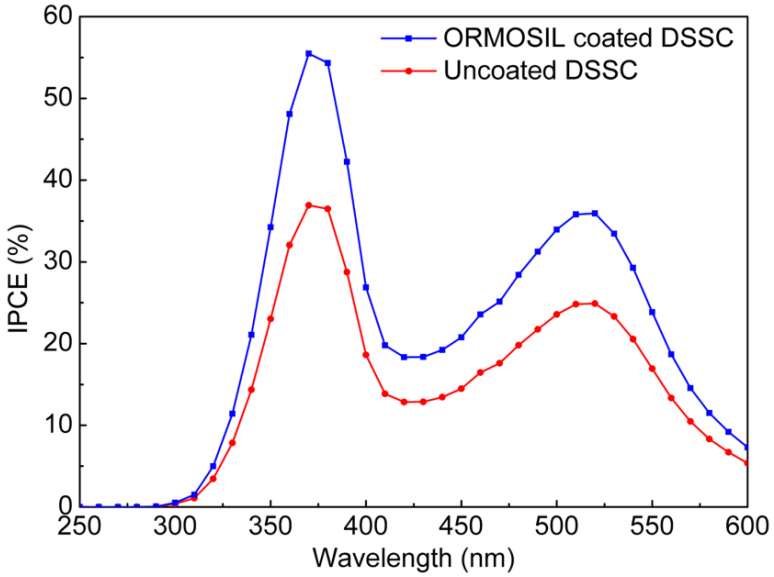

Figure 5.4: IPCE curves are collected in a wavelength range of 250nm-600nm for the both ORMOSIL coated and uncoated cells. The amplitude of maximums located at 370nm and 520nm are improved by about 19% and 11%, respectively. The three-layer coating significantly improves IPCE efficiency for the solar cell.

Chapter 6 Peptide Nanofiber Network Templated ALD-grown TiO_2 Nanostructures for DSSC

This study is collaborative work with the Assist. Prof Dr. Necmi Biyikli and Assoc. Prof. Dr. Mustafa O. Guler groups` in UNAM.

6.1 Introduction

In the last decade, Dye Sensitized solar cells (DSSCs) have undergone a renaissance as lightweight, low-cost and relatively high efficiency renewable power sources due to extensive improvements in materials design and device fabrication technologies.

Transition-metal compounds are one of the most extensively studied materials to exploit their unique properties in catalytic, electronic, optical, energy conversion, and biomedical applications. Substantial effort has been devoted to the finding of convenient and universal techniques to fabricate industrially-significant compounds of transition metals at the nanometer scale. Intentions behind the interest of crafting materials at small dimensions have been to increase the specific active surface area and to reduce the diffusion path length for the reacting species. These two parameters are of utmost significance to boost the reaction rate taking place on nanostructures. TiO_2 and ZnO are among the most studied transition-metal oxides due to their particular electronic properties. Being wide-bandgap semiconductors, both of them can be excited by ultraviolet light (UV) illumination. Due to their unique electronic band structure, excited TiO_2 and ZnO can oxidize and electrolyze water, thereby holding a great promise for a variety of photocatalytic applications, such as artificial photosynthesis, photo-decomposition of hazardous materials, and hydrogen gas production. In accordance with the miniaturization concept, a variety of nanoscale TiO_2 and ZnO materials with unique architectures have been proposed at different length scales, such as nanospheres, nanowires, nanotubes, and three dimensional mesoporous structures so far.

Another device application of the nano-structured materials will be dye sensitized solar cells (DSSC). Owing to low cost active materials and synthesis, DSSCs are very attractive compared to silicon and thin film based photovoltaic (PV) technologies. Furthermore, the investment for production scale industrial facility is remarkably lower for DSSC than that for other PV technologies. In the literature and commercially available DSSCs, nanostructured TiO_2 and ZnO are used for high cell efficiency. In order to increase surface area and improve the electron transport properties, specially designed nanostructures are used. The self-assembled peptide amphiphiles (PA) nanofiber networks proposed in this project, can achieve a highly porous nanostructure network. Combined with the ALD technique, large surface area TiO_2 and ZnO nano-structured networks can be developed, which is innovative in the literature. DSSC devices fabricated using such a technique is also going to offer a novel contribution to the literature, significantly increasing the dye-semiconductor interaction surface area.

6.2 Materials and Reagents

Fmoc- and Boc- protected amino acids, Rink Amide MBHA resin, and HBTU were purchased from NovaBiochem and ABCR. The other chemicals were purchased from Fisher, Merck, Alfa Aesar or Aldrich and used as received. The 2.2 mm thick fluorine doped tin oxide (FTO) coated glass (sheet resistivity of 7Ω/sq), Ruthenizer 535-bis TBA (N719) photosensitizer dye, Iodolyte AN 50 electrolyte and Meltonix 1170-60 thermoplastic were all purchased from Solaronix.

6.3 Synthesis of Peptide for 3D TiO_2 Nanonetworks

In this study, PA molecule with a sequence of Lauryl-Val-Val-Ala-Gly-Lys-Am was designed and synthesized. Prepared peptide molecules are self-assembled into nanofibers and serve as a template with their functional amine groups exposed on the surface. The peptide was synthesized by solid phase peptide synthesis method. Peptide sequence was constructed on Rink Amide

MBHA resin (0.59 mmole/g). 0.5 mmole peptide synthesis was carried out; 2 equivalents (with respect to resin) of amino acids and lauric acid were used in each coupling. Amino acids or lauric acid (2 eq.) were activated with DIPEA (3 eq.) and HBTU (1.98 eq) prior to coupling. All couplings were carried out in dimethylformamide (DMF). At the end of the coupling cycles resin was cleaved from the resin by concentrated trifluoroacetic acid (TFA). For this purpose, a 10 mL cleavage cocktail (TFA:TIS:H_2O = 9.5:0.25:0.25) was prepared; distilled water (H_2O) and triisopropylsilane (TIS) were used as scavengers. Cleaved peptide was collected by dichloromethane (DCM), which was later removed alongside with TFA by rotary evaporation. Residual material was triturated by cold diethyl ether. White peptide precipitate was completely separated from ether by centrifugation; the centrifuge was dissolved in water, deep freezed at -80 °C and finally lyophilized.

6.4 Photoanode Fabrication

First, fluorine doped tin oxide (FTO) glass (1.67cm x 1.67cm) was treated with 100 mL of H_2O:NH_4OH:H_2O (5:1:1) solution at 75°C for 30 minutes. Then, 4 µL of 2% (wt/v) peptide amphiphile solution was spread directly on FTO with restricted area of 0.09π cm^2 (~0.28 cm^2), afterwards peptide solution was gelled by NH_3 vapor in closed container. Obtained hydrogel was converted to alcogel by series of alcohol in water mixtures (15%, 30%, 45%, 60%, 75%, 90% and 100%). Obtained alcogel was converted to aerogel by critical point drying. Next, ALD technique was employed on aerogel to coat TiO_2 in ALD reactor. The substrate temperature was kept at 150 °C during the ALD process using $Ti(NMe_2)_4$, and H_2O as titanium and oxygen precursors, respectively. Prior to deposition, $Ti(NMe_2)_4$ precursor was preheated to 75 °C. The pulse and purge times for $Ti(NMe_2)_4$ and H_2O are 0.1 s and 0.015 s, respectively. As the carrier gas, N_2 was employed with a flow rate of 20sccm. The deposition was carried out using successive 3 different deposition cycles including 100, 150 and 200 of TiO_2 with the estimated growth rate ~0.56 Å per cycle onto the peptide nanofibers. This yields about 5 nm, 7.5 nm and 10 nm thick uniform TiO_2 coating onto the peptide nanofibers. Coated samples

were calcinated in accordance with the following procedure: ramp from 25°C to 150°C with 5°C/min, 150°C to 350°C with 1°C/min, from 350°C to 450°C with 1°C/min and wait for 30 min (see Figure 6.1).

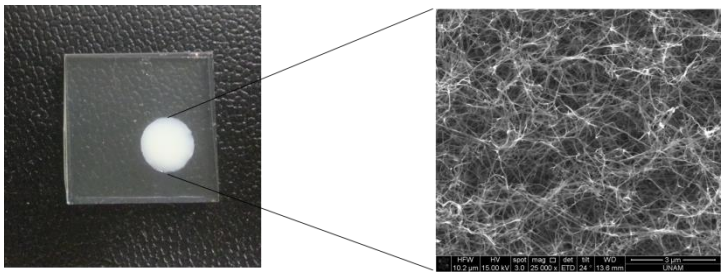

Figure 6.1: Representative image to nanostructured TiO_2 network

6.5 DSSC Assembling

The calcinated 3D TiO_2 nanonetworks used as a photoanode soaked in 0.3 mM ruthenium [cis-di(thiocyanato)-N-N_-bis(2,2-bipyridyl-4-carboxylic acid-4-tetrabutylammoniumcarboxylate) ruthenium (II)] dye (N719) absolute ethanol solution for 48 hours at room temperature to adsorb the dye adequately. The samples are rinsed with ethanol to remove non-chemisorbed dye molecules and dried in room temperature. As a counter electrode, 25 nm thick layer of Pt is deposited on glass by using Precision Etching Coating System (PECS). Afterwards, the photoelectrodes were sandwiched together using thermal sealant. The active area of each cell is filled with electrolyte driven by capillary force. The area of the electrode was controlled using a mask of 0.09π cm^2 (~0.28 cm^2) area on the hot-melt sealed film.

6.6 Results and Discussion

In this study, self-assembled peptide amphiphile nanofiber networks were exploited as an organic template for growth of interconnected TiO_2 nanowires. ALD technique was utilized in growth of nanostructured TiO_2 layers as anodic material in DSSC.

Here, the proposed device consists of 5 main parts; 1) templated TiO_2 nanonetworks as photoanode 2) cis-bis (isothiocyanato) bis (2,2′-bipyridyl-

4,4′-dicarboxylato) ruthenium (II) (N719) as photosensitizer, 3) the iodide/tri-iodide (I^-/I^{3-}) shuttle as electron transfer mediator and finally 5) Pt-coated conducting glass as counter electrode.

Figure 6.2 shows SEM images of the high surface area 3D TiO_2 nanonetworks indicating their morphology. As it can be clearly seen, before and after calcination, the morphology of the 3D TiO_2 nanonetworks prepared on FTO are kept unaltered. However, the calcined ones represent a hollow shape structures in which the surface is covered by a thin TiO_2 shell. This is an evidence for the successful formation of the TiO_2 nanotubes upon burning of the peptide scaffold template. To ensure the existence and thickness of TiO_2 shell layer, TEM experiment has been conducted for all samples (see Figure 6.3). The same observation (as SEM) was recorded for this measurement in which TiO_2 thin layer stayed on the peptide and it thickens moving to higher number of cycles. Also, it can be easily seen that this layer is quite conformal and uniform along the nanonetwork.

To identify the crystallinity phase of the TiO_2 coated 3D nanonetwork samples, Raman Spectroscopy is performed by using Raman Microscope. Based on these patterns shown on Figure 6.4, the prepared peptide coated TiO_2 nanonetwork samples on Si substrates exhibit prominent peaks at 153, 201, 396, 516, 636 cm^{-1} which are indicative of the formation of anatase phases, respectively.

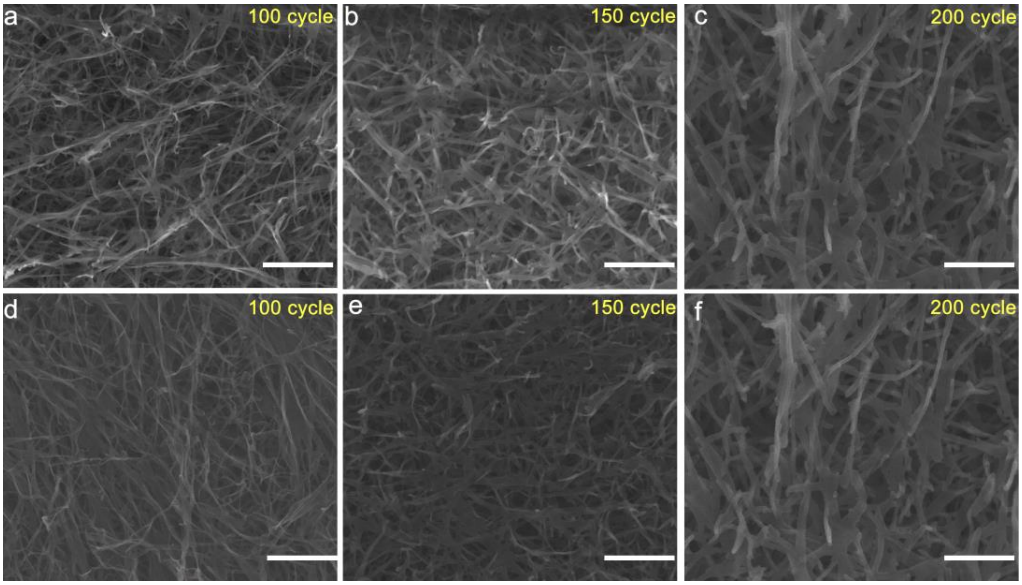

Figure 6.2: SEM images of 3D TiO_2 nanonetworks a-c) before and d-f) after calcination (bar scale: 1 µm)

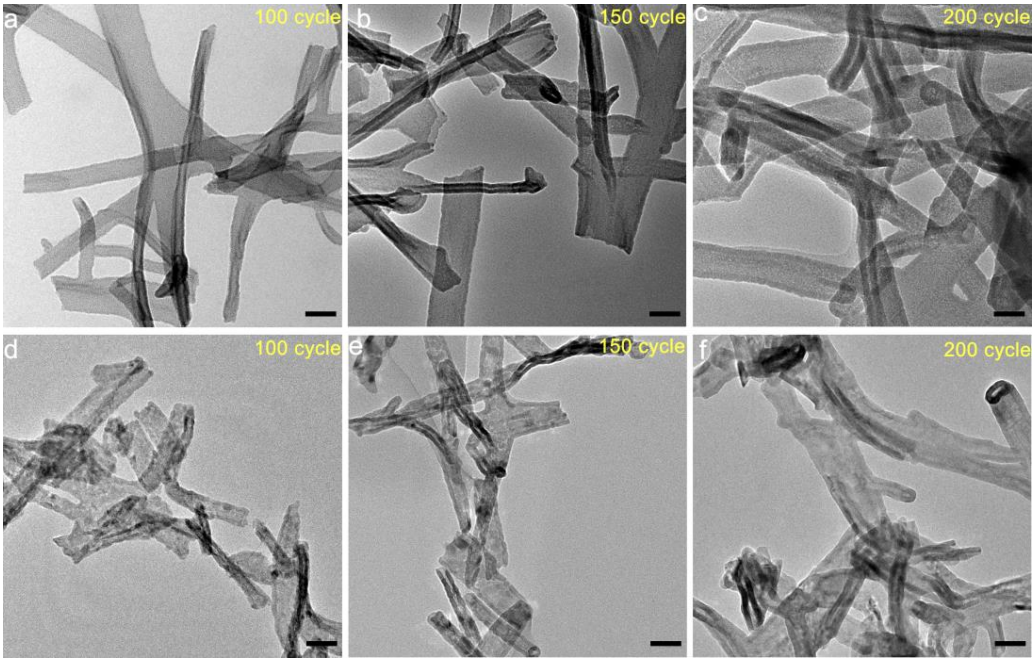

Figure 6.3: TEM images of 3D TiO_2 nanonetworks a-c) before and d-f) after calcination. (bar scale: 50 nm)

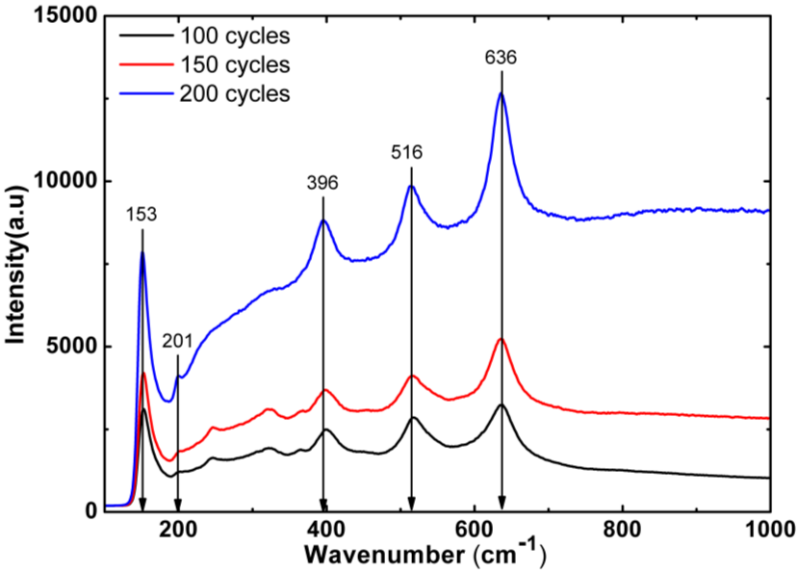

Figure 6.4: Raman of 3D TiO_2 nanonetworks for different ALD cycles

To explore the impact of number of TiO_2 ALD cycles on the optical properties of the nanonetwork structure, diffuse reflectance UV-VIS spectroscopy is employed for all the calcined cases. Using transmission data obtained from UV-Vis spectrometer the optical band gap of the all samples have been experimentally determined via extrapolating of the linear portion of Kubelka-Munk function, $(\alpha h\vartheta^2)$ versus photon energy, $h\vartheta$, as shown in Figure 6.5, where α is absorption coefficient. As it can be identified thicker TiO_2 coating samples show slight red-shift where the corresponding band gaps of 3.39, 3.33 and 3.24 eV are assigned for 100, 150 and 200 cycles, respectively. The high band gap of the thin layers is due to the 1D quantum confinement phenomena which are dominant in thin thicknesses. However moving toward to the thicker layers, the observed red-shift in the band gap is attributed to the influence of the *Urbach* band tails arising from the amorphous effect.

Figure 6.6a shows the current density-voltage (J_{sc}-V) characteristics for DSSC devices constructed with a TiO_2 template and template-free (8nm TiO_2 layer coated by ALD on FTO) photoanodes including 100, 150 and 200 ALD cycles are shown in Figure 6.6a. All related parameters including the short-circuit current density (J_{sc}), the fill factor (FF), and overall conversion efficiency ($\boldsymbol{\eta}$) are summarized in Table 6.1.

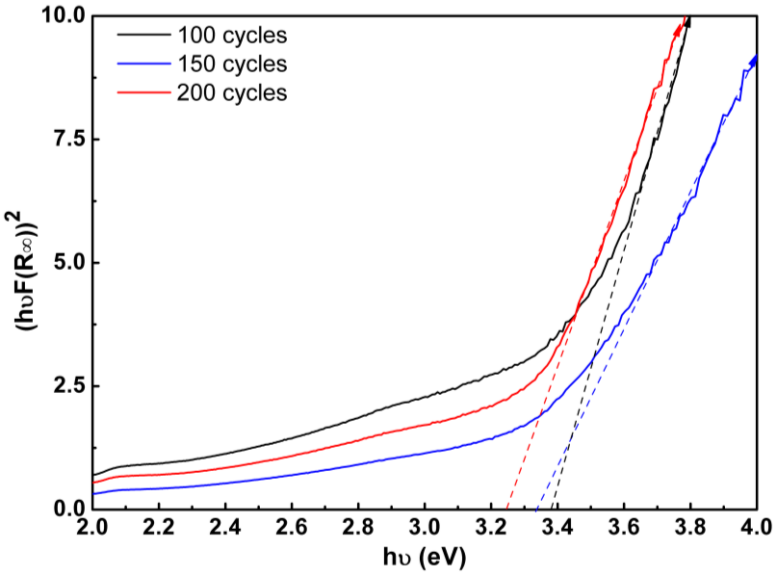

Figure 6.5: $(\alpha h\vartheta^2)$ versus $h\vartheta$ plot for TiO_2 templated structures with different ALD cycles and corresponding band gaps of 3.39, 3.33, 3.24, respectively.

As it can be clearly seen from Table 2 and Figure 3, there is a considerable discrepancy between reference sample and peptide templated DSSCs which is obviously due to the difference in the surface areas. There is a clear trend on the J_{SC} and V_{OC} while V_{OC} drops monolithically (from 0.77-0.71 V) moving to thicker coated samples, J_{SC} shows a maximum amount of 681 μA/cm^2 for 150 cycles and again drops to 572 μA/cm^2 for 200 cycle one. The same trend is followed by efficiency in which the nominal amount of 0.47, for 100 cycles coated sample, jumps to a maximum of 0.97 for 150 cycles and declines gradually to 0.92 for next additional 50 cycles. It should be noted that these are all much higher compared to the photovoltaic results of peptide free-templated DSSCs in which a low efficiency of 0.001 is attained. This is mainly because of the fact that obtained TiO_2 networks have extremely higher surface areas (compared to planar design), so dye adsorption bounces significantly on the template architecture which this in turn significantly enhances photovoltaic performance of the cell.

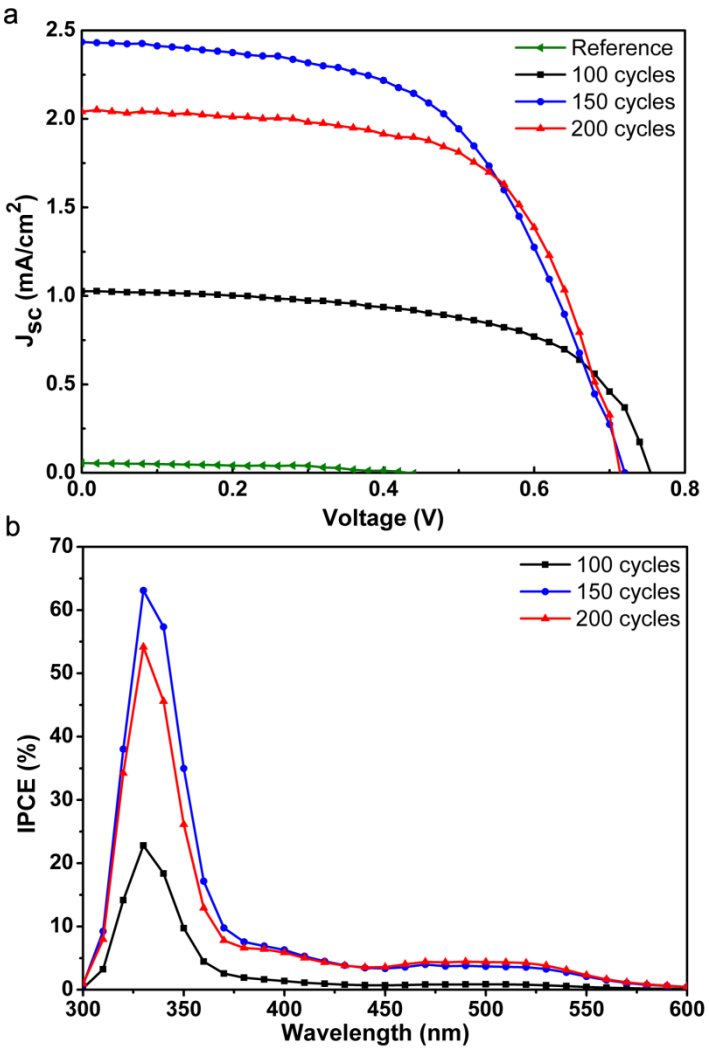

Figure 6.6: DSSC devices with 100,150 and 200 cycles templated TiO_2 a) *J-V* curves b) IPCE curves

By noting that J_{sc} is mainly determined by light absorption strength over the solar spectrum, the substantial increase in J_{sc} and P_{max} can be supported by the monochromatic incident photon conversion efficiency (IPCE) measurement results shown in Figure 6.6b. These results indicate that for samples; there are 2 max peak including ~330 nm in UV region and ~510 nm in visible range. The IPCE amounts follow the same trend as efficiencies, as expected.

Table 6.1: *J–V* parameters for the experimental devices of 3D TiO_2 Networks AM 1.5 G filtered spectral illumination at 100 $mWcm^{-2}$.

TiO_2 ALD cycles	Voc (V)	Jsc μA/cm^2)	FF	η (%)
Ref.	0.41	15.53	0.45	0.01
100	0.77	287.4	0.59	0.47
150	0.73	681	0.55	0.97
200	0.71	572	0.63	0.92

Note: Values given are mean values of three cells prepared in a similar way. 8nm thick TiO_2 layer coated by ALD on FTO substrate is used as a reference cell which is named template-free device.

Chapter 7 Conclusions

The main goal of this thesis is to improve DSSC device performance through engineering the morphology and interface of the photoanode. For this aim, in the first study, we designed, synthesized and well-characterized the idea of using different cycles of ZnO shell and compared their photovoltaic (PV) performance. Of particular interest was the optimum thickness of two cycles ZnO shell wrapping around TiO_2 NWs where device shows a jump in the efficiency by about 3-fold, compared to a control reference device. The obtained results demonstrated the passivation of surface state traps upon deposition of ZnO shell. While this passivation of surface traps provides a reduction in the surface states mediated electrons' back-reactions, it was found that ZnO-induced surface band bending adds a substantial reduction in recombination rate of the device via reducing the conduction band electrons' recombination rate. Moreover, an enhancement in the amount of dye uptake for ZnO-coated TiO_2 samples is ascertained and explained utilizing the isoelectric point (IEP) concept. In spite of excellent PV power conversion efficiencies displayed for first cycles of ZnO, thicker layers impede injection rate of electrons and reduce the efficiency of the device through capturing the photogenerated dye electrons by ZnO quantum well.

In another work, we scrutinized the impact of antireflective coating in DSSC performance. We demonstrated the fabrication of large-area multilayer ORMOSIL coated DSSCs with omnidirectional, broad-band antireflection and self-cleaning properties. We showed that the measured improvements in J_{SC} as a function of incident light angle (0°, 15°, and 30°) and achieving an averaged J_{SC} improvement of 84.6% for a high oblique angle as much as 30°, stemming from enhanced transmittance and higher light absorption of the photoanode. The presented results affirm that such a nanostructured coating can be a promising idea for future performance-enhanced solar cells not only due to improving the PV performance of the cell but also for its self-cleaning property, which renders it an excellent option for outdoor applications.

Finally, we made a fabrication route to prepare TiO_2 nanonetworks photoanode used in DSSCs application. These high surface area nanostructures were grown on self-assembled PA nanofiber networks and exploited as an organic template for growth of interconnected TiO_2 nanofibrous. Atomic Layer Deposition (ALD) technique was utilized in growth of nanostructured titania layers as anodic material. Fabricated templated TiO_2 nanonetworks possess intriguing features, such as greater surface area and improved V_{oc} and J_{sc}, which result in enhanced photoactivity. The efficiencies of DSSCs prepared by template-directed (TiO_2 nanonetwork) and template-free (thin film) approaches were compared, and the former approach resulted in 100 fold improvement thanks to the dimensions and shape of the templated TiO_2. DSSC experiments have demonstrated superiority of nanostructured materials in terms cell parameters and emphasized the importance of bottom-up approach realized via self-assembled soft templates.

We believe that such proposals and developments of these systems exploiting interface engineering, antireflective coating and TiO_2 templates to enhance device properties have great promise in all innovative devices and our results prove this performance improvement.

7.1 Key Challenges and Recommendations

The following major factors are responsible for the low efficiency and stability of DSSCs:

- Poor absorption of the photosensitizer in the Vis and NIR ranges,
- Poor electrode contacts and resultant high series resistances,
- High viscosity of the electrolyte avoiding its diffusion inside nanopores,
- Degradation of organic electrolyte and dye under UV light irradiation,
- Recombinations in the system

The following steps can be recommended in order to enhance the efficiency and stability of DSSCs.

- Modifications on the semiconductor morphology to reduce rate of recombination,
- Improvement in the dye absorption capability using NIR sensitive dyes,
- Development of low volatile and less viscous electrolytes to substantiate ione diffusion inside the photoanode,
- Addition of organic additives to enhance optical and electrical properties of dye and electrolyte.

This dissertation resulted in 6 publications and the first paper is also inside cover of JMCA (48 issues, 2014) and two of them are also in submission process. Also, I have many posters presented in an international conferences about the research work undertaken in this thesis.

7.2 Contributions

[1] Amir Ghobadi, **T. Gamze Ulusoy**, Ruslan Garifullin, Mustafa. O. Guler, Ali. K. Okyay "Less is More: A Heterojunction Design of Single Layer Hole Tunneling ZnO Passivation Wrapping around TiO_2 Nanowires for Superior Photocatalytic Performance" submitted to SMALL.

[2] **T. Gamze Ulusoy**, B. Daglar, A. Yildirim,A. Ghobadi, M. Bayindir, and Ali K. Okyay, "Enhanced performance of dye-sensitized solar cells by omnidirectional antireflective coatings", Journal of Photonics for Energy, vol. 5, pp. 053090 1-9 2015. DOI: 10.1117/1.JPE.5.053090.

[3] **T. G. Ulusoy**, A. Ghobadi and A. K. Okyay**,** "Surface Engineered Angstrom Thick ZnO-sheathed TiO_2 Nanowires as Photoanode for Performance Enhanced Dye-sensitized Solar Cells", Journal of Materials Chemistry A, vol.2, pp. 16795–17188, 2014 DOI: 10.1039/C4TA03445G (front inside cover).

[4] Amir Ghobadi, Halil I. Yavuz, **T. Gamze Ulusoy**, K. Cagatay Icli, Macit Ozenbas, Ali K. Okyay, **"Enhanced Performance of Nanowire-Based All-TiO_2 Solar Cells using Subnanometer-Thick Atomic Layer Deposited**

ZnO Embedded Layer", Electrochim acta Vol. 157, pp. 23–30, 2015. DOI: 10.1016/j.electacta.2015.01.079.

[5] T. Gamze Ulusoy, Amir Ghobadi, Ali K. Okyay,"Sub-nanometer Interface Engineering of Photoanodes Using Atomic Layer Deposited ZnO for Dye-Sensitized Solar Cells", Nanoday 2014, May 26.

[6] Ruslan Garifullin, Hamit Eren, **T. Gamze Ulusoy**, Ali K. Okyay, Mustafa O. Guler, Necmi Biyikli, "Fabrication of Self-Assembled Peptide Nanofiber Templated TiO_2 Nanonetworks by ALD and Their Application in DSSCs", XII International Conference on Nanostructured Materials (Nano 2014), July 13-18, 2014 Moscow, Russia.

[8] Ruslan Garifullin, **T. Gamze Ulusoy**, Hamit Eren, Ali K. Okyay, Mustafa O. Guler, Necmi Biyikli, "Fabrication of Self-Assembled Peptide Nanofiber Templated TiO_2 Nanonetworks by ALD and Their Application in DSSCs", 14th International Conference on Atomic Layer Deposition (ALD 2014), June 15-18, 2014 Kyoto, Japan.

[9] Ruslan Garifullin, **T. Gamze Ulusoy**, Hamit Eren, , Ali K. Okyay, Mustafa O. Guler, Necmi Biyikli, "Peptide Nanofiber Network Templated ALD-grown TiO_2 Nanostructures for Dye-Sensitized Solar Cell (DSSC) Anode", Materials Research Society (MRS), December, Boston, 2014.

[10] T. Gamze ULUSOY, Amir Ghobadi, Ali Kemal Okyay, "Sub-nanometer Interface Engineering of Photoanodes Using Atomic Layer Deposited ZnO for Dye-Sensitized Solar Cells", Materials Research Society (MRS), December, Boston, 2014.

[11] Amir Ghobadi, **T. Gamze Ulusoy,** Ali Kemal Okyay, Performance Enhancement of All-TiO_2 Based Solar Cells Using Sub Nanometer-Thick Atomic Layer Deposited ZnO Interfacial Layer, Materials Research Society (MRS), December, Boston, 2014

Chapter 8 BIBLIOGRAPHY

[1] Human Development Report, 2014.

[2] EIA, AEO 2014, Early release, Table A1 and A17 or Energy Information Administration, Department of energy, 2014.

[3] http://www.fsec.ucf.edu/consumer/solar_electricity/basics/history_of_pv. htm (accessed on 11.04.2015)

[4] O'Regan Brian and M. Gratzel, "A low-cost, high-efficiency solar cell based on dye-sensitized colloidal TiO2 films," *Nature*, vol. 353, pp. 737–739, 1991.

[5] Y. Koyama, T. Miki, X. F. Wang, and H. Nagae, "Dye-sensitized solar cells based on the principles and materials of photosynthesis: Mechanisms of suppression and enhancement of photocurrent and conversion efficiency," *Int. J. Mol. Sci.*, vol. 10, no. 11, pp. 4575–4622, 2009.

[6] J. J. Lagref, M. K. Nazeeruddin, and M. Grätzel, "Artificial photosynthesis based on dye-sensitized nanocrystalline TiO2 solar cells," *Inorganica Chim. Acta*, vol. 361, no. 3, pp. 735–745, 2008.

[7] M. Smestad, Greg P, Gratzel, "Demonstrating Electron Transfer and Nanotechnology : A Natural Dye – Sensitized Nanocrystalline Energy Converter," *J. Chem. Educ.*, vol. 75, no. 6, pp. 752–756, 1998.

[8] J. P. Harney, S. Toan, and J. Rochford, "Artificial Photosynthesis : A Workshop in Solar Cell Design," *Green Chem.*, pp. 1–6, 2011.

[9] M. A. Green, "Crystalline and thin-film silicon solar cells: State of the art and future potential," *Sol. Energy*, vol. 74, no. 3, pp. 181–192, 2003.

[10] B. Von Roedern, H. S. Ullal, and K. Zweibel, "Polycrystalline thin-film photovoltaics: From the laboratory to solar fields," *Conf. Rec. 2006 IEEE 4th World Conf. Photovolt. Energy Conversion, WCPEC-4*, no. May, pp. 384–387, 2007.

[11] M. Grätzel, "Dye-sensitized solar cells," *J. Photochem. Photobiol. C Photochem. Rev.*, vol. 4, no. 2, pp. 145–153, Oct. 2003.

[12] P. V Kamat, “Quantum Dot Solar Cells. Semiconductor Nanocrystals as Light Harvesters,” *J. Phys. Chem. C*, vol. 112, no. 48, pp. 18737–18753, 2008.

[13] M. a. Green, A. Ho-Baillie, and H. J. Snaith, “The emergence of perovskite solar cells,” *Nat. Photonics*, vol. 8, no. 7, pp. 506–514, 2014.

[14] H. Liu, V. Avrutin, N. Izyumskaya, Ü. Özgr, and H. Morkoç, “Transparent conducting oxides for electrode applications in light emitting and absorbing devices,” *Superlattices Microstruct.*, vol. 48, no. 5, pp. 458–484, 2010.

[15] J. D. Roy-mayhew and I. Aksay, “Graphene Materials and Their Use in Dye-Sensitized Solar Cells,” *Chem. Rev.*, vol. 114, pp. 6323–6348, 2014.

[16] B. Tan and Y. Wu, “Dye-sensitized solar cells based on anatase TiO2 nanoparticle/nanowire composites.,” *J. Phys. Chem. B*, vol. 110, no. 32, pp. 15932–15938, 2006.

[17] M. Law, L. E. Greene, J. C. Johnson, R. Saykally, and P. Yang, “Nanowire dye-sensitized solar cells.,” *Nat. Mater.*, vol. 4, no. 6, pp. 455–9, Jun. 2005.

[18] J. B. Baxter and E. S. Aydil, “Nanowire-based dye-sensitized solar cells,” *Appl. Phys. Lett.*, vol. 86, no. 5, pp. 1–3, 2005.

[19] G. Mor, K. Shankar, M. Paulose, O. K. Varghese, and C. A. Grimes, “Use of Highly-Ordered TiO2 Nanotube Arrays in Dye-Sensitized Solar Cells,” *Nano Lett.*, vol. 6, no. 2, pp. 215–218, 2006.

[20] C. P. Grigoropoulos and H. J. Sung, “Nanoforest of Hydrothermally Grown Hierarchical ZnO Nanowires for a high efficiency Dye-Sensitized Solar Cell,” *Nano Lett.*, vol. 11, pp. 666–671, 2011.

[21] M. Mccune, W. Zhang, and Y. Deng, “High Efficiency Dye-Sensitized Solar Cells Based on Three- Dimensional Multilayered ZnO Nanowire Arrays with ‘ Caterpillar- like ’ Structure,” *Nano Lett.*, vol. 12, pp. 3656–3662, 2012.

[22] Y. Liu, H. Wang, H. Shen, and W. Chen, “The 3-dimensional dye-sensitized solar cell and module based on all titanium substrates,” *Appl. Energy*, vol. 87, no. 2, pp. 436–441, 2010.

[23] M. Ye, X. Wen, M. Wang, J. Iocozzia, N. Zhang, C. Lin, and Z. Lin, “Recent advances in dye-sensitized solar cells: from photoanodes, sensitizers and electrolytes to counter electrodes,” *Mater. Today*, vol. 18, no. 3, pp. 155–162, 2015.

[24] J. Gong, J. Liang, and K. Sumathy, “Review on dye-sensitized solar cells (DSSCs): Fundamental concepts and novel materials,” *Renew. Sustain. Energy Rev.*, vol. 16, no. 8, pp. 5848–5860, 2012.

[25] E. Ramasamy and J. Lee, “Ordered Mesoporous SnO2 −Based Photoanodes for High-Performance Dye-Sensitized Solar Cells,” *J. Phys. Chem. C*, vol. 114, no. 50, pp. 22032–22037, 2010.

[26] N. Shahzad, F. Risplendi, D. Pugliese, S. Bianco, a. Sacco, a. Lamberti, R. Gazia, E. Tresso, and G. Cicero, “Comparison of hemi-squaraine sensitized TiO2 and ZnO photoanodes for DSSC applications,” *J. Phys. Chem. C*, vol. 117, no. 44, pp. 22778–22783, 2013.

[27] and G. B. Maria Quintana, Tomas Edvinsson, Anders Hagfeldt, “Comparison of Dye-Sensitized ZnO and TiO 2 Solar Cells : Studies of Charge Transport and Carrier Lifetime,” *J. Phys. Chem. C*, vol. 111, pp. 1035–1041, 2007.

[28] A. Le Viet, R. Jose, M. V Reddy, B. V. R. Chowdari, and S. Ramakrishna, “Nb2O5 Photoelectrodes for Dye-Sensitized Solar Cells : Choice of the Polymorph,” *J.Phys.Chem.CCH*, vol. 114, no. 49, pp. 21795–21800, 2010.

[29] R. Ghosh, M. K. Brennaman, T. Uher, M.-R. Ok, E. T. Samulski, L. E. McNeil, T. J. Meyer, and R. Lopez, “Nanoforest Nb2O5 photoanodes for dye-sensitized solar cells by pulsed laser deposition.,” *ACS Appl. Mater. Interfaces*, vol. 3, no. 10, pp. 3929–35, 2011.

[30] A. Kitiyanan, S. Pavasupree, T. Kato, Y. Suzuki, and S. Yoshikawa, “TiO2-ZrO2 Mixed Metal Oxide Electrode for a Dye-sensitized Solar Cell,” *Asian J. Energy Environ.*, vol. 6, no. 03, pp. 165–174, 2005.

[31] J. Wang, E. Jin, J.-Y. Park, W. Wang, X. Zhao, and H.-B. Gu, “Increases in solar conversion efficiencies of the ZrO2 nanofiber-doped TiO2 photoelectrode for dye-sensitized solar cells,” *Nanoscale Res. Lett.*, vol. 7, no. 1, p. 98, 2012.

[32] A. S. Polo, M. K. Itokazu, and N. Y. Murakami Iha, “Metal complex sensitizers in dye-sensitized solar cells,” *Coord. Chem. Rev.*, vol. 248, no. 13–14, pp. 1343–1361, 2004.

[33] A. Mishra, M. K. R. Fischer, and P. Büuerle, “Metal-Free organic dyes for dye-Sensitized solar cells: From structure: Property relationships to design rules,” *Angew. Chemie - Int. Ed.*, vol. 48, no. 14, pp. 2474–2499, 2009.

[34] M. R. Narayan, “Review: Dye sensitized solar cells based on natural photosensitizers,” *Renew. Sustain. Energy Rev.*, vol. 16, no. 1, pp. 208–215, 2012.

[35] M. S. Su'ait, M. Y. A. Rahman, and A. Ahmad, "Review on polymer electrolyte in dye-sensitized solar cells (DSSCs)," *Sol. Energy*, vol. 115, pp. 452–470, 2015.

[36] and L. K. Z. Yu, N. Vlachopoulos, M. Gorlovb, "Liquid electrolytes for dye-sensitized solar cells," *Dalt. Trans.*, vol. 40, pp. 10289–10303, 2011.

[37] B. Li, L. Wang, B. Kang, P. Wang, and Y. Qiu, "Review of recent progress in solid-state dye-sensitized solar cells," *Sol. Energy Mater. Sol. Cells*, vol. 90, no. 5, pp. 549–573, 2006.

[38] J. Wu, Z. Lan, J. Lin, M. Huang, Y. Huang, L. Fan, and G. Luo, "Electrolytes in Dye-Sensitized Solar Cells," *Chem. Rev.*, vol. 115, pp. 2136–2173, 2015.

[39] H. Wang and Y. H. Hu, "Graphene as a counter electrode material for dye-sensitized solar cells," *Energy Environ. Sci.*, vol. 5, no. 8, p. 8182, 2012.

[40] J. D. Roy-mayhew, D. J. Bozym, C. Punckt, and I. a Aksay, "Functionalized Graphene as a Catalytic counter electrode in dye sensitized Solar Cells," *ACS Nano*, vol. 4, no. 10, pp. 6203–6211, 2010.

[41] A. F. Nogueira, C. Longo, and M. A. De Paoli, "Polymers in dye sensitized solar cells: Overview and perspectives," *Coord. Chem. Rev.*, vol. 248, no. 13–14, pp. 1455–1468, 2004.

[42] M. M. Byranvand, a N. Kharat, A. Badiei, and M. H. Bazargan, "Electron Transfer in Dye-Sensitized Solar Cells," *J. Optoelectron. Biomed. Mater.*, vol. 4, no. 3, pp. 49–57, 2012.

[43] A. Listorti, B. O. Regan, and J. R. Durrant, "Electron Transfer Dynamics in Dye-Sensitized Solar Cells," *Chem. Mater.*, vol. 23, pp. 3381–3399, 2011.

[44] Y. Diamant, S. Chappel, S. G. Chen, O. Melamed, and A. Zaban, "Core–shell nanoporous electrode for dye sensitized solar cells: the effect of shell characteristics on the electronic properties of the electrode," *Coord. Chem. Rev.*, vol. 248, no. 13–14, pp. 1271–1276, Jul. 2004.

[45] A. Zaban, M. Greenshtein, and J. Bisquert, "Determination of the electron lifetime in nanocrystalline dye solar cells by open-circuit voltage decay measurements," *ChemPhysChem*, vol. 4, no. 8, pp. 859–864, 2003.

[46] S. E. Koops, B. C. O'Regan, P. R. F. Barnes, and J. R. Durrant, "Parameters influencing the efficiency of electron injection in dye-sensitized solar cells.," *J. Am. Chem. Soc.*, vol. 131, no. 13, pp. 4808–18, Apr. 2009.

[47] N. Robertson, “Optimizing dyes for dye-sensitized solar cells.,” *Angew. Chem. Int. Ed. Engl.*, vol. 45, no. 15, pp. 2338–45, Apr. 2006.

[48] C. Klein, M. K. Nazeeruddin, P. Liska, D. Di Censo, N. Hirata, E. Palomares, J. R. Durrant, and M. Grätzel, “Engineering of a novel ruthenium sensitizer and its application in dye-sensitized solar cells for conversion of sunlight into electricity.,” *Inorg. Chem.*, vol. 44, no. 2, pp. 178–80, Jan. 2005.

[49] D. Kuang, S. Ito, B. Wenger, C. Klein, J.-E. Moser, R. Humphry-Baker, S. M. Zakeeruddin, and M. Grätzel, “High molar extinction coefficient heteroleptic ruthenium complexes for thin film dye-sensitized solar cells.,” *J. Am. Chem. Soc.*, vol. 128, no. 12, pp. 4146–54, Mar. 2006.

[50] M. K. Nazeeruddin, P. Péchy, T. Renouard, S. M. Zakeeruddin, R. Humphry-Baker, P. Comte, P. Liska, L. Cevey, E. Costa, V. Shklover, L. Spiccia, G. B. Deacon, C. a Bignozzi, and M. Grätzel, “Engineering of efficient panchromatic sensitizers for nanocrystalline TiO(2)-based solar cells.,” *J. Am. Chem. Soc.*, vol. 123, no. 8, pp. 1613–24, Mar. 2001.

[51] S. Y. Huang, G. Schlichtho, A. J. Nozik, M. Gra, and A. J. Frank, “Charge Recombination in Dye-Sensitized Nanocrystalline TiO 2 Solar Cells,” vol. 5647, no. 96, pp. 2576–2582, 1997.

[52] J. Van De Lagemaat, N. Park, and A. J. Frank, “Influence of Electrical Potential Distribution , Charge Transport , and Recombination on the Photopotential and Photocurrent Conversion Efficiency of Dye-Sensitized Nanocrystalline TiO 2 Solar Cells : A Study by Electrical Impedance and Optical Modulation,” pp. 2044–2052, 2000.

[53] S. H. Ko, “Review of the Multi-scale Nano-structure Approach to the Development of High Efficiency Solar Cells,” *smart Sci.*, vol. 2, no. 2, pp. 54–62, 2014.

[54] M. J. Katz, M. J. D. Vermeer, O. K. Farha, M. J. Pellin, and J. T. Hupp, “E ff ects of Adsorbed Pyridine Derivatives and Ultrathin Atomic-Layer- Deposited Alumina Coatings on the Conduction Band-Edge Energy of TiO 2 and on Redox-Shuttle-Derived Dark Currents,” 2013.

[55] A. R. Pascoe, L. Bourgeois, N. W. Du, W. Xiang, and Y. Cheng, “Surface State Recombination and Passivation in Nanocrystalline TiO 2 Dye-Sensitized Solar Cells,” 2013.

[56] T. P. Brennan, J. T. Tanskanen, K. E. Roelofs, J. W. F. To, W. H. Nguyen, J. R. Bakke, I. Ding, B. E. Hardin, A. Sellinger, M. D. Mcgehee, and S. F. Bent,

"TiO 2 Conduction Band Modulation with In 2 O 3 Recombination Barrier Layers in Solid-State Dye-Sensitized Solar Cells," 2013.

[57] E. Palomares, J. N. Clifford, S. a Haque, T. Lutz, and J. R. Durrant, "Control of charge recombination dynamics in dye sensitized solar cells by the use of conformally deposited metal oxide blocking layers.," *J. Am. Chem. Soc.*, vol. 125, no. 2, pp. 475–82, Jan. 2003.

[58] A. K. Chandiran, N. Tetreault, R. Humphry-Baker, F. Kessler, E. Baranoff, C. Yi, M. K. Nazeeruddin, and M. Grätzel, "Subnanometer Ga2O3 tunnelling layer by atomic layer deposition to achieve 1.1 V open-circuit potential in dye-sensitized solar cells.," *Nano Lett.*, vol. 12, no. 8, pp. 3941–7, Aug. 2012.

[59] A. K. Chandiran, M. K. Nazeeruddin, and M. Grätzel, "The Role of Insulating Oxides in Blocking the Charge Carrier Recombination in Dye-Sensitized Solar Cells," *Adv. Funct. Mater.*, vol. 24, no. 11, pp. 1615–1623, Mar. 2014.

[60] T. C. Li, S. Go, F. Fabregat-santiago, J. Bisquert, P. R. Bueno, C. Prasittichai, J. T. Hupp, and T. J. Marks, "Surface Passivation of Nanoporous TiO 2 via Atomic Layer Deposition of ZrO 2 for Solid-State Dye-Sensitized Solar Cell Applications," vol. 14, pp. 18385–18390, 2009.

[61] E. Barea, X. Xu, V. González-Pedro, T. Ripollés-Sanchis, F. Fabregat-Santiago, and J. Bisquert, "Origin of efficiency enhancement in Nb2O5 coated titanium dioxide nanorod based dye sensitized solar cells," *Energy Environ. Sci.*, vol. 4, no. 9, p. 3414, 2011.

[62] A. K. Chandiran, M. K. Nazeeruddin, and M. Graetzel, "The Role of Insulating Oxides in Blocking the Charge Carrier Recombination in Dye-Sensitized Solar Cells.," *Adv. Funct. Mater.*, vol. 24, no. 11, pp. 1615–1623, 2014.

[63] A. Kay and M. Grätzel, "Dye-sensitized core-shell nanocrystals: Improved efficiency of mesoporous tin oxide electrodes coated with a thin layer of an insulating oxide," *Chem. Mater.*, vol. 14, no. 7, pp. 2930–2935, 2002.

[64] Z. L. Wang, "Functional oxide nanobelts: materials, properties and potential applications in nanosystems and biotechnology.," *Annu. Rev. Phys. Chem.*, vol. 55, pp. 159–96, Jan. 2004.

[65] R. H. Baughman, A. a Zakhidov, and W. a de Heer, "Carbon nanotubes--the route toward applications.," *Science*, vol. 297, no. 5582, pp. 787–92, Aug. 2002.

[66] Z. W. Pan, Z. R. Dai, and Z. L. Wang, "Nanobelts of Semiconducting Oxides," vol. 291, no. March, pp. 2000–2002, 2001.

[67] H. Ceylan, C. Ozgit-Akgun, T. S. Erkal, I. Donmez, R. Garifullin, A. B. Tekinay, H. Usta, N. Biyikli, and M. O. Guler, "Size-controlled conformal nanofabrication of biotemplated three-dimensional TiO_2 and ZnO nanonetworks.," *Sci. Rep.*, vol. 3, p. 2306, Jan. 2013.

[68] S.-C. Li and U. Diebold, "Reactivity of TiO2 rutile and anatase surfaces toward nitroaromatics.," *J. Am. Chem. Soc.*, vol. 132, no. 1, pp. 64–6, Jan. 2010.

[69] M. Andersson and O. Lars, "Preparation of Nanosize Anatase and Rutile TiO 2 by Hydrothermal Treatment of Microemulsions and Their Activity for Photocatalytic Wet Oxidation of Phenol," pp. 10674–10679, 2002.

[70] S. Kwon, S. Bang, S. Lee, S. Jeon, W. Jeong, H. Kim, S. C. Gong, H. J. Chang, H. Park, and H. Jeon, "Characteristics of the ZnO thin film transistor by atomic layer deposition at various temperatures," *Semicond. Sci. Technol.*, vol. 24, no. 3, p. 035015, Mar. 2009.

[71] D. Chu, A. Younis, and S. Li, "Direct growth of TiO 2 nanotubes on transparent substrates and their resistive switching characteristics," *J. Phys. D. Appl. Phys.*, vol. 45, no. 35, p. 355306, Sep. 2012.

[72] F. Kayaci, S. Vempati, C. Ozgit-Akgun, I. Donmez, N. Biyikli, and T. Uyar, "Selective isolation of the electron or hole in photocatalysis: ZnO-TiO2 and TiO2-ZnO core-shell structured heterojunction nanofibers via electrospinning and atomic layer deposition.," *Nanoscale*, Mar. 2014.

[73] X. Zhang, J. Qin, Y. Xue, P. Yu, B. Zhang, L. Wang, and R. Liu, "Effect of aspect ratio and surface defects on the photocatalytic activity of ZnO nanorods.," *Sci. Rep.*, vol. 4, p. 4596, Jan. 2014.

[74] X.-G. Han, H.-Z. He, Q. Kuang, X. Zhou, X.-H. Zhang, T. Xu, Z.-X. Xie, and L.-S. Zheng, "Controlling Morphologies and Tuning the Related Properties of Nano/Microstructured ZnO Crystallites," *J. Phys. Chem. C*, vol. 113, no. 2, pp. 584–589, Jan. 2009.

[75] R. Wang, N. Sakai, A. Fujishima, and T. Watanabe, "Studies of Surface Wettability Conversion on TiO 2 Single-Crystal Surfaces," pp. 2188–2194, 1999.

[76] P. Scheiber, A. Riss, M. Schmid, P. Varga, and U. Diebold, "Observation and Destruction of an Elusive Adsorbate with STM: O_{2}/TiO_{2}(110)," *Phys. Rev. Lett.*, vol. 105, no. 21, p. 216101, Nov. 2010.

[77] S. Tan, Y. Ji, Y. Zhao, A. Zhao, B. Wang, J. Yang, and J. G. Hou, "Molecular oxygen adsorption behaviors on the rutile TiO2(110)-1×1 surface: an in situ

study with low-temperature scanning tunneling microscopy.," *J. Am. Chem. Soc.*, vol. 133, no. 6, pp. 2002–9, Feb. 2011.

[78] N. G. Petrik and G. a Kimmel, "Probing the photochemistry of chemisorbed oxygen on TiO2(110) with Kr and other co-adsorbates.," *Phys. Chem. Chem. Phys.*, vol. 16, no. 6, pp. 2338–46, Feb. 2014.

[79] C. Lun Pang, R. Lindsay, and G. Thornton, "Chemical reactions on rutile TiO2(110).," *Chem. Soc. Rev.*, vol. 37, no. 10, pp. 2328–53, Oct. 2008.

[80] F. Liu, L. Lu, P. Xiao, H. He, L. Qiao, and Y. Zhang, "Effect of Oxygen Vacancies on Photocatalytic Efficiency of TiO2 Nanotubes Aggregation," *Bull. Korean Chem. Soc.*, vol. 33, no. 7, pp. 2255–2259, 2012.

[81] N. Bundaleski, a G. Silva, U. Schröder, a M. C. Moutinho, and O. M. N. D. Teodoro, "Adsorption dynamics of water on the surface of TiO2 (110)," *J. Phys. Conf. Ser.*, vol. 257, p. 012008, Nov. 2010.

[82] J. Wu, G. Yue, Y. Xiao, J. Lin, M. Huang, Z. Lan, Q. Tang, Y. Huang, L. Fan, S. Yin, and T. Sato, "An ultraviolet responsive hybrid solar cell based on titania/poly(3-hexylthiophene).," *Sci. Rep.*, vol. 3, p. 1283, Jan. 2013.

[83] L. Zhao, M. Xia, Y. Liu, B. Zheng, Q. Jiang, and J. Lian, "Structure and Photocatalysis of TiO 2 / ZnO Double-Layer Film Prepared by Pulsed Laser Deposition," vol. 53, no. 3, pp. 463–468, 2012.

[84] Z. W. Ai, Y. Wu, H. Wu, T. Wang, C. Chen, Y. Xu, and C. Liu, "Enhanced band-edge photoluminescence from ZnO-passivated ZnO nanoflowers by atomic layer deposition.," *Nanoscale Res. Lett.*, vol. 8, no. 1, p. 105, Jan. 2013.

[85] S. Mathew, A. K. Prasad, T. Benoy, P. P. Rakesh, M. Hari, T. M. Libish, P. Radhakrishnan, V. P. N. Nampoori, and C. P. G. Vallabhan, "UV-visible photoluminescence of TiO2 nanoparticles prepared by hydrothermal method.," *J. Fluoresc.*, vol. 22, no. 6, pp. 1563–9, Nov. 2012.

[86] M. K. Nowotny, L. R. Sheppard, T. Bak, and J. Nowotny, "Defect chemistry of titanium dioxide. Application of defect engineering in processing of TiO2-based photocatalysts," *J. Phys. Chem. C*, vol. 112, no. 14, pp. 5275–5300, 2008.

[87] G. Liu, F. Li, D.-W. Wang, D.-M. Tang, C. Liu, X. Ma, G. Q. Lu, and H.-M. Cheng, "Electron field emission of a nitrogen-doped TiO(2) nanotube array.," *Nanotechnology*, vol. 19, no. 2, p. 025606, Jan. 2008.

[88] T. T. Pham, K. Y. Lee, J.-H. Lee, K.-H. Kim, K.-S. Shin, M. K. Gupta, B. Kumar, and S.-W. Kim, "Reliable operation of a nanogenerator under ultraviolet light via engineering piezoelectric potential," *Energy Environ. Sci.*, vol. 6, no. 3, p. 841, 2013.

[89] C.-Y. Chen, J. R. D. Retamal, I.-W. Wu, D.-H. Lien, M.-W. Chen, Y. Ding, Y.-L. Chueh, C.-I. Wu, and J.-H. He, "Probing surface band bending of surface-engineered metal oxide nanowires.," *ACS Nano*, vol. 6, no. 11, pp. 9366–72, Nov. 2012.

[90] B. Tadesse, "SOIL-WATER ENVIRONMENT," no. May, 1997.

[91] K. Shen, K. Wu, and D. Wang, "Band alignment of ultra-thin hetero-structure ZnO/TiO2 junction," *Mater. Res. Bull.*, vol. 51, pp. 141–144, Mar. 2014.

[92] S. Xuhui, C. Xinglan, T. Wanquan, W. Dong, and L. Kefei, "Performance comparison of dye-sensitized solar cells by using different metal oxide- coated TiO2 as the photoanode," *AIP Adv.*, vol. 4, no. 3, p. 031304, Mar. 2014.

[93] C. Cheng, A. Amini, C. Zhu, Z. Xu, H. Song, and N. Wang, "Enhanced photocatalytic performance of TiO2-ZnO hybrid nanostructures.," *Sci. Rep.*, vol. 4, p. 4181, Jan. 2014.

[94] M. Law, L. E. Greene, A. Radenovic, T. Kuykendall, J. Liphardt, and P. Yang, "ZnO-Al2O3 and ZnO-TiO2 core-shell nanowire dye-sensitized solar cells.," *J. Phys. Chem. B*, vol. 110, no. 45, pp. 22652–63, Nov. 2006.

[95] R. A. Rakkesh and S. Balakumar, "Facile Synthesis of ZnO/TiO₂ Core–Shell Nanostructures and Their Photocatalytic Activities," *J. Nanosci. Nanotechnol.*, vol. 13, no. 1, pp. 370–376, Jan. 2013.

[96] C. Kim, J. Kim, H. Choi, C. Nahm, S. Kang, S. Lee, B. Lee, and B. Park, "Author ' s personal copy The effect of TiO 2 -coating layer on the performance in nanoporous ZnO-based dye-sensitized solar cells."

[97] S. P. Kowalczyk, "Semiconductor core-level," vol. 28, no. 4, 1983.

[98] R. Deng, B. Yao, Y. F. Li, Y. M. Zhao, B. H. Li, C. X. Shan, Z. Z. Zhang, D. X. Zhao, J. Y. Zhang, D. Z. Shen, and X. W. Fan, "X-ray photoelectron spectroscopy measurement of n-ZnO/p-NiO heterostructure valence-band offset," *Appl. Phys. Lett.*, vol. 94, no. 2, p. 022108, 2009.

[99] D. O. Scanlon, C. W. Dunnill, J. Buckeridge, S. a Shevlin, A. J. Logsdail, S. M. Woodley, C. R. a Catlow, M. J. Powell, R. G. Palgrave, I. P. Parkin, G. W. Watson, T. W. Keal, P. Sherwood, A. Walsh, and A. a Sokol, "Band alignment

of rutile and anatase TiO_2.," *Nat. Mater.*, vol. 12, no. 9, pp. 798–801, Sep. 2013.

[100] F.-X. Xiao, J. Miao, and B. Liu, "Self-assembly of aligned rutile@anatase TiO2 nanorod@CdS quantum dots ternary core–shell heterostructure: cascade electron transfer by interfacial design," *Mater. Horizons*, vol. 1, no. 2, p. 259, 2014.

[101] L. E. Aygun, F. B. Oruc, F. B. Atar, and a. K. Okyay, "Dynamic Control of Photoresponse in ZnO-Based Thin-Film Transistors in the Visible Spectrum," *IEEE Photonics J.*, vol. 5, no. 2, pp. 2200707–2200707, Apr. 2013.

[102] A. Belsky, K. Ivanovskikh, A. Vasil'ev, M.-F. Joubert, and C. Dujardin, "Estimation of the Electron Thermalization Length in Ionic Materials," *J. Phys. Chem. Lett.*, vol. 4, no. 20, pp. 3534–3538, Oct. 2013.

[103] S. Zhang, X. Yang, Y. Numata, and L. Han, "Highly efficient dye-sensitized solar cells: progress and future challenges," *Energy Environ. Sci.*, vol. 6, no. 5, p. 1443, 2013.

[104] B. E. Hardin, H. J. Snaith, and M. D. McGehee, "The renaissance of dye-sensitized solar cells," *Nat. Photonics*, vol. 6, no. 3, pp. 162–169, Feb. 2012.

[105] N. Robertson, "Optimizing dyes for dye-sensitized solar cells.," *Angew. Chem. Int. Ed. Engl.*, vol. 45, no. 15, pp. 2338–45, Apr. 2006.

[106] D. Kuang, S. Ito, B. Wenger, C. Klein, J. Moser, R. Humphry-baker, S. M. Zakeeruddin, and M. Gra, "High Molar Extinction Coefficient Heteroleptic Ruthenium Complexes for Thin Film Dye-Sensitized Solar Cells," *J.AM.CHEM.SOC*, vol. 128, pp. 4146–4154, 2006.

[107] U. Bach, P. Comte, J. E. Moser, F. Weisso, and M. Gra, "letters to nature," *Lett. to Nat.*, vol. 395, pp. 583–585, 1998.

[108] Q. Zhang and G. Cao, "Nanostructured photoelectrodes for dye-sensitized solar cells," *Nano Today*, vol. 6, no. 1, pp. 91–109, Feb. 2011.

[109] R. Y. Ogura, S. Nakane, M. Morooka, M. Orihashi, Y. Suzuki, and K. Noda, "High-performance dye-sensitized solar cell with a multiple dye system," *Appl. Phys. Lett.*, vol. 94, no. 7, p. 073308, 2009.

[110] X. Yan, D. J. Poxson, J. Cho, R. E. Welser, A. K. Sood, J. K. Kim, and E. F. Schubert, "Enhanced Omnidirectional Photovoltaic Performance of Solar Cells Using Multiple-Discrete-Layer Tailored- and Low-Refractive Index Anti-

Reflection Coatings," *Adv. Funct. Mater.*, vol. 23, no. 5, pp. 583–590, Feb. 2013.

[111] J. Y. Lee, S. Lee, J. Park, Y. Jun, Y. Lee, K. M. Kim, J. H. Yun, and K. Y. Cho, "Simple approach for enhancement of light harvesting efficiency of dye-sensitized solar cells by polymeric mirror.," *Opt. Express*, vol. 18, no. 104, pp. A522–A527, 2010.

[112] H. Li, B. Jiang, R. Schaller, J. Wu, and J. Jiao, "Antireflective Photoanode Made of TiO 2 Nanobelts and a ZnO Nanowire Array," *J. Phys. Chem. C*, vol. 114, no. 26, pp. 11375–11380, 2010.

[113] U. Gangopadhyay, S. Jana, S. Das, S. Garain, and S. Ray, "Antireflective Nanocomposite Based Coating on Crystalline Silicon Solar Cells for Building-Integrated Photovoltaic Systems," *Conf. Pap. Energy*, vol. 2013, pp. 1–6, 2013.

[114] M. Tao, W. Zhou, H. Yang, and L. Chen, "Surface texturing by solution deposition for omnidirectional antireflection," *Appl. Phys. Lett.*, vol. 91, no. 8, pp. 8–10, 2007.

[115] K. M. Yeung, W. C. Luk, K. C. Tam, C. Y. Kwong, M. a. Tsai, H. C. Kuo, a. M. C. Ng, and a. B. Djuriić, "2-Step self-assembly method to fabricate broadband omnidirectional antireflection coating in large scale," *Sol. Energy Mater. Sol. Cells*, vol. 95, no. 2, pp. 699–703, 2011.

[116] M. Chigane, Y. Hatanaka, and T. Shinagawa, "Enhanced antireflection properties of silica thin films via redox deposition and hot-water treatment," *Sol. Energy Mater. Sol. Cells*, vol. 94, no. 6, pp. 1055–1058, 2010.

[117] C. Ballif, J. Dicker, D. Borchert, and T. Hofmann, "Solar glass with industrial porous SiO2 antireflection coating: Measurements of photovoltaic module properties improvement and modelling of yearly energy yield gain," *Sol. Energy Mater. Sol. Cells*, vol. 82, no. 3, pp. 331–344, 2004.

[118] B. Daglar, T. Khudiyev, G. B. Demirel, F. Buyukserin, and M. Bayindir, "Soft biomimetic tapered nanostructures for large-area antireflective surfaces and SERS sensing," *J. Mater. Chem. C*, vol. 1, no. 47, p. 7842, 2013.

[119] Z. Liu, X. Zhang, T. Murakami, and A. Fujishima, "Sol-gel SiO2/TiO2 bilayer films with self-cleaning and antireflection properties," *Sol. Energy Mater. Sol. Cells*, vol. 92, no. 11, pp. 1434–1438, 2008.

[120] N.-F. Wang, T.-W. Kuo, Y.-Z. Tsai, S.-X. Lin, P.-K. Hung, C.-L. Lin, and M.-P. Houng, "Porous SiO_2/MgF_2 broadband antireflection coatings for

superstrate-type silicon-based tandem cells," *Opt. Express*, vol. 20, no. 7, p. 7445, 2012.

[121] M. H. Asghar, M. B. Khan, S. Naseem, and Z. A. Khan, "Design and Preparation of Antireflection Films on Glass Substrate," *Turk. J. Phys.*, vol. 29, pp. 43–53, 2005.

[122] Y. Ohtera, D. Kurniatan, and H. Yamada, "Antireflection coatings for multilayer-type photonic crystals.," *Opt. Express*, vol. 18, no. 12, pp. 12249–12261, 2010.

[123] K. L. Cho, I. I. Liaw, a. H. F. Wu, and R. N. Lamb, "Influence of roughness on a transparent superhydrophobic coating," *J. Phys. Chem. C*, vol. 114, no. 25, pp. 11228–11233, 2010.

[124] A. Yildirim, T. Khudiyev, B. Daglar, H. Budunoglu, A. K. Okyay, and M. Bayindir, "Superhydrophobic and omnidirectional antireflective surfaces from nanostructured ormosil colloids," *ACS Appl. Mater. Interfaces*, 2013.

[125] H. Budunoglu, A. Yildirim, M. O. Guler, and M. Bayindir, "Highly transparent, flexible, and thermally stable superhydrophobic ORMOSIL aerogel thin films.," *ACS Appl. Mater. Interfaces*, vol. 3, no. 2, pp. 539–45, Feb. 2011.

[126] H. S. Lim, J. H. Baek, K. Park, H. S. Shin, J. Kim, and J. H. Cho, "Multifunctional hybrid fabrics with thermally stable superhydrophobicity," *Adv. Mater.*, vol. 22, no. 19, pp. 2138–2141, 2010.

[127] G. Schlichthorl, N. G. Park, and A. J. Frank, "Evaluation of the charge-collection efficiency of dye-sensitized nanocrystalline TiO2 solar cells," *J. Phys. Chem. B*, vol. 103, no. 5, pp. 782–791, 1999.